Multimodality and Nonrigid Image Registration with Application to Diffusion Tensor Imaging

Mohammed Khader

A Thesis

in

The Department

of

Computer Science and Software Engineering

Presented in Partial Fulfillment of the Requirements

for the Degree of Doctor of Philosophy at

Concordia University

Montréal, Québec, Canada

September 2012

CONCORDIA UNIVERSITY

SCHOOL OF GRADUATE STUDIES

This is to certify that the thesis prepared

By: **Mohammed Khader**

Entitled: **Multimodality and Nonrigid Image Registration with Application to Diffusion Tensor Imaging**

and submitted in partial fulfillment of the requirements for the degree of

DOCTOR OF PHILOSOPHY (Computer Science)

complies with the regulations of the University and meets the accepted standards with respect to originality and quality.

Signed by the final examining committee:

_____ Chair
Dr. A. Dolatabadi

_____ External Examiner
Dr. D. Ziou

_____ External to Program
Dr. P. Valizadeh

_____ Examiner
Dr. P. Grogono

_____ Examiner
Dr. N. Shiri

_____ Thesis Supervisor
Dr. A. Ben Hamza

Approved by _____
Dr. V. Haarslev, Graduate Program Director

November 16, 2012

_____
Dr. Robin A.L. Drew, Dean
Faculty of Engineering and Computer Science

ABSTRACT

Multimodality and Nonrigid Image Registration with Application to Diffusion Tensor Imaging

Mohammed Khader

The great challenge in image registration is to devise computationally efficient algorithms for aligning images so that their details overlap accurately. The first problem addressed in this thesis is multimodality medical image registration, which we formulate as an optimization problem in the information-theoretic setting. We introduce a viable and practical image registration method by maximizing a generalized entropic dissimilarity measure using a modified simultaneous perturbation stochastic approximation algorithm. The feasibility of the proposed image registration approach is demonstrated through extensive experiments.

The rest of the thesis is devoted to nonrigid medical image registration. We propose an information-theoretic framework by optimizing a non-extensive entropic similarity measure using the quasi-Newton method as an optimization scheme and cubic B-splines for modeling the nonrigid deformation field between the fixed and moving 3D image pairs. To achieve a compromise between the nonrigid registration accuracy and the associated computational cost, we implement a three-level hierarchical multi-resolution approach in such a way that the image resolution is increased in a coarse to fine fashion. The feasibility and registration accuracy of the proposed method are demonstrated through experimental results on a 3D magnetic resonance data volume and also on clinically acquired 4D computed tomography image data sets. In the same vein, we extend our nonrigid registration approach to align diffusion tensor images for multiple components by enabling explicit optimization of tensor reorientation. Incorporating tensor reorientation in the registration algorithm is pivotal in wrapping diffusion tensor images. Experimental results on diffusion-tensor image registration indicate the feasibility of the proposed approach and a much better performance compared to the affine registration method based on mutual information, not only in terms of registration accuracy in the presence of geometric distortions but also in terms of robustness in the presence of Rician noise.

Table of Contents

Title Page i

Table of Contents iv

List of Tables vii

List of Figures viii

Chapter

Introduction 1

1.1 Motivation and Framework . . . 1

1.2 Problem Statement . . . 2

1.2.1 Image Registration . . . 2

1.2.2 Nonrigid Image registration . . . 3

1.3 Objectives . . . 4

1.4 Background . . . 4

1.5 Mutual Information . . . 4

1.6 Literature Pertinent to Entropic Measures . . . 6

1.7 Thesis Overview and Contributions . . . 8

Chapter

An Information-Theoretic Method for Multimodality Medical Image Registration 9

2.1 Introduction . . . 9

2.2 Problem Formulation . . . 11
2.3 Proposed Multimodal Image Registration Approach . . . 12
2.3.1 Jensen-Tsallis divergence . . . 13
2.3.2 Modified SPSA optimization algorithm . . . 15
2.3.3 Modality Transformation . . . 15
2.3.4 Proposed Algorithm . . . 16
2.4 Experimental Results . . . 16
2.4.1 Modality Transformation . . . 17
2.4.2 Registration Functions . . . 17
2.4.3 Robustness and Accuracy . . . 19

Chapter

Nonrigid Image Registration using a Generalized Entropic Similarity **25**
3.1 Introduction . . . 25
3.2 Proposed Method . . . 27
3.2.1 Jensen-Tsallis (JT) Similarity . . . 28
3.2.2 Problem Statement . . . 29
3.2.3 Transformation Model . . . 30
3.2.4 Optimization of the JT Similarity . . . 30
3.2.5 Derivative of the JT Similarity . . . 33
3.2.6 Summary of the Proposed Algorithm . . . 34
3.3 Experimental Results . . . 34
3.3.1 Registration Functions . . . 35
3.3.2 Monomodality Test . . . 37
3.3.3 Multimodality Test . . . 39
3.3.4 Statistical Significance Test . . . 40
3.3.5 Real-Life Data Set: 3D Thoracic CT Images . . . 40

Chapter

Nonrigid Registration of Diffusion Tensor Images **44**
4.1 Introduction . . . 44
4.2 Background . . . 46

4.2.1 Brownian Motion . . . 46
4.2.2 Diffusion . . . 47
4.2.3 Diffusion Imaging . . . 48
4.2.4 Scalar Indices . . . 51
4.3 Proposed Method . . . 52
4.3.1 Literature Pertinent to DTI Registration . . . 52
4.3.2 Jensen-Tsallis Similarity for Multiple Components . . . 54
4.3.3 Problem Statement . . . 55
4.3.4 Tensor Reorientation Formulation . . . 55
4.3.5 Summary of the Proposed Methodology . . . 56
4.4 Experimental Results . . . 58
4.4.1 Evaluation Criteria . . . 58
4.4.2 Qualitative Registration Test . . . 59
4.4.3 Quantitative Test . . . 60
4.4.4 Effect of Noise . . . 61
4.4.5 Intersubject Test . . . 63

Chapter

Conclusions and Future Work **69**
5.1 Thesis Contributions . . . 69
5.1.1 An Information-Theoretic Method for Multimodality Image Registration 69
5.1.2 Nonrigid Image Registration using an Entropic Similarity . . . 70
5.1.3 Nonrigid Registration of DTI using a Multicomponent Entropic Similarity 70
5.2 Future Research Directions . . . 70
5.2.1 Image Denoising . . . 70
5.2.2 Image Fusion . . . 70
5.2.3 Group-wise Image Registration . . . 71
5.2.4 Diffusion Tensor Imaging Atlas . . . 71

References **72**

List of Tables

3.1 Mean square error (MSE) statistics of the estimated nonrigid deformation. 37

3.2 Comparison between the registration methods using statistical significant test (p-values). 41

3.3 CT-image and reference landmark properties. The image volumes dimensions in units of voxels and also the voxel dimensions are shown for each patient case used in this experiment. The distribution of manually registered landmark pairs regarding right, left and total lung feature points are shown as well. More details about generation and characterization of landmarks can be found in [59]. 42

List of Figures

1.1 (a) Reference image I; (b) Target image J. 3

1.2 (a) Fixed image I; (b) Moving image J; (c) Deformation field Φ 3

1.3 The relationship between entropy, joint entropy, conditional entropy and mutual information. 6

1.4 (a) a brain CT scan. (b) a synthetic image obtained by corrupting the CT image by additive Gaussian noise. (c) Scatter Plot for "perfect alignment". (d) Scatter Plot for a 2 degree rotational misalignment. (e) Scatter Plot for a 10 degree rotational misalignment 7

2.1 (a) Fixed image I; (b) Moving image J. 12

2.2 Tsallis entropy $H_\alpha(\boldsymbol{p})$ of a Bernoulli distribution $\boldsymbol{p} = (p, 1-p)$ for different values of α. 14

2.3 Multimodal images from the patient 5 dataset: (a) MR-T1 image, (b) noisy MR-T1 image, (c) CT image, (d) PET image. 18

2.4 2D plots of conditional probabilities of MR-T1 given PET: (a) before modality transformation; (b) after modality transformation. 19

2.5 Registration functions of MI, NMI, and proposed approach in aligning MRI-T1 images. From top to bottom: (a), (b) and (c) rotation only; (d), (e) and (f) translation along x-axis; (g), (h) and (i) translation along y-axis. 20

2.6 2D PLOTS OF CONDITIONAL PROBABILITIES FOR MR-T1 IMAGE ALIGNMENT: (A) AFTER APPLYING EUCLIDEAN TRANSFORMATION $\Phi_{\boldsymbol{\ell}}$ TO FIXED IMAGE WITH PARAMETER VECTOR $\boldsymbol{\ell} = (5, 5, 5)$; (B)-(D) AFTER ALIGNING THE IMAGES BY MI, NMI, AND PROPOSED APPROACH, RESPECTIVELY. 21

2.7 2D PLOTS OF CONDITIONAL PROBABILITIES FOR VARIOUS ALIGNMENT METHODS OF MR-T1 TO NOISY MR-T1 IMAGES: (A) AFTER APPLYING EUCLIDEAN TRANSFORMATION $\Phi_{\boldsymbol{\ell}}$ TO FIXED IMAGE WITH PARAMETER VECTOR $\boldsymbol{\ell} = (5, 5, 5)$; (B)-(D) AFTER ALIGNING THE IMAGES BY MI, NMI, AND PROPOSED APPROACH, RESPECTIVELY. 22

2.8 2D PLOTS OF CONDITIONAL PROBABILITIES FOR VARIOUS ALIGNMENT METHODS OF MR-T1 TO CT IMAGES: (A) AFTER APPLYING EUCLIDEAN TRANSFORMATION $\Phi_{\boldsymbol{\ell}}$ TO FIXED IMAGE WITH PARAMETER VECTOR $\boldsymbol{\ell} = (5, 5, 5)$; (B)-(D) AFTER APPLYING MODALITY TRANSFORMATION AND THEN ALIGNING THE IMAGES BY MI, NMI, AND PROPOSED APPROACH, RESPECTIVELY. 23

2.9 2D PLOTS OF CONDITIONAL PROBABILITIES FOR VARIOUS ALIGNMENTS METHODS OF MR-T1 TO PET IMAGES: (A) AFTER APPLYING EUCLIDEAN TRANSFORMATION $\Phi_{\boldsymbol{\ell}}$ TO FIXED IMAGE WITH PARAMETER VECTOR $\boldsymbol{\ell} = (5, 5, 5)$; (B)-(D) AFTER APPLYING MODALITY TRANSFORMATION AND THEN ALIGNING THE IMAGES BY MI, NMI, AND PROPOSED APPROACH, RESPECTIVELY. 24

3.1 (A) FIXED IMAGE I; (B) MOVING IMAGE J; (C) DEFORMATION FIELD $\boldsymbol{\Phi}$. 29

3.2 JT SIMILARITY $S_\alpha(\boldsymbol{p}, \boldsymbol{q})$ BETWEEN TWO BERNOULLI DISTRIBUTIONS $\boldsymbol{p} = (p, 1-p)$ AND $\boldsymbol{q} = (1-p, p)$ FOR DIFFERENT VALUES OF α. 31

3.3 REGISTRATION FUNCTIONS OF OUR APPROACH, RC, AND NMI IN ALIGNING MRI-T1 IMAGES. FROM TOP TO BOTTOM: (A), (D) AND (G) ROTATION ONLY; (B), (E) AND (H) TRANSLATION ALONG x-AXIS; (C), (F) AND (I) TRANSLATION ALONG y-AXIS. 36

3.4 GEOMETRIC DISTORTION EXPERIMENT : (A) MR-T1 IMAGE; (B) DISTORTED MR-T1 IMAGE WITH GEOMETRIC DISTORTION; (C) GROUND TRUTH DEFORMATION FIELD; (D)-(F) REGISTERED IMAGES USING OUR APPROACH, RC, AND NMI, RESPECTIVELY; (G)-(I) ESTIMATED TRANSFORMATION USING OUR APPROACH, RC, AND NMI, RESPECTIVELY. 38

3.5 GEOMETRIC AND INTENSITY DISTORTION EXPERIMENT: (A) MR-T1 IMAGE; (B) DISTORTED MR-T1 IMAGE WITH GEOMETRIC AND INTENSITY DISTORTION; (C) GROUND TRUTH DEFORMATION FIELD; (D)-(F) REGISTERED IMAGES USING OUR APPROACH, RC, AND NMI, RESPECTIVELY; (G)-(I) THE ESTIMATED TRANSFORMATION USING OUR APPROACH, RC, AND NMI, RESPECTIVELY. 39

3.6 MULTIMODALITY EXPERIMENT: (A) MR-T2 IMAGE,; (B) DISTORTED MR-T1 IMAGE WITH GEOMETRIC DISTORTION; (C) GROUND TRUTH DEFORMATION FIELD; (D) AND (E) REGISTERED IMAGES USING OUR APPROACH, AND NMI, RESPECTIVELY; (F) THE ESTIMATED TRANSFORMATION USING OUR APPROACH. 40

3.7 4D CT SCAN OF A LUNG TAKEN DURING A SINGLE BREATH CYCLE: FIXED (TOP ROW) AND MOVING (BOTTOM ROW) REPRESENT COMPONENT PHASE 3D VOLUMES FROM A 4D SET FOR PATIENT CASE NUMBER ONE. (A)-(C) DISPLAY A 3D VOLUME OF THE MAXIMUM INHALE PHASE IN TRANSVERSE, CORONAL AND SAGITTAL ORIENTATION, RESPECTIVELY; (D)-(F) DISPLAY A 3D VOLUME OF THE MAXIMUM EXHALE PHASE IN TRANSVERSE, CORONAL AND SAGITTAL ORIENTATION, RESPECTIVELY. 42

3.8 3D VOLUME REGISTRATION ACCURACY. MEAN AND STANDARD DEVIATION OF 3D REGISTRATION ERRORS ARE DEPICTED FOR EACH CASE BEFORE REGISTRATION AND AFTER APPLYING THE PROPOSED METHOD, RC AND NMI APPROACHES. ALL VALUES ARE IN UNITS OF MILLIMETERS. 43

4.1 ISOTROPIC DIFFUSION (LEFT) VS. ANISOTROPIC DIFFUSION (RIGHT). THIS IMAGE IS ADAPTED FROM BEAULIEU [69]. 48

4.2 AXIAL DW IMAGES $S_k(\boldsymbol{r})$ OF THE HUMAN BRAIN FOR DIFFERENT GRADIENT DIRECTIONS $\boldsymbol{g}_k$. 50

4.3 DIFFERENT CASES OF DIFFUSION: SPHERICAL DIFFUSION (LEFT); PLANAR DIFFUSION (CENTER); LINEAR DIFFUSION (RIGHT). 51

4.4 ELLIPSOIDAL REPRESENTATION OF THE DIFFUSION TENSOR AT EACH VOXEL LOCATION OF A DTI IMAGE. 53

4.5 (A) FIXED IMAGE I; (B) MOVING IMAGE J; (C) DEFORMATION FIELD $\boldsymbol{\Phi}$. 56

4.6 (A) AND (C) REGISTERED IMAGES BEFORE AND AFTER TENSOR REORIENTATION, RESPECTIVELY; (B) AND (D) DIFFUSION TENSORS OF A CERTAIN REGION BEFORE AND AFTER APPLYING TENSOR REORIENTATION, RESPECTIVELY. 57

4.7 THE AXIAL SLICE NO. 30 OF THE DIFFUSION TENSOR IMAGE CHOSEN AS THE TEMPLATE IN THIS STUDY : (A) DW IMAGE; (B) MEAN DIFFUSION; (C) FRACTIONAL ANISOTROPY; (D) COLOR-CODED DT ELEMENTS. THE DT MAPS ARE COLOR-CODED ACCORDING TO THE DIFFUSION DIRECTION. 60

4.8 GEOMETRIC DISTORTION EXPERIMENT: (A) GROUND TRUTH DEFORMATION FIELD; (B)-(C) DISTORTED FA AND DT ELEMENTS' IMAGES, RESPECTIVELY, WITH GEOMETRIC DISTORTION; (D)-(F) DT ELEMENTS OF THE REGISTERED IMAGES USING AFFINE, JT-FA, AND JT-DT, RESPECTIVELY; (G)-(I) FA OF THE REGISTERED IMAGES USING AFFINE, JT-FA, AND JT-DT, RESPECTIVELY. 61

4.9 QUANTITATIVE REGISTRATION RESULTS OF DEFORMED IMAGE DATA SETS WITH KNOWN DEFORMATION FIELDS. JT-DT, JT-FA, AND AFFINE REGISTRATION METHODS ARE DISPLAYED ON THE HORIZONTAL AXIS, RESPECTIVELY. (A) THE OVL MEASURES THE EIGENVALUE-EIGENVECTOR OVERLAP OF TENSORS IN CORRESPONDING VOXELS BETWEEN THE REFERENCE AND REGISTERED IMAGES. (B) THE ANGLE DIFFERENCE BETWEEN THE FIRST EIGENVECTORS OF CORRESPONDING VOXELS IN THE REFERENCE AND REGISTERED IMAGES. (C) THE MEASURE C CALCULATES THE DISCREPANCY BETWEEN THE ESTIMATED DEFORMATION FIELD AND GROUND TRUTH DEFORMATION FIELD. (D) THE p-VALUES BETWEEN THE JT-DT, JT-FA, AND AFFINE REGISTRATION TECHNIQUES REPRESENTED BY I, II, III RESPECTIVELY, ARE DISPLAYED FOR QUANTITATIVE PARAMETERS. 62

4.10 EFFECT OF NOISE. TOP: DTI DATA AFTER CORRUPTING THE DW IMAGES WITH DIFFERENT LEVELS OF RICIAN NOISE. THE DT ELEMENTS' REPRESENTATION IS ACCORDING TO DIFFUSION DIRECTION. MIDDLE AND BOTTOM: SPATIAL AND ORIENTATION CORRESPONDENCE ARE GIVEN USING JT-FA, JT-DT, AND AFFINE ALGORITHMS. THE VALUES OF C, a, AND OVL REPRESENT THE MEDIAN DEFORMATION FIELD CORRESPONDENCE, THE MEDIAN FIRST EIGENVECTOR ANGLE DIFFERENCE, AND THE EIGENVALUE-EIGENVECTOR OVERLAP, RESPECTIVELY. 64

4.11 THE FA MAP OF THE AXIAL SLICE NO. 21 COMPUTED FROM THE DIFFUSION TENSOR OF EACH SUBJECT IS PRESENTED. THE IMAGE FROM THE SUBJECT CHOSEN AS A TEMPLATE IS SHOWN ON THE TOP-LEFT. THE REST OF THE IMAGES ARE FROM THE OTHER 8 SUBJECTS BEFORE REGISTRATION. 65
4.12 THE FA MAP OF THE AXIAL SLICE NO. 21 COMPUTED FROM THE DIFFUSION TENSOR OF EACH SUBJECT IS PRESENTED. THE IMAGE FROM THE SUBJECT CHOSEN AS A TEMPLATE IS SHOWN ON THE TOP-LEFT. THE REST OF THE IMAGES ARE FROM THE OTHER 8 SUBJECTS AFTER REGISTRATION TO THE TEMPLATE WITH THE AFFINE REGISTRATION ALGORITHM. . 66
4.13 THE FA MAP OF THE AXIAL SLICE NO. 21 COMPUTED FROM THE DIFFUSION TENSOR OF EACH SUBJECT IS PRESENTED. THE IMAGE FROM THE SUBJECT CHOSEN AS A TEMPLATE IS SHOWN ON THE TOP-LEFT. THE REST OF THE IMAGES ARE FROM THE OTHER 8 SUBJECTS. THE REST OF THE IMAGES ARE FROM THE OTHER 8 SUBJECTS AFTER REGISTRATION TO THE TEMPLATE WITH THE JT-FA ALGORITHM. 67
4.14 THE FA MAP OF THE AXIAL SLICE NO. 21 CALCULATED FROM THE DIFFUSION TENSOR OF EACH SUBJECT IS PRESENTED IN THIS FIGURE. THE IMAGE FROM THE SUBJECT CHOSEN AS A TEMPLATE IS SHOWN ON THE TOP-LEFT. THE REST OF THE IMAGES ARE FROM THE OTHER 8 SUBJECTS AFTER REGISTRATION TO THE TEMPLATE WITH THE JT-DT ALGORITHM. 68

List of Acronyms

CT	Computed tomography
PET	Positron emission tomography
MRI	Magnetic resonance imaging
MI	Mutual information
NMI	Normalized mutual information
SPSA	Simultaneous perturbation stochastic approximation
SSD	Sum of squared differences
CCRE	Cross-cumulative residual entropy
cMI	Conditional mutual information
RC	Residual complexity
JT	Jensen-Tsallis
FFD	Free-form deformation
DTI	Diffusion tensor imaging
WM	White matter
JT-FA	Jensen-Tsallis applied to fractional anisotropy map
JT-DT	Jensen-Tsallis applied to diffusion tensor elements

CHAPTER 1

INTRODUCTION

In this Chapter, we present the framework and motivation behind this work, followed by the problem statement, objectives, and a brief overview of essential concepts and definitions which we will refer to throughout the thesis. We also present a short summary of background material relevant to nonrigid image registration of medical images.

1.1 MOTIVATION AND FRAMEWORK

Recent advances in medical imaging have resulted in the development of many imaging techniques that capture various aspects of the patient's anatomy and metabolism [5, 6]. Image registration is among the most challenging problems in medical imaging, and it is of paramount importance in medical diagnosis and computer aided surgery [5, 6]. Image registration or alignment refers to the process of aligning two or more images of the same scene so that their details overlap accurately [5, 6, 7]. Typically, one image, called the *fixed* or *reference* image, is considered the reference to which the other images, called *moving* or *target* images, are compared.

Images from different modalities display complementary and shared information about the object in images with different intensity maps. For example, what appears as white in one image may appear as dark grey in the other image, or not appear at all [8]. Therefore, similarity measures used for multimodal image registration must be insensitive to differing intensity maps or modality transformation must be done as pre-registration step. A wide range of image registration techniques have been recently developed for many different types of applications and data, such as mean squared alignment, correlation registration, moment invariant matching, and entropic alignment [5, 6, 7]. The latter problem will be the primary focus of Chapter

2. Our focus on the entropic approach is inspired by the successful application of the mutual information measure to medical image registration [6].

Unfortunately, not all types of image misalignment can be solved by rigid image registration, nonrigid transformations are usually required to account for image deformations. For example, the positioning of the patient may be different between modalities. In CT imaging, the patient usually lies on their back with their arms above their head and in PET imaging, they may have their arms at their sides. Also, the type of couch the patient lies on may be curved or flat. Deformations also arise from the days, months, or years that exist between image acquisition times. Regular internal organ movement, breathing, full bladder, etc. can also deform image content in nonlinear ways. Nonrigid image registration will be the focus of the thesis in Chapters 3 and 4.

1.2 Problem Statement

1.2.1 Image Registration

Image registration is of paramount importance in the field of medical imaging and has sparked a flurry of research interest in many other applications of image analysis such as remote sensing, movie editing, and archeology. The objective of image registration is to bring the moving image into alignment with the fixed image by applying a spatial transformation to the moving image. Images are usually registered for the purpose of combining or comparing them, enabling the fusion of information in the images. Roughly speaking, the image alignment problem may be formulated as a two-step process: the first step is to define a distance measure that quantifies the quality of spatial alignment between the fixed image and the spatially transformed moving image, and the second step is to develop an efficient optimization algorithm for optimizing this distance measure iteratively in order to find the optimal transformation parameters.

More precisely, given two misaligned images, the fixed image I and the moving image J as depicted in Figure 1.1, the image alignment or registration problem may be formulated as an optimization problem

$$\boldsymbol{\ell}^* = \arg\max_{\boldsymbol{\ell}} D\left(I(\boldsymbol{x}), J(\Phi_{\boldsymbol{\ell}}(\boldsymbol{x}))\right), \tag{1.1}$$

where $D(\cdot,\cdot)$ is a dissimilarity measure that quantifies the discrepancy between the fixed image and the transformed moving image; and $\Phi_{\boldsymbol{\ell}} : \Omega \to \Omega$ is a spatial transformation mapping parameterized by a parameter vector $\boldsymbol{\ell}$.

The goal of image registration is to align the moving image to the fixed image by maximizing the dissimilarity measure $D(I(\boldsymbol{x}), J(\Phi_{\boldsymbol{\ell}}(\boldsymbol{x})))$ using an optimization scheme in order to find the optimal spatial

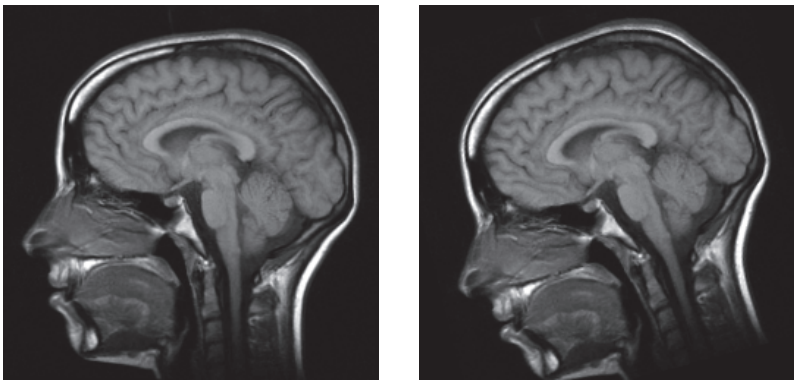

FIGURE 1.1: (a) Reference image I; (b) Target image J.

transformation parameters. Note that since the image pixel values are integers, a bilinear interpolation may be used to determine the values of $J(\Phi_{\boldsymbol{\ell}}(\boldsymbol{x}))$ when $\Phi_{\boldsymbol{\ell}}(\boldsymbol{x})$ is not an integer.

1.2.2 NONRIGID IMAGE REGISTRATION

Let I and J be two misaligned images to be registered, where I is the fixed image and J is the moving image. The moving image J is obtained by applying a deformation field $\boldsymbol{\Phi}$ to the fixed image I, as depicted in Figure 1.2. The deformation field $\boldsymbol{\Phi}$ is described by a transformation function $g(\boldsymbol{x};\boldsymbol{\mu}) : V_J \rightarrow V_I$, where V_J and V_I are continuous domains on which J and I are defined, and $\boldsymbol{\mu}$ is a set of transformation parameters to be determined. The nonrigid image registration problem may be formulated as an optimization problem

$$\hat{\boldsymbol{\mu}} = \arg\min_{\boldsymbol{\mu}} S_{\alpha}^{\boldsymbol{\omega}}\big(I(\boldsymbol{x}), J(g(\boldsymbol{x};\boldsymbol{\mu}))\big). \tag{1.2}$$

To align the transformed moving image $J(g(\boldsymbol{x};\boldsymbol{\mu}))$ to the fixed image I, we seek the set of transformation parameters $\boldsymbol{\mu}$ that minimize the similarity cost function $S_{\alpha}^{\boldsymbol{\omega}}\big(I(\boldsymbol{x}), J(g(\boldsymbol{x};\boldsymbol{\mu}))\big)$.

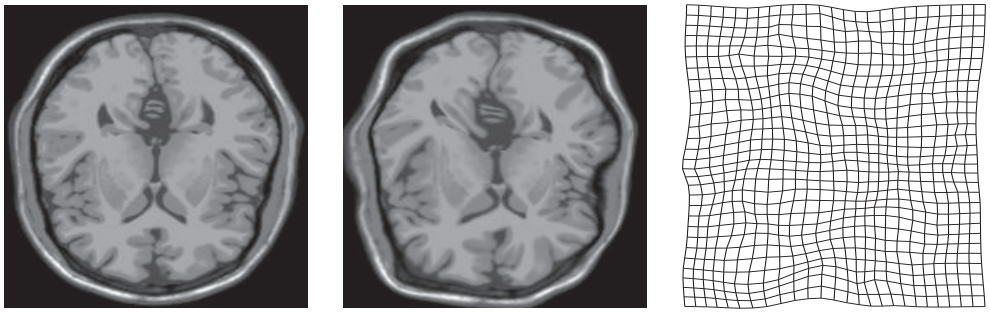

(a) (b) (c)

FIGURE 1.2: (a) Fixed image I; (b) Moving image J; (c) Deformation field $\boldsymbol{\Phi}$

The goal of nonrigid image registration is to find the set of transformation parameters $\boldsymbol{\mu}$ that best align the target image J to reference image I.

1.3 Objectives

Our main objectives may be summarized as follows:

- Develop an efficient image registration approach for aligning medical images so that their details overlap accurately, and perform an experimental comparative study with the state-of-the-art registration techniques.
- Develop a nonrigid image registration method for aligning medical images with complex deformation field accurately and efficiently.
- Develop a nonrigid registration technique for aligning diffusion tensor medical images, not only accurately and efficiently but also by keeping the diffusion tensor orientation consistent with the anatomy after image transformations.

1.4 Background

1.5 Mutual Information

Consider two images (over their region of overlap) to be observations of two discrete random variables, X and Y, with probability distributions $\boldsymbol{p}$ and $\boldsymbol{q}$ respectively. In general, random variable X will have sample space $\mathcal{X}$ and random variable Y will have sample space $\mathcal{Y}$. For imaging purposes, the modality-specific intensity maps determine $\mathcal{X}$ and $\mathcal{Y}$. The 2D joint histogram can be constructed from images X and Y over their region of overlap by counting the number of times the intensity pair (x, y) occurs in corresponding pixel pairs $(X_{i,j}, Y_{i,j})$. Normalizing the joint histogram gives an estimate of the joint probability distribution $\boldsymbol{r}$, where $r(x, y) = \Pr(X_{i,j} = x, Y_{i,j} = y)$, for $x \in \mathcal{X}$, $y \in \mathcal{Y}$ and $(X_{i,j}, Y_{i,j})$ corresponding pixels contained in the region of overlap. A result of the joint histogram normalization is that $\sum_x \sum_y r(x, y) = 1$.
The marginals of the joint distribution can be defined as follows:

$$\sum_{x \in \mathcal{X}} r(x, y) = q(y) \tag{1.3}$$

and

$$\sum_{y \in \mathcal{Y}} r(x, y) = p(x) \tag{1.4}$$

Joint entropy, $H(X,Y)$, is a functional of the joint probability distribution $\boldsymbol{r}$, and is a measure of the combined randomness of the discrete random variables X and Y [1]. The joint entropy, $H(X,Y)$, for the discrete random variables X and Y, with joint probability distribution $\boldsymbol{r}$, is defined as

$$H(X,Y) = H(\boldsymbol{r}) = -\sum_{x\in\mathcal{X}}\sum_{y\in\mathcal{Y}} r(x,y)\log r(x,y) \tag{1.5}$$

Relative entropy, or Kullback-Leibler divergence, is a measure of the distance between one probability distribution and another [1]. It measures the error of using an estimated distribution $\boldsymbol{q}$ over the true distribution $\boldsymbol{p}$. The Kullback-Leibler divergence is defined as

$$D(\boldsymbol{p}||\boldsymbol{q}) = \sum_{x\in\mathcal{X}} p(x)\log\frac{p(x)}{q(x)} \tag{1.6}$$

A special case of relative entropy is the mutual information. Mutual information measures the amount of information shared between two random variables, or the decrease in randomness of one random variable due to the knowledge of another [8]. Mutual information is defined as follows:

$$I(X;Y) = \sum_{x\in\mathcal{X}}\sum_{y\in\mathcal{Y}} r(x,y)\log\frac{r(x,y)}{p(x)q(y)} \tag{1.7}$$

The conditional entropy quantifies the remaining entropy (i.e. uncertainty) of a random variable Y given that the value of a second random variable X is known. It is referred to as the entropy of Y conditional on X, and is written $H(Y|X)$. The conditional entropy of X given Y is defined as:

$$H(X|Y) = -\sum_{x\in\mathcal{X}}\sum_{y\in\mathcal{Y}} r(x,y)\log r(x|y) \tag{1.8}$$

where $r(x|y)$ conditional probability distribution of X given Y.

Mutual information can be expressed in terms of entropy:

$$I(X;Y) = H(X) + H(Y) - H(X,Y) \tag{1.9}$$

$$I(X;Y) = H(X) - H(X|Y) \tag{1.10}$$

$$I(X;Y) = H(Y) - H(Y|X) \tag{1.11}$$

This relationship is expressed by the Venn diagram [1], as shown in Figure 1.3.

Note that, (i) mutual information is the amount of uncertainty in Y (or X) that is reduced when X (or Y) is known, (ii) maximizing the mutual information is equivalent to minimizing the joint entropy, (iii)

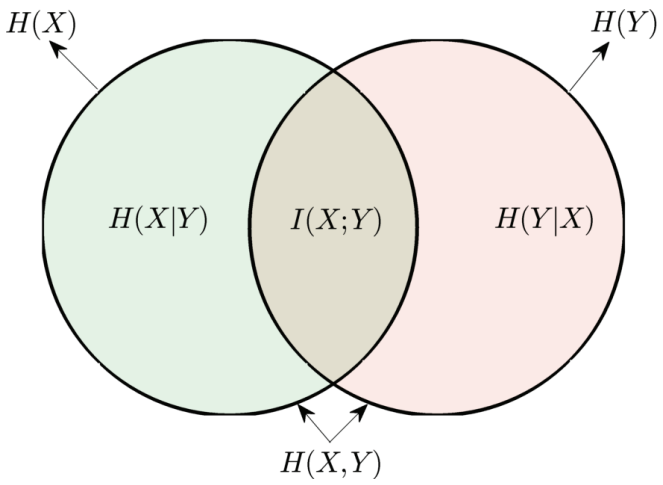

FIGURE 1.3: The relationship between entropy, joint entropy, conditional entropy and mutual information.

the advantage of using mutual information over joint entropy is that marginal entropies are included in the mutual information.

1.6 LITERATURE PERTINENT TO ENTROPIC MEASURES

The investigation of entropic measures for image registration started in the 1990s with Woods *et al.*'s seminal paper [2]. This also marks the beginning of the exploration of fast and reliable automatic multimodal registration methods. The common trait of these approaches is that they rely on the whole image, particularly pixel intensity values, when determining the quality of alignment. This is contrary to landmark-based approaches that require the definition and computation of specific landmarks [8]. These algorithms are constrained by the quality and speed of the landmark detection step.

The basic idea that motivates the employment of entropic measures for quantifying the quality of alignment is simple: corresponding features extracted from the images should become statistically more dependent with better alignment.

This observation is illustrated with an example shown in Figure 1.4, where the scatter-plots display pixel intensity value pairs (from both images). Notice that, since both images are the same (up to some noise), at perfect alignment pixel samples cluster around the $x = y$ line. At bad alignment, however, the samples are scattered, i.e., the joint histogram is more dispersed. In an attempt to quantify the dispersion of the joint histogram both Collignon *et al.* [3] and Studholme *et al.* [4] proposed to employ the entropy of the joint histogram for determining alignment quality. These studies were mainly based on the empirical observation

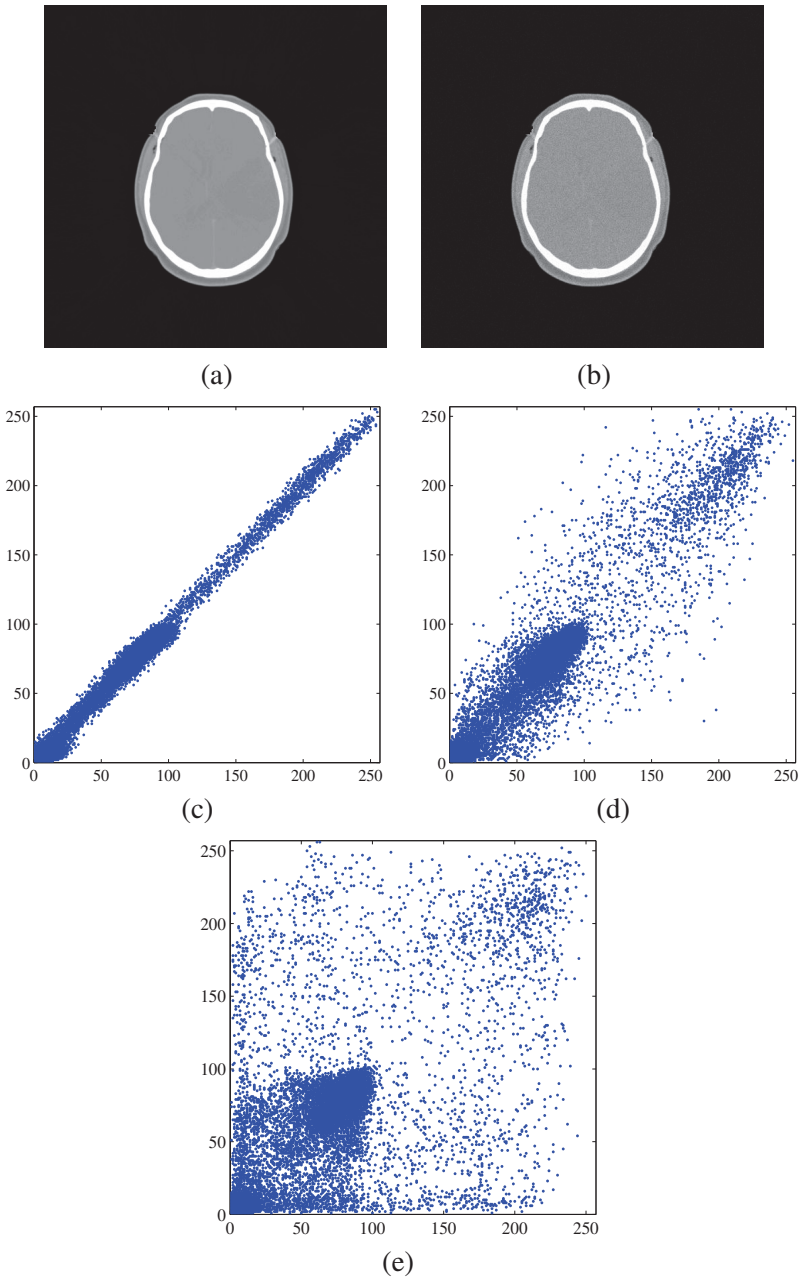

FIGURE 1.4: (a) a brain CT scan. (b) a synthetic image obtained by corrupting the CT image by additive Gaussian noise. (c) Scatter Plot for ”perfect alignment”. (d) Scatter Plot for a 2 degree rotational misalignment. (e) Scatter Plot for a 10 degree rotational misalignment

that the joint distribution tends to be sharper with well-defined peaks at good alignment, which yields a small entropy. Experiments indicated that the approach was promising, yet no rigorous theoretical derivation was provided. The papers of Collignon *et al.* [11] and Viola and Wells [10] formalized these ideas and motivated mutual information as an alignment measure.

1.7 Thesis Overview and Contributions

The organization of this thesis is as follows:

- In Chapter 2, we propose an image registration method by maximizing a Tsallis entopy-based divergence using a modified simultaneous perturbation stochastic approximation algorithm.
- In Chapter3, we propose a nonrigid image registration technique by optimizing a generalized information-theoretic similarity measure using the quasi-Newton method as an optimization scheme and cubic B-splines for modeling the nonrigid deformation field between the fixed and moving 3D image pairs.
- In Chapter 4, we develop a multicomponent nonrigid registration approach for diffusion tensor images by extending our deformable registration algorithm described in Chapter 3. Moreover, we enable explicit orientation optimization by incorporating tensor reorientation, which is necessary for wrapping DT images.
- In Chapter 5, we summarize the contributions in this thesis and propose some future research directions.

CHAPTER 2

AN INFORMATION-THEORETIC METHOD FOR MULTIMODALITY MEDICAL IMAGE REGISTRATION

In this Chapter, an information-theoretic approach for multimodal image registration is presented. In the proposed approach, image registration is carried out by maximizing a Tsallis entopy-based divergence using a modified simultaneous perturbation stochastic approximation algorithm. This divergence measure achieves its maximum value when the conditional intensity probabilities of the transformed moving image given the reference image are degenerate distributions. Experimental results are provided to demonstrate the registration accuracy of the proposed approach in comparison to existing entropic image alignment techniques. The feasibility of the proposed algorithm is demonstrated on medical images from magnetic resonance imaging (MRI), computer tomography (CT), and positron emission tomography (PET).

2.1 INTRODUCTION

Recent advances in medical imaging have resulted in the development of many multimodal imaging techniques that capture various aspects of the patient's anatomy and metabolism [6, 5]. Multimodal image registration is among the most challenging problems in medical imaging, and it is of paramount importance in medical diagnosis and computer aided surgery [5, 6]. Image registration or alignment refers to the process of aligning two or more images of the same scene so that their details overlap accurately [5, 6, 7]. Typically, one image, called the fixed image, is considered the reference to which the other images, called moving images, are compared. The objective of image registration is to bring the moving image into alignment with the fixed image by applying a spatial transformation to the moving image. Images are usually regis-

tered for the purpose of combining or comparing them, enabling the fusion of information in the images. Roughly speaking, the image alignment problem may be formulated as a two-step process: the first step is to define a distance measure that quantifies the quality of spatial alignment between the fixed image and the spatially transformed moving image, and the second step is to develop an efficient optimization algorithm for optimizing this distance measure iteratively in order to find the optimal transformation parameters. A wide range of image registration techniques have been developed for many different types of applications and data, such as mean squared alignment, correlation registration, and moment invariant matching [7]. These techniques are, however, mainly used in intramodal image registration, where images are of the same modality. Intramodal registration is most commonly used for time series analysis in order to detect subtle changes or contrast enhancements.

Multimodality imaging is widely considered to involve the incorporation of two or more imaging modalities that are acquired by different scanners. The goal of multimodal image registration is to align intermodal images created by different medical diagnostic modalities in order to improve diagnosis accuracy [6, 5]. Intermodal images display complementary and shared information about the object in images with different intensity maps. Therefore, distance measures used for multimodal image registration must be insensitive to differing intensity maps. Recently, much attention has been paid to the multimodal image registration problem using information-theoretic measures [9, 10, 11, 14, 12, 13, 15]. The latter will be the focus of this chapter. The most popular approach in multimodal image registration maximizes the mutual information (MI) between the fixed and moving images [9, 10, 11]. This approach involves maximizing the information (entropy) contained in each image while minimizing the information (joint entropy) contained in the overlayed images. Although MI has been successfully applied to multimodality image registration, it is worth noting that the MI-based registration methods might have the limited performances, once the initial misalignment of the two images is large or equally the overlay region of the two images is relatively small [13]. Moreover, MI is sensitive to the changes that occur in the distributions (overlap statistics) as a result of changes in the region of overlap. To circumvent these limitations, various methods have been proposed to improve the robustness of MI-based registration, including normalized mutual information (NMI) and Rényi entropy based approaches [17, 19, 18]. The NMI approach, proposed by Studholme *et al.* [17], is a robust similarity measure that allows for fully automated intermodal image registration algorithms. Furthermore, NMI-based registration is less sensitive to the changes in the overlap of two images. Cahill *et al.* [18] introduced a modified NMI-based approach that is invariant to changes in overlap size. Inspired by the successful application of mutual information, and looking to address its limitations in often difficult

imagery, He *et al.* proposed in [19] an information-theoretic approach to ISAR image registration by estimating the target motion during the imaging time using a Rényi entropy based divergence. This generalized entropic divergence enjoys appealing mathematical properties affording a great flexibility in a number of applications [20, 21, 22, 23]. Sabuncu *et al.* [24] proposed a minimal spanning graph for multimodal image registration using Jensen-Rényi divergence [19] by joint determination of both the alignment measure and a descent direction with respect to alignment parameters.

In recent years, there has been a concerted research effort in statistical physics to explore the properties of Tsallis entropy, leading to a statistical mechanics that satisfies many of the properties of the standard theory [50]. In [26], a Tsallis entropy-based image mutual information approach, combined with the simultaneous perturbation stochastic approximation (SPSA) algorithm [27], was proposed leading to accurate image registration results compared to the classical mutual information [10, 11]. In this Chapter, we propose a multimodal entropic image registration approach by maximizing the Jensen-Tsallis divergence using a modified simultaneous perturbation stochastic approximation algorithm [28]. To increase the accuracy of multimodal image alignment, we apply a histogram-based modality transformation [29] to the moving image prior to maximizing the Jensen-Tsallis divergence measure between the fixed and the transformed moving images.

The outline of this Chapter is as follows. In Section 2.2, we formulate the image alignment problem. In Section 2.3, we describe the proposed multimodal image alignment method and provide its most important algorithmic steps. In Section 2.4, we provide experimental results to show the effectiveness and the registration accuracy of the proposed approach.

2.2 Problem Formulation

In the continuous domain, an image is defined as a real-valued function $I : \Omega \to \mathbb{R}$, where Ω is a nonempty, bounded, open set in $\mathbb{R}^2$ (usually Ω is a rectangle in $\mathbb{R}^2$). We denote by $\boldsymbol{x} = (x, y)$ a pixel location in Ω. Given two misaligned images, the fixed image I and the moving image J as depicted in Figure 2.1, the image alignment or registration problem may be formulated as an optimization problem

$$\boldsymbol{\ell}^* = \arg\max_{\boldsymbol{\ell}} D\left(I(\boldsymbol{x}), J(\Phi_{\boldsymbol{\ell}}(\boldsymbol{x}))\right), \tag{2.1}$$

where $D(\cdot, \cdot)$ is a dissimilarity measure that quantifies the discrepancy between the fixed image and the transformed moving image; and $\Phi_{\boldsymbol{\ell}} : \Omega \to \Omega$ is a spatial transformation mapping parameterized by a parameter vector $\boldsymbol{\ell}$. An example of such a mapping is a Euclidean transformation with a parameter vector

$\boldsymbol{\ell} = (\boldsymbol{t}, \theta, \boldsymbol{s})$, where $\boldsymbol{t} = (t_x, t_y)$ is a translational parameter vector, θ is a rotational parameter, and $\boldsymbol{s} = (s_x, s_y)$ is a scaling parameter vector.

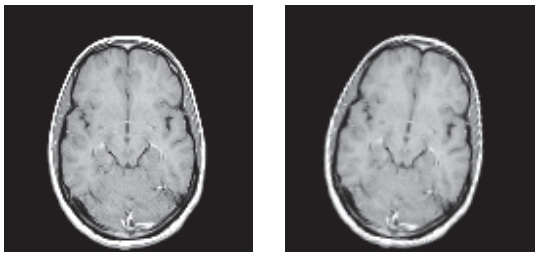

FIGURE 2.1: (a) Fixed image I; (b) Moving image J.

The goal of image registration is to align the moving image to the fixed image by maximizing the dissimilarity measure $D(I(\boldsymbol{x}), J(\Phi_{\boldsymbol{\ell}}(\boldsymbol{x})))$ using an optimization scheme in order to find the optimal spatial transformation parameters. Note that since the image pixel values are integers, a bilinear interpolation may be used to determine the values of $J(\Phi_{\boldsymbol{\ell}}(\boldsymbol{x}))$ when $\Phi_{\boldsymbol{\ell}}(\boldsymbol{x})$ is not an integer.

In the proposed approach, we apply a histogram-based modality transformation that essentially maps pixel-wise the moving image modality to the fixed image modality by finding the pixel values which most often overlap in both images [29]. This modality transform will be discussed in more details in the next section. Then, we use the Jensen-Tsallis divergence as a dissimilarity measure, and a modified simultaneous perturbation stochastic approximation (SPSA) approach as an optimization algorithm [28].

2.3 PROPOSED MULTIMODAL IMAGE REGISTRATION APPROACH

Our proposed approach may now be described as follows: Given two images that need to be registered, we first compute their conditional intensity probabilities and the Jensen-Tsallis divergence between them. Then we optimize this divergence measure using the modified SPSA algorithm.

Without loss of generality, we consider a Euclidean transformation $\Phi_{\boldsymbol{\ell}}$ with a parameter vector $\boldsymbol{\ell} = (\boldsymbol{t}, \theta)$, i.e. a transformation with translation parameter vector $\boldsymbol{t} = (t_x, t_y)$, and a rotation parameter θ. In other words, for an image pixel location $\boldsymbol{x} = (x, y)$ the Euclidean transformation is defined as $\Phi_{\boldsymbol{\ell}}(\boldsymbol{x}) = R\boldsymbol{x} + \boldsymbol{t}$, where R is a rotation matrix given by

$$R = \begin{pmatrix} \cos\theta & \sin\theta \\ -\sin\theta & \cos\theta \end{pmatrix}.$$

Denote by $\mathcal{X} = \{x_1, x_2, \ldots, x_n\}$ and $\mathcal{Y} = \{y_1, y_2, \ldots, y_n\}$ the sets of pixel intensity values of the fixed image $I(\boldsymbol{x})$ and the transformed moving image $J(\Phi_{\boldsymbol{\ell}}(\boldsymbol{x}))$ respectively. Let X and Y be two random variables taking values in $\mathcal{X}$ and $\mathcal{Y}$.

2.3.1 JENSEN-TSALLIS DIVERGENCE

Let $X = \{x_1, x_2, \ldots, x_k\}$ be a finite set with a probability distribution $\boldsymbol{p} = (p_1, p_2, \ldots, p_k)$, $k > 1$. Shannon's entropy is defined as $H(\boldsymbol{p}) = -\sum_{j=1}^{k} p_j \log(p_j)$. A generalization of Shannon entropy is Tsallis entropy [50] given by

$$H_\alpha(\boldsymbol{p}) = \frac{1}{1-\alpha}\Big(\sum_{j=1}^{k} p_j^\alpha - 1\Big) = -\sum_{j=1}^{k} p_j^\alpha \log_\alpha(p_j), \quad \alpha \in (0,1) \cup (1,\infty). \tag{2.2}$$

where $\log_\alpha$ is the α-logarithm function defined as $\log_\alpha(x) = (1-\alpha)^{-1}(x^{1-\alpha} - 1)$ for $x > 0$, and α is an exponential order also referred to as entopic index. This generalized entropy is widely used in statistical physics applications [50].

If we consider that a physical system can be decomposed in two statistical independent subsystems with probability distributions $\boldsymbol{p}$ and $\boldsymbol{q}$, then it can be shown that the joint Tsallis entropy is pseudo-additive

$$H_\alpha(\boldsymbol{p}, \boldsymbol{q}) = H_\alpha(\boldsymbol{p}) + H_\alpha(\boldsymbol{q}) + (1-\alpha)H_\alpha(\boldsymbol{p})H_\alpha(\boldsymbol{q}),$$

whereas the joint Shannon entropy is additive: $H(\boldsymbol{p}, \boldsymbol{q}) = H(\boldsymbol{p}) + H(\boldsymbol{q})$. Pseudo-additivity implies that Tsallis entropy has a nonextensive property for statistical independent systems. Further, standard thermodynamics is extensive because of the short-range nature of the interaction between subsystems of a composite system. In other words, when a system is composed of two statistically independent subsystems, then Shannon entropy of the composite system is just the sum of entropies of the individual systems, and hence the correlations between the subsystems are not accounted for. Tsallis entropy, however, does take into account these correlations due to its pseudo-additivity property. Figure 2.2 depicts Tsallis entropy of a Bernoulli distribution $\boldsymbol{p} = (p, 1-p)$, for different values of the entropic index. As illustrated in Figure 2.2, the measure of uncertainty is at a minimum when Shannon entropy is used, and for $\alpha \geq 1$ it decreases as the parameter α increases. Furthermore, Tsallis entropy attains a maximum uncertainty when its exponential order α is equal to zero.

Definition 2.3.1 *Let $\boldsymbol{p}_1, \boldsymbol{p}_2, \ldots, \boldsymbol{p}_n$ be n probability distributions. The Jensen-Tsallis divergence is defined as*

$$D_\alpha^{\boldsymbol{\omega}}(\boldsymbol{p}_1, \ldots, \boldsymbol{p}_n) = H_\alpha\left(\sum_{i=1}^{n} \omega_i \boldsymbol{p}_i\right) - \sum_{i=1}^{n} \omega_i H_\alpha(\boldsymbol{p}_i), \tag{2.3}$$

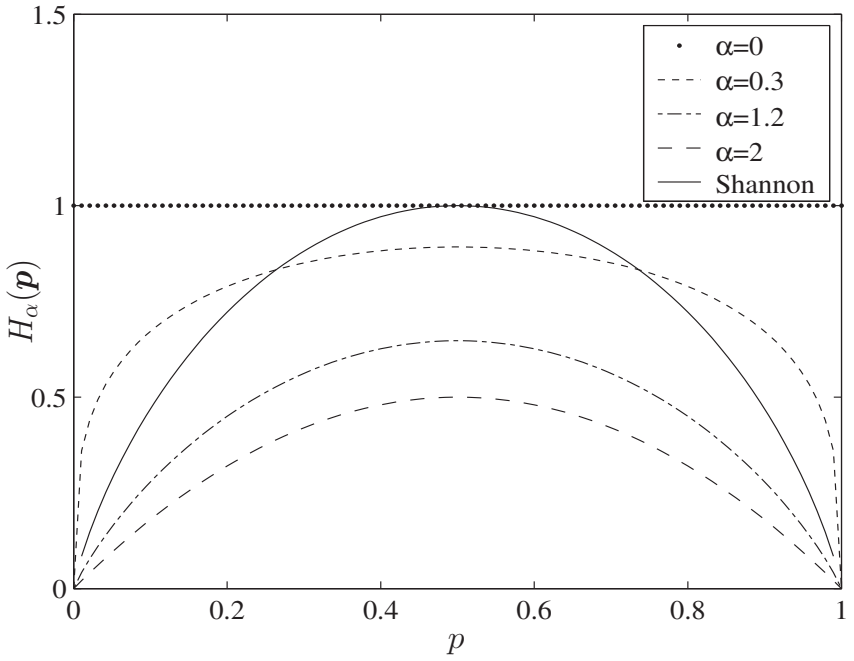

FIGURE 2.2: Tsallis entropy $H_\alpha(\boldsymbol{p})$ of a Bernoulli distribution $\boldsymbol{p} = (p, 1-p)$ for different values of α.

where $H_\alpha(\boldsymbol{p})$ is Tsallis entropy, and $\boldsymbol{\omega} = (\omega_1, \omega_2, \ldots, \omega_n)$ is a weight vector such that $\sum_{i=1}^n \omega_i = 1$ and $\omega_i \geq 0$.

Using the Jensen inequality, it is easy to check that the Jensen-Tsallis divergence is nonnegative for $\alpha > 0$. It is also symmetric and vanishes if and only if all the probability distributions are equal, for all $\alpha > 0$.

The following result establishes the convexity of the Jensen-Tsallis divergence of a set of probability distributions [30].

Proposition 2.3.2 *For $\alpha \in [1, 2]$, the Jensen-Tsallis divergence D_α^ω is a convex function of $\boldsymbol{p}_1, \boldsymbol{p}_2, \ldots, \boldsymbol{p}_n$.*

In the sequel, we will restrict $\alpha \in [1, 2]$, unless specified otherwise. In addition to its convexity property, the Jensen-Tsallis divergence is an adapted measure of disparity among n probability distributions as shown in the next result [28].

Proposition 2.3.3 *The Jensen-Tsallis divergence D_α^ω achieves its maximum value when $\boldsymbol{p}_1, \boldsymbol{p}_2, \ldots, \boldsymbol{p}_n$ are degenerate distributions, that is $\boldsymbol{p}_i = (\delta_{ij})$, where $\delta_{ij} = 1$ if $i = j$ and 0 otherwise.*

2.3.2 MODIFIED SPSA OPTIMIZATION ALGORITHM

The implementation of SPSA depends on a simple "simultaneous perturbation" approximation to the gradient [31]. It uses only two measurements of the loss function in each iteration independent of the number of the problem dimension. In contrast, the standard stochastic approximation method like finite difference stochastic approximation varies the variables one at a time. If the number of terms being optimized is equal to ν, then the finite-difference method takes 2ν measurements of the objective function at each iteration.

Next we propose a modified SPSA algorithm that maximizes a real-valued loss function $\mathcal{L}(\boldsymbol{\ell})$, where $\boldsymbol{\ell}$ denotes a ν-dimensional transformation parameter vector that needs to be optimally found by maximizing $\mathcal{L}(\boldsymbol{\ell})$. The proposed SPSA algorithm starts from an initial guess of $\boldsymbol{\ell}$, where the iteration process depends on the above-mentioned highly efficient "simultaneous perturbation" approximation to the gradient $g(\boldsymbol{\ell}) \equiv \nabla\mathcal{L}(\boldsymbol{\ell})$. It is assumed that $\mathcal{L}(\boldsymbol{\ell})$ is a differentiable function of $\boldsymbol{\ell}$ and that the maximum point $\boldsymbol{\ell}^*$ corresponds to a zero point of the gradient, i.e.,

$$g(\boldsymbol{\ell}^*) = \nabla\mathcal{L}(\boldsymbol{\ell}^*) = 0. \tag{2.4}$$

Let $y(\boldsymbol{\ell}) = \mathcal{L}(\boldsymbol{\ell}) + \textit{noise}$, and $\hat{\boldsymbol{\ell}}$ be the estimate of $\boldsymbol{\ell}$. Then the gradient estimate $\hat{g}(\hat{\boldsymbol{\ell}})$ in the k-th iteration is given by

$$\hat{g}_k(\hat{\boldsymbol{\ell}}_k) = \frac{y(\hat{\boldsymbol{\ell}}_k + c_k\boldsymbol{\varepsilon}_k) - y(\hat{\boldsymbol{\ell}}_k - c_k\boldsymbol{\varepsilon}_k)}{2c_k\boldsymbol{\varepsilon}_k}, \tag{2.5}$$

where c_k is the perturbation coefficient, and $\boldsymbol{\varepsilon}_k$ is the ν-dimensional simultaneous perturbation vector that is Monte Carlo-generated. At the end of each iteration, the $\hat{\boldsymbol{\ell}}_k$ estimate is updated using the standard stochastic approximation form

$$\hat{\boldsymbol{\ell}}_{k+1} = \hat{\boldsymbol{\ell}}_k + a_k\hat{g}_k(\hat{\boldsymbol{\ell}}_k). \tag{2.6}$$

Note that the choice of the gain sequences a_k and c_k should satisfy some typical stochastic approximation conditions [31].

2.3.3 MODALITY TRANSFORMATION

Assume that I and J are normalized images, that is $I(\boldsymbol{x}), J(\boldsymbol{x}) \in [0, 1]$. By looping through all pixel locations, the joint histogram $h(I, J)$ of the images I and J may be written as:

$$h\big(\lfloor I(\boldsymbol{x})N\rfloor, \lfloor J(x)N\rfloor\big) := h\big(\lfloor I(\boldsymbol{x})N\rfloor, \lfloor J(\boldsymbol{x})N\rfloor\big) + 1, \tag{2.7}$$

where N is the number of bins, and $\lfloor\alpha\rfloor$ denotes the floor function (largest integer not greater than α).

Using the following optimization scheme

$$J_T(\boldsymbol{x}) = \arg\max_i \, h\big(\lfloor iN \rfloor, \lfloor J(\boldsymbol{x})N \rfloor\big), \tag{2.8}$$

we can transform the moving image J into another image J_T that has a similar modality representation as I. In other words, the iterative scheme given by Eq. (2.8) finds every pixel value i in the image I that overlaps most often with a pixel value in the image J. It is worth pointing out that in medical images two regions may have the same intensity value in one modality. However, in another modality both regions may have completely different intensity values.

2.3.4 Proposed Algorithm

The proposed algorithm consists of the following main steps:

(i) Find the conditional intensity probabilities

$$\boldsymbol{p}_i = \boldsymbol{p}_i\left(J(\Phi_{\boldsymbol{\ell}}(\boldsymbol{x}))|I(\boldsymbol{x})\right) = (p_{ij})_{j=1,\ldots,n}, \quad \forall i = 1, \ldots, n, \tag{2.9}$$

where $p_{ij} = P(Y = y_j | X = x_i),\ j = 1, \ldots, n.$

(ii) Find the optimal parameter vector $\boldsymbol{\ell}^\star = (\boldsymbol{t}^\star, \theta^\star)$ of the Jensen-Tsallis objective function

$$\boldsymbol{\ell}^\star = \arg\max_{\boldsymbol{\ell}} \, D_\alpha^{\boldsymbol{\omega}}(\boldsymbol{p}_1, \ldots, \boldsymbol{p}_n) \tag{2.10}$$

using the modified SPSA optimization algorithm.

Note that if the images I and J are exactly matched, then $\boldsymbol{p}_i = (\delta_{ij})$ and by Proposition 2.3.3, the Jensen-Tsallis divergence is therefore maximized. The conditional probability p_{ij} is estimated using the normalized conditional histogram. In other words, p_{ij} estimates the probability that a pixel has intensity j in the transformed moving image J, given that is has an intensity i in the fixed image I.

2.4 Experimental Results

The results of the proposed multimodal image registration algorithm are presented in this section. We tested the performance of the proposed approach on a medical imaging dataset. Figure 2.3 shows the medical images that were used to validate the performance of the proposed algorithm in comparison to MI and NMI approaches. These multimodal images were obtained from the Vanderbilt Retrospective Image Registration

Evaluation (RIRE) database [32], which contains magnetic resonance (MR), computer tomography (CT), and positron emission tomography (PET) images for various patients. Each patient dataset contains MR images from several protocols, including T1-weighted, T2-weighted, PD-weighted, etc. Most of these data sets contain MR, CT, and PET images. Figure 2.3 shows the images from the patient 5 data set, where the MR-T1, CT, and PET images are shown in Figure 2.3(a), (c), and (d), respectively. Figure 2.3(b) shows a noisy MR image, obtained by adding a Rician noise to the MR-T1 image. These images are available online at [33]. It is worth pointing out that multimodal medical images are used to provide as much information about the patient as possible. MR and CT images provide complementary information, with CT proving a good visual description of bone tissue, whereas soft tissues are better visualized by MR images. Moreover, MR and CT are anatomical modalities that display geometric features of the object. On the other hand, PET is a functional modality that displays a metabolic map of the object and captures very reliably the metabolic activity. For example, in radiation treatment for cancer therapy, CT and PET are commonly used modalities to define cancerous lesions and plan treatment strategies. CT and PET modalities display different, but complementary information and involve different acquisition processes. These differences make registering CT and PET data one of the most challenging medical image registration problems.

2.4.1 Modality Transformation

To boost the accuracy of the proposed multimodal image registration, we apply the histogram-based modality transformation to the moving image prior to maximizing the Jensen-Tsallis divergence between the fixed and transformed moving images. This modality transformation involves finding the maxima of the joint histogram of both images to transform one image modality representation into another modality, allowing more accurate image registration results for MI, NMI, and the proposed approach.

Figure 2.4 illustrates the idea behind the histogram-based modality transformation, where the sparsity patterns of the conditional probabilities of MR-T1 image given PET image before and after modality transformation are shown in Figure 2.4(a) and Figure 2.4(b), respectively.

2.4.2 Registration Functions

In all the experiments we used an entropic index $\alpha = 2$ and the normalized histogram of the fixed image as the weight vector ω for the Jensen-Tsallis divergence. In the case of images from the same modality, that is MR-T1 to MR-T1 and MR-T1 to noisy MR-T1, we used the proposed algorithm directly without any modality transformation. However, for aligning multimodal images MR-T1 to CT and MR-T1 to PET,

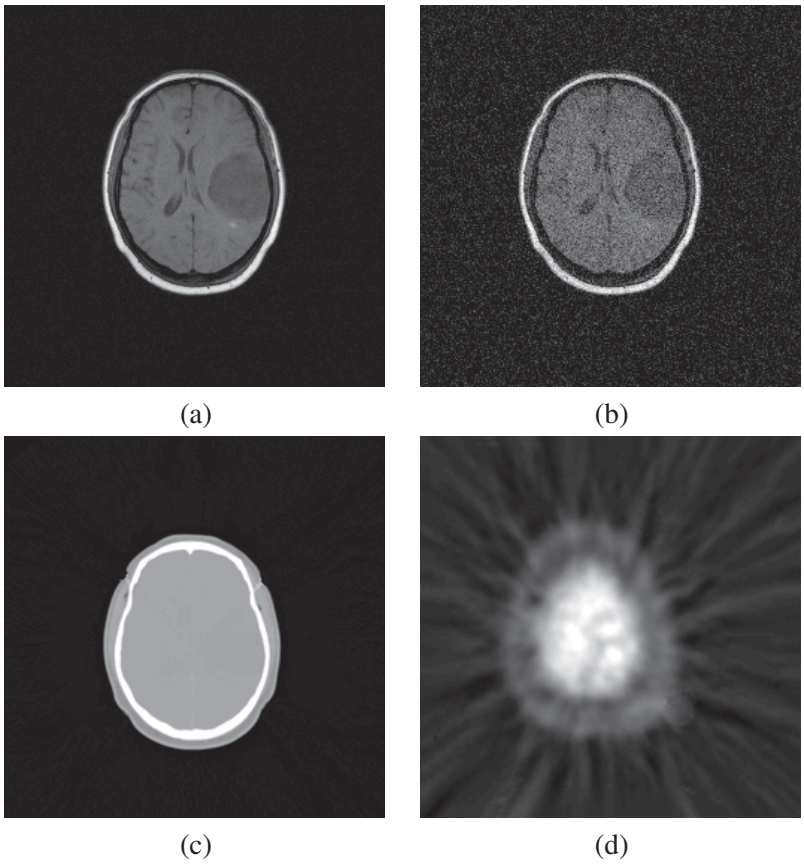

FIGURE 2.3: Multimodal images from the patient 5 dataset: (a) MR-T1 image, (b) noisy MR-T1 image, (c) CT image, (d) PET image.

we used the histogram-based modality transformation to transform CT and PET images into the MR-T1 modality. For fair comparison, it is worth mentioning that we also used modality transformation to align MR-T1 to CT and MR-T1 to PET when comparing the performance of the proposed algorithm to MI and NMI-based approaches.

To validate the proposed approach, we first applied a Euclidean transformation $\Phi_{\boldsymbol{\ell}}$ with different values of the parameter vector $\boldsymbol{\ell} = (t_x, t_y, \theta)$ to the fixed images shown in Figure 2.3. Then, we run iteratively the modified SPSA algorithm to find the optimal parameter vector $\boldsymbol{\ell}^* = (t_x^\star, t_y^\star, \theta^\star)$. We also compared the image alignment results of the proposed approach to MI and NMI-based registration methods.

An ideal registration function that measures the dissimilarity between two images should be smooth and concave with respect to different transformation parameters. Also, the global maximum of the registration function should be close to the correct transformation parameters that align two images perfectly [57]. Moreover, the capture range around the global maximum should be as large as possible, and the number of local maxima of the registration function should be as small as possible. These criteria will be used to

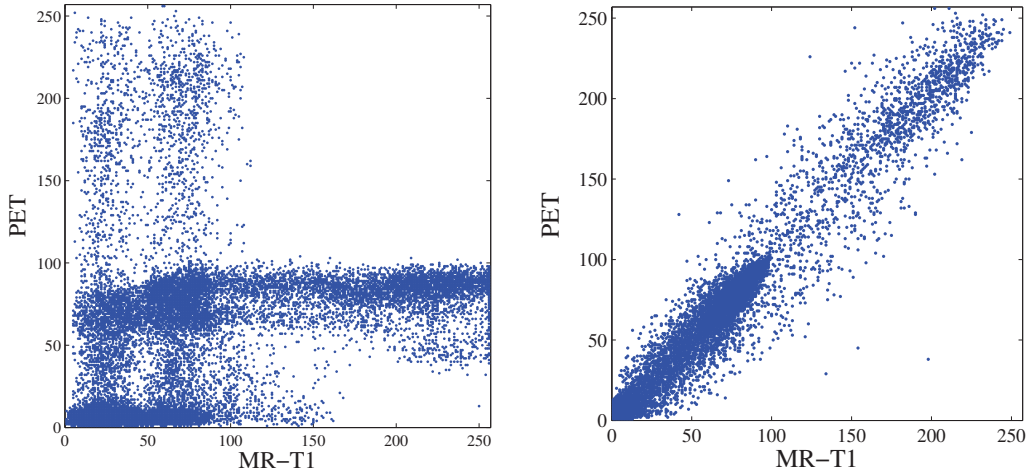

FIGURE 2.4: 2D plots of conditional probabilities of MR-T1 given PET: (a) before modality transformation; (b) after modality transformation.

evaluate the registration functions generated by MI, NMI, and Jensen-Tsallis respectively. The registration function of the proposed algorithm can be generated by computing the Jensen-Tsallis of two images under all possible transformations. For the medical images used in our experiments, their relative transformation parameters can be determined with the aid of four fiducial markers implanted in the patients. In other words, we can first align all testing images into the same space by using the four fiducial markers, and then compute the Jensen-Tsallis measure between two testing images under different rigid-body transformations, thereby obtaining a registration function of Jensen-Tsallis. Similarly, the registration functions of MI and NMI can be obtained.

The registration functions of MI, NMI, and Jensen-Tsallis with respect to different rotation and translation parameters are depicted in Figure 2.5. It is evident from Figure 2.5 that the registration functions of Jensen-Tsallis are much smoother than those of MI and NMI. Moreover, the capture range in the registration function of Jensen-Tsallis is considerably large. In particular, the change of registration function with respect to rotations is smoothly extended relatively far from the global maximum, indicating a better performance of the proposed approach.

2.4.3 ROBUSTNESS AND ACCURACY

We tested the accuracy and robustness of the proposed method by comparing the conditional probabilities of the moving image given the fixed image after applying various alignment methods. The more linear conditional probability indicates more accurate registration method. Note that if the fixed image I and the

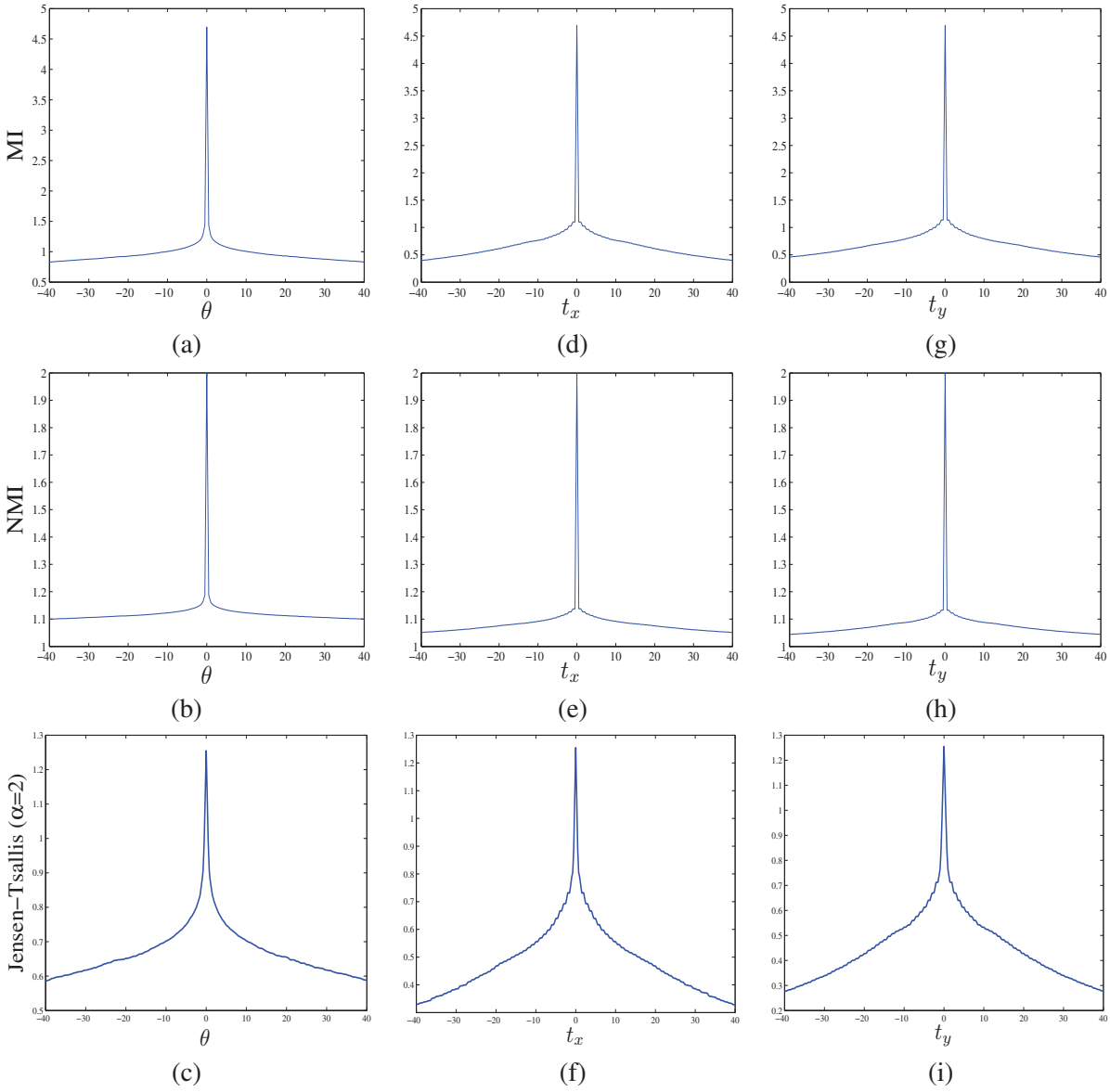

FIGURE 2.5: Registration functions of MI, NMI, and proposed approach in aligning MRI-T1 images. From top to bottom: (a), (b) and (c) rotation only; (d), (e) and (f) translation along x-axis; (g), (h) and (i) translation along y-axis.

moving image J are exactly matched, then the conditional probability plots a straight diagonal line.

The conditional probabilities before and after aligning different images modalities with the MR-T1 image using MI, NMI, and Jensen-Tsallis respectively, are presented in Figure 2.6 through Figure 2.9. The conditional probabilities in Figure 2.6 represent the alignment of MR-T1 to another image of the same modality. The plots in the three cases are close to linear, indicating the effectiveness of the three methods in multi-modality image registration. Figure 2.7 shows that the proposed approach is more robust to noise than MI

and NMI. Note that the presence of noise causes the joint distribution to be less correlated, and thus increases the joint entropy estimate, resulting in a lower registration accuracy for MI and NMI-based approaches.

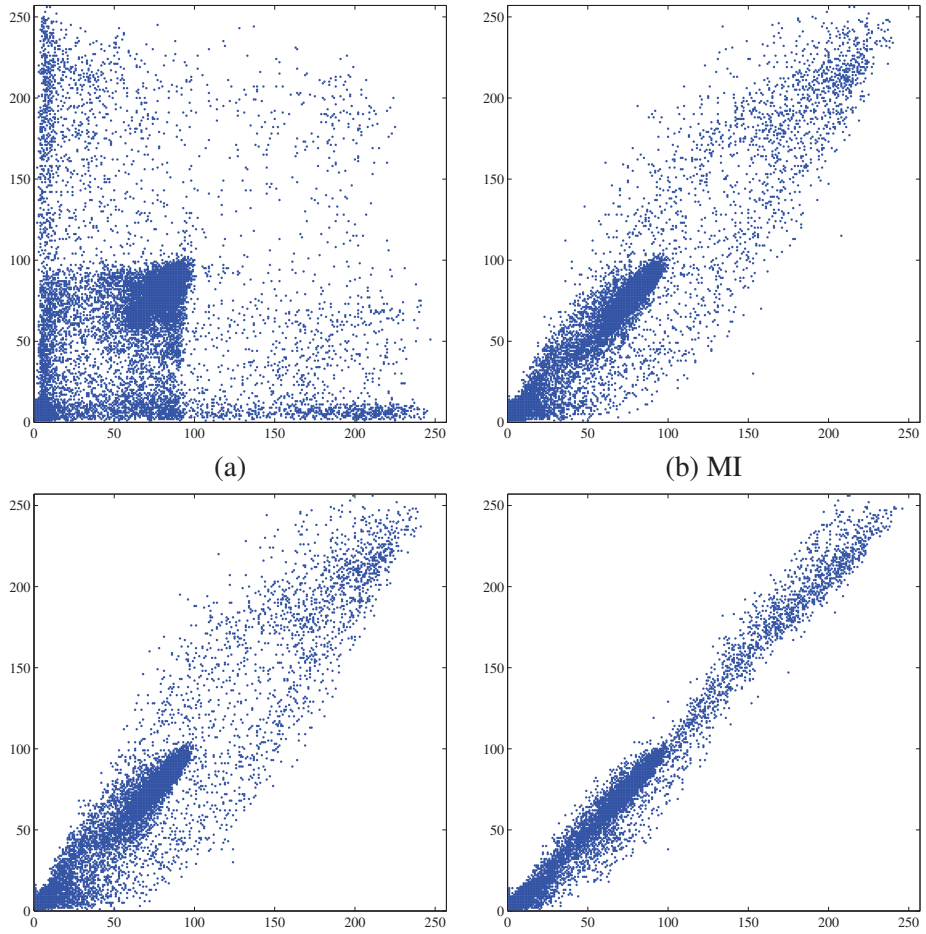

FIGURE 2.6: 2D plots of conditional probabilities for MR-T1 image alignment: (a) after applying Euclidean transformation $\Phi_{\boldsymbol{\ell}}$ to fixed image with parameter vector $\boldsymbol{\ell} = (5, 5, 5)$; (b)-(d) after aligning the images by MI, NMI, and proposed approach, respectively.

Figure 2.8 and Figure 2.9 depict the conditional probabilities for aligning MRI-T1 with CT and PET images respectively, after applying modality transformation to CT and PET images. From these figures, it is evident that the linearity of the conditional probabilities indicates the effectiveness and a much improved registration accuracy of the proposed algorithm in comparison to MI and NMI.

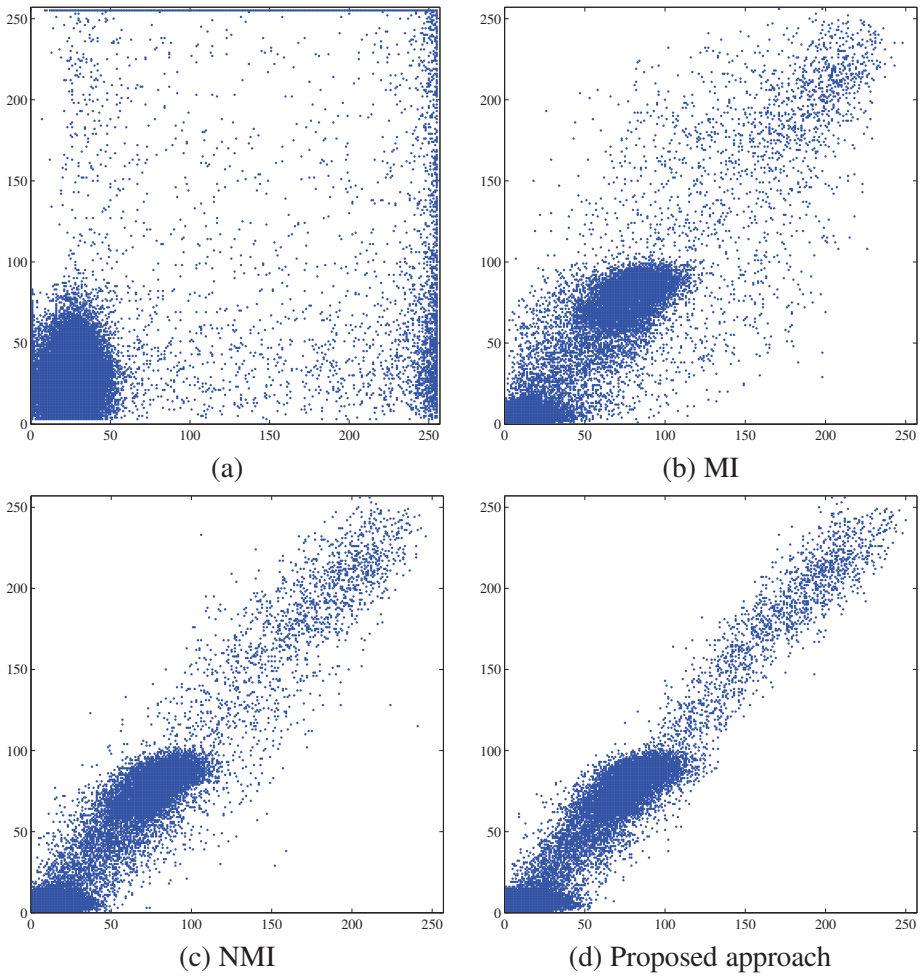

FIGURE 2.7: 2D plots of conditional probabilities for various alignment methods of MR-T1 to noisy MR-T1 images: (a) after applying Euclidean transformation $\Phi_{\boldsymbol{\ell}}$ to fixed image with parameter vector $\boldsymbol{\ell} = (5, 5, 5)$; (b)-(d) after aligning the images by MI, NMI, and proposed approach, respectively.

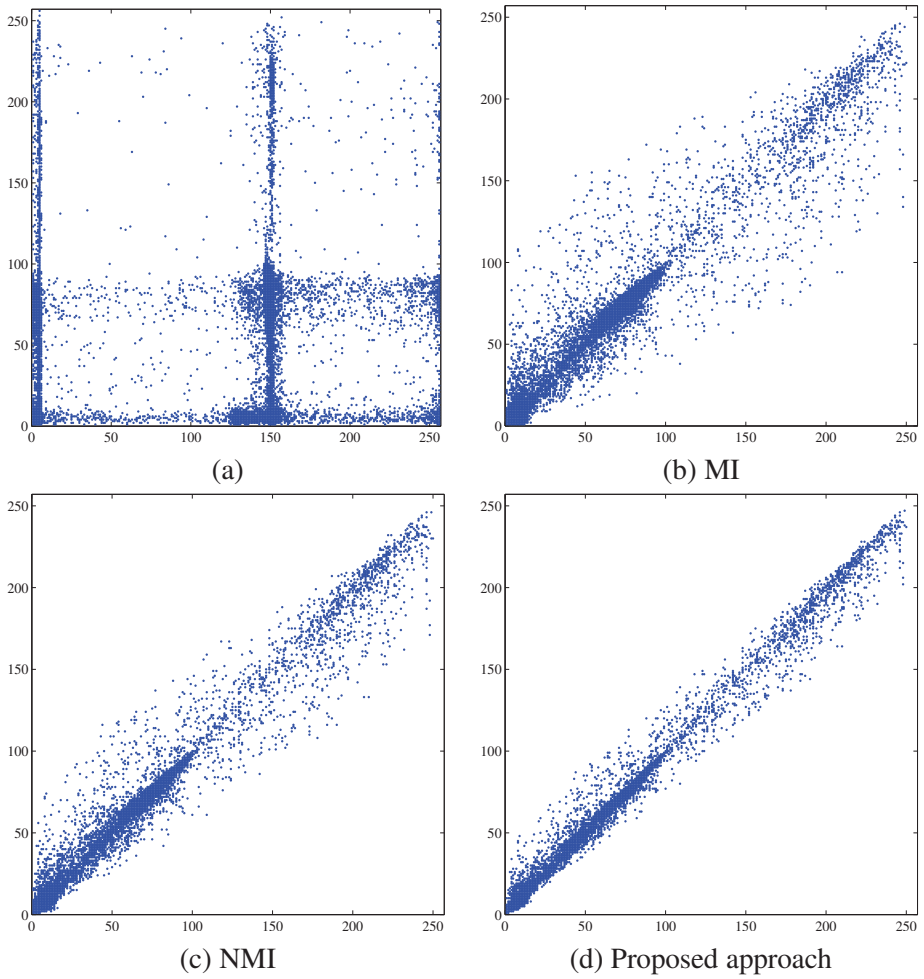

FIGURE 2.8: 2D plots of conditional probabilities for various alignment methods of MR-T1 to CT images: (a) after applying Euclidean transformation $\Phi_{\boldsymbol{\ell}}$ to fixed image with parameter vector $\boldsymbol{\ell} = (5, 5, 5)$; (b)-(d) after applying modality transformation and then aligning the images by MI, NMI, and proposed approach, respectively.

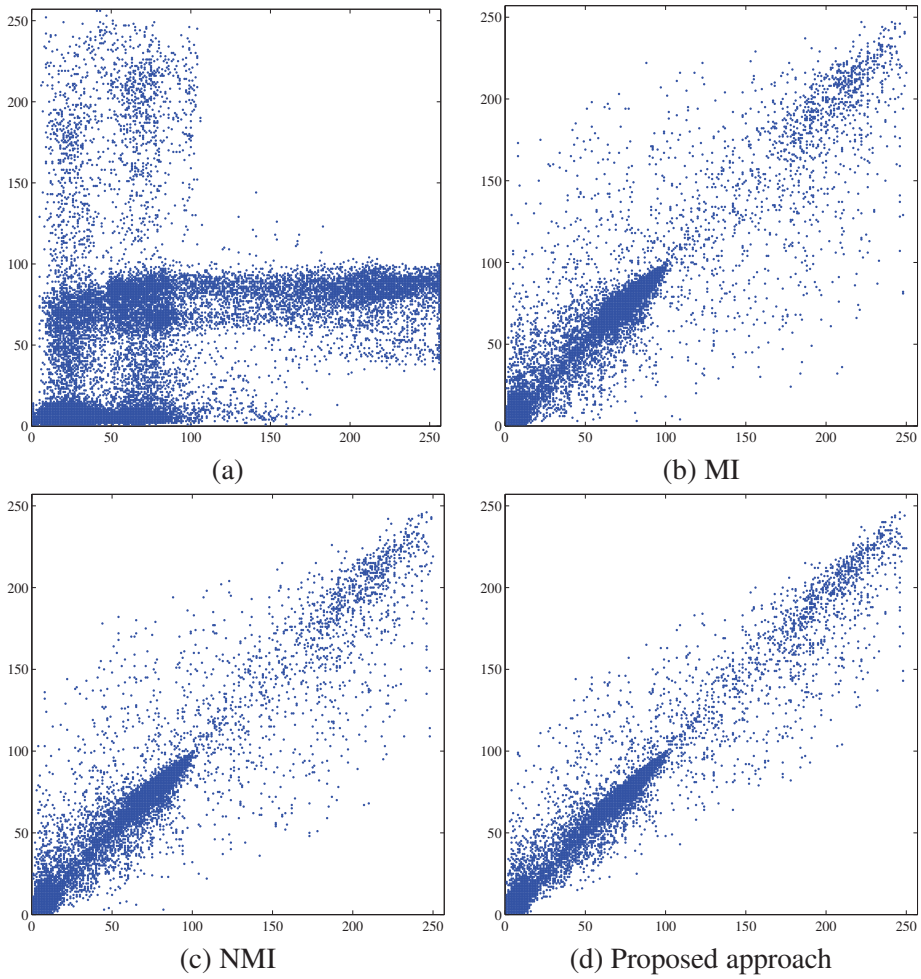

FIGURE 2.9: 2D plots of conditional probabilities for various alignments methods of MR-T1 to PET images: (a) after applying Euclidean transformation $\Phi_{\boldsymbol{\ell}}$ to fixed image with parameter vector $\boldsymbol{\ell} = (5, 5, 5)$; (b)-(d) after applying modality transformation and then aligning the images by MI, NMI, and proposed approach, respectively.

CHAPTER 3

NONRIGID IMAGE REGISTRATION USING A GENERALIZED ENTROPIC SIMILARITY

In this Chapter, we introduce a nonrigid image registration technique by optimizing a generalized information-theoretic similarity measure using the quasi-Newton method as an optimization scheme and cubic B-splines for modeling the nonrigid deformation field between the fixed and moving 3D image pairs. To achieve a compromise between the nonrigid registration accuracy and the associated computational cost, we implement a three-level hierarchical multi-resolution approach such that the image resolution is increased in a coarse to fine fashion. Experimental results are provided to demonstrate the registration accuracy of our approach. The feasibility of the proposed method is demonstrated on a 3D magnetic resonance data volume and also on clinically acquired 4D CT image data sets.

3.1 INTRODUCTION

Nonrigid image registration is of paramount importance in the field of medical imaging and has sparked a flurry of research interest in many other applications of image analysis such as remote sensing, movie editing, and archeology [7]. In recent years, various techniques have been proposed in the literature to tackle the nonrigid image registration problem [6, 7, 5]. Most of these techniques may be classified into two broad categories: feature-based and intensity-based methods. Feature-based approaches determine the registration at the feature locations, and an interpolation method is required at other locations. The registration accuracy for feature-based algorithms depends on the accuracy of the feature detector and involves detecting surface landmarks, edges and points [34, 35, 36, 37, 38]. On the other hand, intensity-based approaches employ

matching techniques that involve the use of distance measures, such as the normalized cross-correlation or the sum of squared differences (SSD) [7, 5]. A general framework for intensity-based registration methods relies on information-theoretic similarity measures. One such similarity measure is the mutual information (MI), which was proposed independently by Viola and Wells [10] and by Maes *et al.* [11]. The MI measure has been shown to be effective in the development of the intensity-based image registration because of its ability to register images from different modalities [9, 12]. Moreover, registration algorithms that maximize MI over rigid and affine transformations have reported impressive registration results [12]. Rueckert *et al.* [39] presented MI-based schemes for matching multimodal image pairs using B-splines to represent the deformation field on a regular grid. Most accurate methods for nonrigid registration are inspired by models from physics, either from elasticity [40, 41] or fluid mechanics [42, 43], but they are considered computationally expensive. Hence, several methods have been proposed based on various heuristics to approximate the underlying physical reality by alternative mathematical models [44]. Likar and Pernus [45] proposed a hierarchical image subdivision strategy by decomposing the nonrigid registration problem into an elastic interpolation of various local rigid registrations of sub-images of decreasing size. This algorithm is applicable to both intra- and inter-modal cases as it maximizes the local MI among sub-images. Although MI has been successfully applied to nonrigid image registration, it is worth noting that MI-based registration methods might have a limited performance, once the initial misalignment of the two images is large or equally the overlay region of the two images is relatively small [13]. Moreover, MI is sensitive to the changes that occur in the distributions (overlap statistics) as a result of changes in the region of overlap. To circumvent these limitations, a number of information-theoretic methods have been proposed to improve the robustness of MI-based registration, including the normalized mutual information (NMI) approach [17]. The NMI-based approach is a robust similarity measure that allows for fully automated intermodal image registration algorithms. Wang and Vemuri [46] introduced the cross-cumulative residual entropy (CCRE), which is a measure of entropy defined in terms of cumulative distribution functions. In this approach, the CCRE between two images to be registered is maximized over the space of smooth and unknown nonrigid transformations. The reported results showed a better performance than MI-based methods. In [47], Loeckx *et al.* proposed the conditional mutual information (cMI) as a new similarity measure for nonrigid image registration. This measure was calculated as the expected value of the cMI between the image intensities given the spatial distribution. Recently, Myronenko *et al.* [48, 49] proposed to minimize a residual complexity (RC) instead of mutual information. This approach deals with complex spatially-varying intensity distortions and produces accurate registration results.

In recent years, there has been a concerted research effort in statistical physics to explore the properties of Tsallis entropy, leading to a statistical mechanics that satisfies many of the properties of the standard theory [50]. Wachowiak *et al.* [51] introduced a generalized mutual information measure based on Tsallis entropy for 2D-3D multimodal biomedical image registration, and showed that their metric often produces fewer misregistrations compared to the MI approach. However, no results on nonrigid image registration were reported. Extending entropic methods to nonrigid image registration is the main focus of this Chapter. In the proposed approach, we model the nonrigid transformation of image coordinates using cubic B-splines [52]. Because of their attractive characteristics, such as inherent control of smoothness, separability in multiple dimensions and computational efficiency, B-splines are used widely in the literature to model nonrigid deformations [39, 48, 46, 47, 53].

In this Chapter, we propose a nonrigid image registration method by optimizing the Jensen-Tsallis (JT) similarity measure using the quasi-Newton L-BFGS-B method [55] as an optimization scheme and cubic B-splines for modeling the nonrigid deformation field between the fixed and moving 3D image pairs. The analytical gradient of the JT similarity is derived so that we can achieve an efficient and accurate nonrigid registration. In order to achieve a compromise between the nonrigid registration accuracy and the associated computational cost, we implement a three-level hierarchical multi-resolution approach such that the image resolution is increased, along with the resolution of the control mesh, in a coarse to fine fashion. Experimental results are provided to demonstrate the registration accuracy of the proposed approach in comparison to RC and NMI approaches. The feasibility of the proposed algorithm is demonstrated on medical images from magnetic resonance imaging with different protocols and also on clinically acquired 4D CT image data sets.

The rest of the Chapter is organized as follows. In Section 3.2, we describe in detail the proposed method, including the JT divergence and its main properties, the problem formulation, the deformation model, the estimation of the JT similarity and its derivative, as well as the summary of our proposed algorithm. Section 3.3 provides experimental results on a medical imaging data set that demonstrate the effectiveness and superior performance of our method compared to RC and NMI approaches.

3.2 Proposed Method

In this section, we present the details of our proposed nonrigid image registration approach. First, we introduce the JT similarity measure that calculates how well the fixed and deformed image match. Then, we describe the transformation model that defines the space in which the best solution is found. Next,

we present the optimization and derivative of the analytic gradient of the JT cost function with respect to nonrigid transformation parameters. Finally, we summarize our nonrigid registration algorithm.

3.2.1 JENSEN-TSALLIS (JT) SIMILARITY

Let $\boldsymbol{p}_1, \boldsymbol{p}_2, \ldots, \boldsymbol{p}_n$ be n probability distributions. Recall that the Jensen-Tsallis (JT) divergence is defined as

$$D_\alpha^{\boldsymbol{\omega}}(\boldsymbol{p}_1, \ldots, \boldsymbol{p}_n) = H_\alpha\left(\sum_{i=1}^{n} \omega_i \boldsymbol{p}_i\right) - \sum_{i=1}^{n} \omega_i H_\alpha(\boldsymbol{p}_i). \tag{3.1}$$

where $H_\alpha(\boldsymbol{p})$ is Tsallis entropy, and $\boldsymbol{\omega} = (\omega_1, \omega_2, \ldots, \omega_n)$ is a weight vector such that $\sum_{i=1}^{n} \omega_i = 1$ and $\omega_i \geq 0$.

Proposition 3.2.1 *The upper-bound of the JT divergence is given by* $D_\alpha^{\omega}(\boldsymbol{p}_1, \ldots, \boldsymbol{p}_n) \leq H_\alpha(\omega)$.

Proof: Since the JT divergence is a convex function of $\boldsymbol{p}_1, \ldots, \boldsymbol{p}_n$, it achieves its maximum value when Tsallis entropy of the $\boldsymbol{\omega}$-weighted average of degenerate probability distributions, achieves its maximum value as well. Assigning weights ω_i to the degenerate distributions $\boldsymbol{\delta}_1, \boldsymbol{\delta}_2, \ldots, \boldsymbol{\delta}_n$, where $\boldsymbol{\delta}_i = (\delta_{ij})$, the following upper bound

$$D_\alpha^{\boldsymbol{\omega}}(\boldsymbol{p}_1, \ldots, \boldsymbol{p}_n) \quad \leq \quad H_\alpha\left(\sum_{j=1}^{n} \omega_i \boldsymbol{\delta}_i\right) = H_\alpha(\boldsymbol{\omega}).$$

is achieved. ■

Since $H_\alpha(\boldsymbol{\omega})$ attains its maximum value when the weights are uniformly distributed (i.e. $\omega_i = 1/n, \forall i$), it follows that a tight upper bound of the JT divergence is given by

$$D_\alpha^{\omega}(\boldsymbol{p}_1, \ldots, \boldsymbol{p}_n) \leq H_\alpha(1/n, \ldots, 1/n) = \log_\alpha n \tag{3.2}$$

If we are measuring the similarity, $S_\alpha^{\omega}(\boldsymbol{p}_1, \ldots, \boldsymbol{p}_n)$, between densities, then $S_\alpha^{\omega}(\boldsymbol{p}_1, \ldots, \boldsymbol{p}_n)$ should satisfy the conditions

$$S_\alpha^{\omega}(\boldsymbol{p}_1, \ldots, \boldsymbol{p}_n) \geq 0$$

$$S_\alpha^{\omega}(\boldsymbol{p}_1, \ldots, \boldsymbol{p}_n) = \mathsf{max}$$

where max is the maximum similarity possible on the scale of measurement being used, and often this will be unity. Therefore, using Eq. (3.2) we may define the JT similarity measure as follows:

$$S_\alpha^{\boldsymbol{\omega}}(\boldsymbol{p}_1, \ldots, \boldsymbol{p}_n) = \frac{\varrho(D_\alpha^{\boldsymbol{\omega}}(\boldsymbol{p}_1, \ldots, \boldsymbol{p}_n)) - \varrho(\log_\alpha n)}{\varrho(0) - \varrho(\log_\alpha n)}, \tag{3.3}$$

where ϱ is a monotonous decreasing function such that $\varrho(\log_\alpha n) < \varrho(0)$. For simplicity, we choose $\varrho(x) = 1 - x$ as a monotonous decreasing function and by substituting this function into Eq. (3.3), the JT similarity measure becomes

$$S_\alpha^{\boldsymbol{\omega}}(\boldsymbol{p}_1, \ldots, \boldsymbol{p}_n) = 1 - \frac{D_\alpha^{\boldsymbol{\omega}}(\boldsymbol{p}_1, \ldots, \boldsymbol{p}_n)}{\log_\alpha n}. \tag{3.4}$$

It is worth pointing out that the main purpose of introducing the Jensen-Tsallis similarity measure $S_\alpha^{\boldsymbol{\omega}}$ is to use the limited memory quasi-Newton minimization method, which efficiently solves nonlinear and large-scale minimization problems.

3.2.2 Problem Statement

In the sequel, we will use the JT similarity measure, given by Eq. (3.4), as a matching criterion to solve the image alignment problem. Let I and J be two misaligned images to be registered, where I is the fixed image and J is the moving image. The moving image J is obtained by applying a deformation field $\boldsymbol{\Phi}$ to the fixed image I, as depicted in Figure 3.1. The deformation field $\boldsymbol{\Phi}$ is described by a transformation function $g(\boldsymbol{x}; \boldsymbol{\mu}) : V_J \to V_I$, where V_J and V_I are continuous domains on which J and I are defined, and $\boldsymbol{\mu}$ is a set of transformation parameters to be determined. The image alignment or registration problem may be formulated as an optimization problem

$$\hat{\boldsymbol{\mu}} = \arg\min_{\boldsymbol{\mu}} S_\alpha^{\boldsymbol{\omega}}\big(I(\boldsymbol{x}), J(g(\boldsymbol{x}; \boldsymbol{\mu}))\big). \tag{3.5}$$

To align the transformed moving image $J(g(\boldsymbol{x}; \boldsymbol{\mu}))$ to the fixed image I, we seek the set of transformation parameters $\boldsymbol{\mu}$ that minimize the JT cost function $S_\alpha^{\boldsymbol{\omega}}\big(I(\boldsymbol{x}), J(g(\boldsymbol{x}; \boldsymbol{\mu}))\big)$.

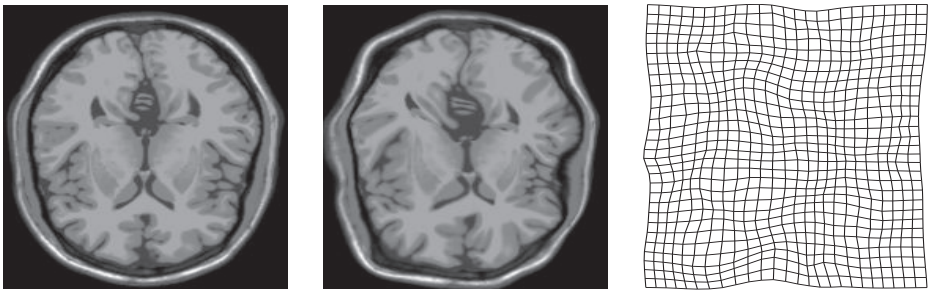

(a) (b) (c)

FIGURE 3.1: (a) Fixed image I; (b) Moving image J; (c) Deformation field $\boldsymbol{\Phi}$.

3.2.3 Transformation Model

Several transformation models have been proposed over the years to represent a nonrigid deformation field. In this Chapter, we model the transformation $g(\boldsymbol{x};\boldsymbol{\mu})$ using the free form deformation [53], which is based on cubic B-splines, and $\boldsymbol{\mu}$ represents the parameter vector of deformation coefficients. Let Φ denote a $n_x \times n_y \times n_z$ mesh of control points $\varphi_{i,j,k}$ with a uniform spacing Δ. Then, the 3D transformation at any point $\boldsymbol{x} = [x, y, z]^T$ in the moving image is interpolated using a linear combination of cubic B-spline convolution kernels as follows

$$g(\boldsymbol{x};\boldsymbol{\mu}) = \sum_{ijk} \eta_{ijk} \beta^{(3)} \left(\frac{\boldsymbol{x} - \varphi_{ijk}}{\Delta} \right), \tag{3.6}$$

where $\beta^{(3)}(\boldsymbol{x}) = \beta^{(3)}(x)\beta^{(3)}(y)\beta^{(3)}(z)$ is a separable cubic B-spline convolution kernel, and η_{ijk} are the deformation coefficients associated to the control points φ_{ijk}. The degree of nonrigidity can be adopted to a specific registration problem by varying the mesh spacing or the resolution of the mesh Φ of control points. The parameter vector $\boldsymbol{\mu} = (\eta_{ijk})$ represents the vector of deformation coefficients associated to the control points φ_{ijk}, where the indices i, j, k denote the coordinates of the control points on the mesh grid.

3.2.4 Optimization of the JT Similarity

We adopt a limited memory quasi-Newton method for solving the optimization problem given by Eq. (4.15). The calculation of the analytical gradient of the JT cost (similarity) function is necessary to not only avoid discretization errors but also to achieve an efficient and robust minimization scheme. Denote by $\mathcal{X} = \{x_1, x_2, \ldots, x_n\}$ and $\mathcal{Y} = \{y_1, y_2, \ldots, y_n\}$ the sets of pixel intensity values of the fixed image $I(\boldsymbol{x})$ and the deformed moving image $J(g(\boldsymbol{x};\boldsymbol{\mu}))$, respectively. Let X and Y be two random variables taking values in $\mathcal{X}$ and $\mathcal{Y}$. Then, we define the conditional intensity probability distributions $\boldsymbol{p}_i$ as follows:

$$\boldsymbol{p}_i = \boldsymbol{p}_i\big(J(g(\boldsymbol{x};\boldsymbol{\mu}))|I(\boldsymbol{x})\big) = (p_{ij})_{j=1,\ldots,n}, \quad \forall i = 1, \ldots, n,$$

where $p_{ij} = P(Y = y_j | X = x_i) = p\left(j|i;\boldsymbol{\mu}\right),\ j = 1, \ldots, n$. Note that in p_{ij} the parameter vector $\boldsymbol{\mu}$ is omitted for notational simplicity.

It is worth pointing out that if the images I and J are exactly matched, then $\boldsymbol{p}_i = (\delta_{ij})$ and by Proposition 2.3.3, the JT divergence is therefore maximized and consequently the JT similarity measure is minimized. By substituting Eq. (2.2) into Eq. (3.1), we obtain

$$D_\alpha^{\boldsymbol{\omega}}(\boldsymbol{p}_1, \ldots, \boldsymbol{p}_n) = \frac{1}{1-\alpha} \left[\sum_{j=1}^{n} \Big(\sum_{i=1}^{n} \omega_i p_{ij} \Big)^\alpha - \sum_{i=1}^{n} \omega_i \sum_{j=1}^{n} p_{ij}^\alpha \right]. \tag{3.7}$$

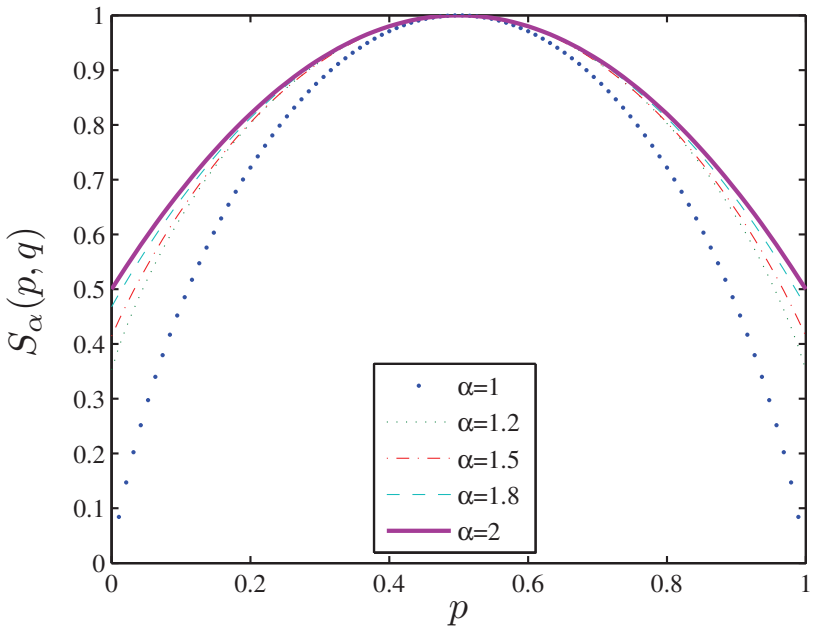

FIGURE 3.2: JT similarity $S_\alpha(\boldsymbol{p},\boldsymbol{q})$ between two Bernoulli distributions $\boldsymbol{p}=(p,1-p)$ and $\boldsymbol{q}=(1-p,p)$ for different values of α.

Figure 3.2 illustrates the JT similarity between two Bernoulli distributions $\boldsymbol{p}=(p,1-p)$ and $\boldsymbol{q}=(1-p,p)$ for different values of the entropic index. As shown in Figure 3.2, the highest similarity corresponds to the entropic index $\alpha=2$. In the sequel, we choose an entropic index $\alpha=2$. Thus, the JT divergence is reduced to

$$D_2^{\boldsymbol{\omega}}(\boldsymbol{p}_1,\ldots,\boldsymbol{p}_n)=-\sum_{j=1}^{n}\left(\sum_{i=1}^{n}\omega_i p_{ij}\right)^2+\sum_{i=1}^{n}\omega_i\sum_{j=1}^{n}p_{ij}^2, \tag{3.8}$$

and the JT similarity becomes

$$S_2^{\boldsymbol{\omega}}(\boldsymbol{p}_1,\ldots,\boldsymbol{p}_n)=1-\frac{D_2^{\boldsymbol{\omega}}(\boldsymbol{p}_1,\ldots,\boldsymbol{p}_n)}{\log_2 n}. \tag{3.9}$$

The calculation of the registration function is as follows. First, we calculate the conditional intensity probability distributions $\boldsymbol{p}_i, i=1,...,n$ between the fixed and deformed moving images. Then, we compute $D_2^{\boldsymbol{\omega}}(\boldsymbol{p}_1,\ldots,\boldsymbol{p}_n)$ according to the formula given by Eq. (10). Finally, we compute the similarity $S_2^{\boldsymbol{\omega}}(\boldsymbol{p}_1,\ldots,\boldsymbol{p}_n)$ given by Eq. (11), which represents our registration function. Note that we are using conditional (not marginal) probabilities to compute the JT similarity metric. Moreover, it is important to point out that n denotes the number of pixel values in the fixed image and also in the moving image. Thus, the number of conditional probabilities is also equal to n. In addition, both indices i and j in Eq. (3.8) run from 1 to n.

Conditional Intensity Probability Estimation

In a typical registration problem, direct access to the marginal and joint probability densities is not available and hence the densities must be estimated from the image data. Parzen windows (also known as kernel density estimators) can be used for this purpose. In this scheme, the densities are constructed by taking intensity samples from the image and super-positioning kernel functions centered on the elements of these samples. A variety of functions can be used as smoothing kernels with the requirement that they are smooth, symmetric, have zero mean and integrate to one. For example, boxcar, Gaussian and B-spline functions are suitable candidates. We propose to use the B-spline Parzen window to estimate the conditional intensity probability of the interpolated moving image given the fixed image. The advantage of using a B-spline kernel over a Gaussian kernel is that the B-spline kernel has a finite support region which is computationally attractive, as each intensity sample only affects a small number of bins and hence does not require an $N \times N$ loop to compute the metric value. Let $\beta^{(0)}$ be a zero-order spline Parzen window and $\beta^{(3)}$ be a cubic spline Parzen window, then the smoothed conditional probability of $J(g(\boldsymbol{x};\boldsymbol{\mu}))$ given $I(\boldsymbol{x})$ is expressed as:

$$p(j|i;\boldsymbol{\mu}) = \frac{p\left(j,i;\boldsymbol{\mu}\right)}{p_I\left(i\right)}, \tag{3.10}$$

where

$$p\left(j,i;\boldsymbol{\mu}\right) = \xi \sum_{\boldsymbol{x}\in V} \beta^{(0)}\left(i - \frac{I(\boldsymbol{x}) - f_I^0}{\Delta b_I}\right) \beta^{(3)}\left(j - \frac{J(g(\boldsymbol{x};\boldsymbol{\mu})) - f_J^0}{\Delta b_J}\right). \tag{3.11}$$

The normalization factor ξ ensures sum to one of the probabilities, and $I(\boldsymbol{x})$ and $J(g(\boldsymbol{x};\boldsymbol{\mu}))$ are samples of the fixed and interpolated moving images respectively. These samples are normalized by the minimum intensity value, f_I^0, f_J^0, and intensity range of each bin, Δb_I and Δb_J respectively.

The marginal probability of the fixed image is independent of the transformation parameters, and can be computed as:

$$p_I(i) = \xi \sum_{\boldsymbol{x}\in V} \beta^{(0)}\left(i - \frac{I(\boldsymbol{x}) - f_I^0}{\Delta b_I}\right) \tag{3.12}$$

Since the fixed image probability density function does not contribute to the cost function derivative, it does not need to be smooth. Hence, a zero order B-spline kernel is used.

By taking the derivative of the conditional probability with respect to $\boldsymbol{\mu}$, we get

$$\begin{aligned}\frac{\partial p(j|i;\boldsymbol{\mu})}{\partial \boldsymbol{\mu}} = \frac{\gamma}{p_I(i)\Delta b_J} \sum_{\boldsymbol{x}\in V} \beta^{(0)}\left(i - \frac{I(\boldsymbol{x}) - f_I^0}{\Delta b_I}\right) \\ \cdot \beta'^{(3)}\left(j - \frac{J(g(\boldsymbol{x};\boldsymbol{\mu})) - f_J^0}{\Delta b_J}\right) \\ \cdot \left(\frac{\partial J(t)}{\partial t}\bigg|_{t=g(\boldsymbol{x};\boldsymbol{\mu})}\right) \frac{\partial g(\boldsymbol{x};\boldsymbol{\mu})}{\partial \boldsymbol{\mu}},\end{aligned} \tag{3.13}$$

where $\partial J(t)/\partial t$ is the image gradient, and $\beta'^{(3)}$ is the derivative of the cubic spline kernel

$$\beta'^{(3)}(u) = \begin{cases} 0.0 & u \le -2 \\ 2u + 2 + \frac{1}{2}u^2 & -2 < u \le -1 \\ -2u - \frac{3}{2}u^2 & -1 < u \le 0 \\ -2u + \frac{3}{2}u^2 & 0 < u \le 1 \\ 2u - 2 - \frac{1}{2}u^2 & 1 < u \le 2 \\ 0.0 & u > 2 \end{cases} \tag{3.14}$$

3.2.5 Derivative of the JT Similarity

Now, taking the derivative of the JT divergence with respect to $\boldsymbol{\mu}$ yields:

$$\frac{\partial D_2^{\boldsymbol{\omega}}(\boldsymbol{p}_1,\ldots,\boldsymbol{p}_n)}{\partial \boldsymbol{\mu}} = \frac{\partial\left(-\sum_{j=1}^n \left(\sum_{i=1}^n \omega_i p_{ij}\right)^2\right)}{\partial \boldsymbol{\mu}} + \frac{\partial\left(\sum_{i=1}^n \omega_i \sum_{j=1}^n p_i^2\right)}{\partial \boldsymbol{\mu}}, \tag{3.15}$$

where

$$\begin{aligned}\frac{\partial\left(-\sum_{j=1}^n \left(\sum_{i=1}^n \omega_i p_{ij}\right)^2\right)}{\partial \boldsymbol{\mu}} &= -2\sum_{j=1}^n \left(\sum_{i=1}^n \omega_i p_{ij}\right) \frac{\partial\left(\sum_{i=1}^n \omega_i p_{ij}\right)}{\partial \boldsymbol{\mu}} \\ &= -2\sum_{j=1}^n \left(\sum_{i=1}^n \omega_i p_{ij}\right)\left(\sum_{i=1}^n \omega_i \frac{\partial p_{ij}}{\partial \boldsymbol{\mu}}\right)\end{aligned} \tag{3.16}$$

and

$$\frac{\partial\left(\sum_{i=1}^n \omega_i \sum_{j=1}^n p_{ij}^2\right)}{\partial \boldsymbol{\mu}} = \sum_{i=1}^n \omega_i \sum_{j=1}^n \frac{\partial p_{ij}^2}{\partial \boldsymbol{\mu}} = 2\sum_{i=1}^n \omega_i \sum_{j=1}^n p_{ij} \frac{\partial p_{ij}}{\partial \boldsymbol{\mu}}$$

Therefore,

$$\frac{\partial D_2^{\boldsymbol{\omega}}(\boldsymbol{p}_1,\ldots,\boldsymbol{p}_n)}{\partial \boldsymbol{\mu}} = -2\sum_{j=1}^n \left(\sum_{i=1}^n \omega_i p_{ij}\right)\left(\sum_{i=1}^n \omega_i \frac{\partial p_{ij}}{\partial \boldsymbol{\mu}}\right) + 2\sum_{i=1}^n \omega_i \sum_{j=1}^n p_{ij} \frac{\partial p_{ij}}{\partial \boldsymbol{\mu}} \tag{3.17}$$

Consequently, the JT similarity measure and its derivative are given by:

$$\begin{cases} S_2^{\boldsymbol{\omega}}(\boldsymbol{p}_1, \ldots, \boldsymbol{p}_n) = 1 - \dfrac{D_2^{\boldsymbol{\omega}}(\boldsymbol{p}_1, \ldots, \boldsymbol{p}_n)}{\log_2 n} \\ \dfrac{\partial S_2^{\boldsymbol{\omega}}(\boldsymbol{p}_1, \ldots, \boldsymbol{p}_n)}{\partial \boldsymbol{\mu}} = -\dfrac{\partial D_2^{\boldsymbol{\omega}}(\boldsymbol{p}_1, \ldots, \boldsymbol{p}_n)}{\partial \boldsymbol{\mu}} \times \dfrac{1}{\log_2 n} \end{cases} \tag{3.18}$$

3.2.6 Summary of the Proposed Algorithm

The proposed algorithm is implemented by changing the deformation in the moving image until the discrepancy between the moving and fixed images is minimized. The main algorithmic steps of our nonrigid image registration approach are summarized in Algorithm 2. First, the algorithm initializes the deformation field Φ by creating a uniform B-spline control grid with predefined spacing knots. Next, a 3-level hierarchical multi-resolution scheme is used to achieve the best compromise between the registration accuracy and the associated computational cost. As the hierarchical level increases the resolution of the control mesh is increased, along with the image resolution, in a coarse to fine fashion. In each hierarchical level, a limited-memory, quasi-Newton minimization scheme is used to find the optimum set of transformation parameters that reduce the JT cost function until the difference between the cost function values in two consecutive iterations is less than $\epsilon = 0.01$. The resolution of the optimum set of transformation parameters, at a courser level, is increased to be used as starting point for the next hierarchical level.

Algorithm 1 Proposed nonrigid registration approach

```
Initialize the deformation field Φ
for hierarchical_level = 1 to 3 do
    Calculate the cost function and its gradient as given by Eq. (3.18)
    repeat
        Use the quasi-Newton method to solve the optimization problem given by Eq. (3.5)
        Update the deformation field
        Recalculate the cost function and its gradient
    until the difference in consecutive iterates is less than ϵ = 0.01
    Increase the resolution of both the deformation field and the image.
end for
```

3.3 Experimental Results

We tested the performance of the proposed approach on a medical imaging data set that was obtained from the brainweb database at the Montreal Neurological Institute [56]. This data set contains a full 3D simulated brain magnetic resonance (MR) data volumes from several protocols, including T1-weighted (MR-T1), T2-

weighted (MR-T2), and proton density (MR-PD) with a variety of slice thicknesses, noise levels, and levels of intensity non-uniformity. All the corresponding slices from different protocols are originally aligned with each other. The images used in our experiments have $181 \times 217 \times 181$ voxels with a 1 mm voxel size in each dimension. To validate the nonrigid registration accuracy of the proposed method, we first applied both geometric and intensity distortions to the fixed image in order to generate moving image. Then, we aligned the moving image with the fixed image. We also compared the image registration results of our approach to RC and NMI approaches, which are implemented in the Medical Image Registration Toolbox (MIRT) [48] and in the Image Registration Toolkit (ITK) [39], respectively. In all the experiments we used an entropic index $\alpha = 2$ and the normalized histogram of the fixed image as the weight vector $\boldsymbol{\omega}$ for the JT similarity measure.

For the implementation of RC and NMI methods, we essentially model the nonrigid deformation field as a free-form deformation (FFD) based on B-splines and then we employ an iterative gradient descent scheme as an optimization algorithm. In all the experiments, the moving image is generated by applying a random perturbation to the corresponding fixed image using a thin-plate spline interpolation (TPS) such that the mean nonrigid displacement of the pixels, caused by the relative displacement between the fixed and generated moving images, is the ground truth deformation field μ_g. Moreover, it is important to mention that none of the three methods (NMI, RC, and proposed approach) uses TPS interpolation as its transformation model. Therefore, using TPS interpolation for generating moving image is not unfairly advantageous to any of these methods.

3.3.1 Registration Functions

An ideal registration function that measures the similarity between two images should be smooth and convex with respect to different transformation parameters. Also, the global minimum of the registration function should be close to the correct transformation parameters that align two images perfectly [57]. Moreover, the capture range around the global minimum should be as large as possible, and the number of local minima of the registration function should be as small as possible. These criteria will be used to evaluate the registration functions generated by NMI, RC, and the proposed approach. The registration function of our algorithm can be generated by computing the JT similarity between two images under all possible transformations. Similarly, the registration functions of NMI and RC can be obtained.

The registration functions of NMI, RC, and the proposed approach with respect to different rotation and translation parameters are shown in Figure 3.3. We can observe that the registration functions of the

proposed approach are much smoother than those of NMI and RC. In addition, the capture range in the registration function of our method is considerably large. In particular, the change of the registration function with respect to rotations is smoothly extended relatively far from the global minimum, indicating a better performance of the proposed approach.

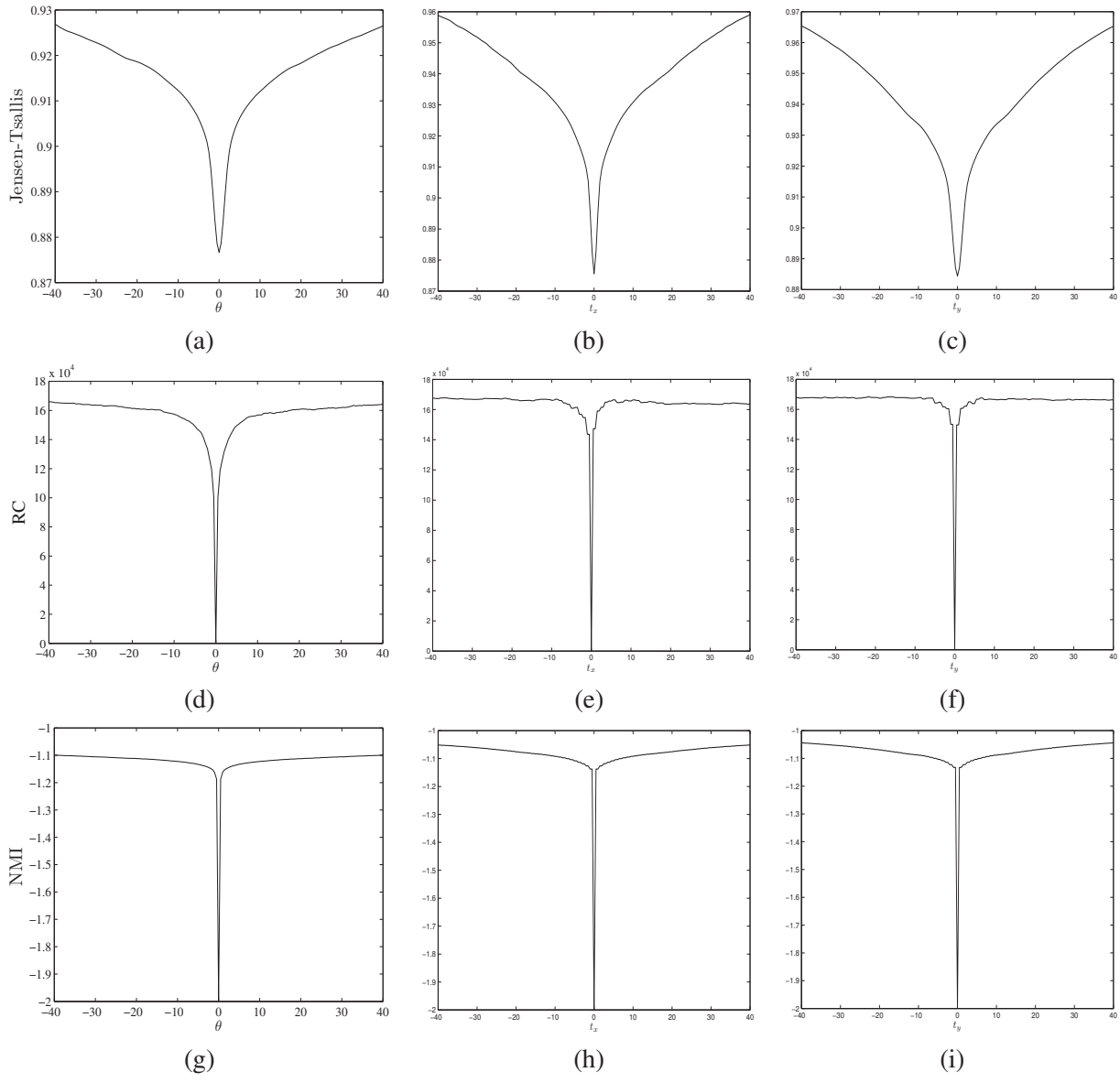

FIGURE 3.3: Registration functions of our approach, RC, and NMI in aligning MRI-T1 images. From top to bottom: (a), (d) and (g) rotation only; (b), (e) and (h) translation along x-axis; (c), (f) and (i) translation along y-axis.

3.3.2 MONOMODALITY TEST

In the first experiment, we distorted the fixed image MR-T1 with a known nonrigid transformation field, or the so-called ground truth deformation, μ_g. Then, we applied the proposed approach, RC and NMI algorithms. And finally, we compared the obtained deformations fields with the ground truth. Figure 3.4 shows the results obtained from this experiment. Note that the registered moving images obtained by the proposed method and the RC approach are visually more similar in shape to the moving image than the image produced by the NMI approach. Moreover, the estimated transformation field resulted from our approach is more similar to the ground truth than of those obtained using RC and NMI approaches. To measure the registration accuracy of the proposed method, we computed the mean ($\hat{\mu}_{\mathrm{MSE}}$) and standard deviation ($\hat{\sigma}_{\mathrm{MSE}}$) of the mean squared error (MSE) between the ground truth and estimated displacement vectors. Table 3.1 displays the MSE statistics of the estimated nonrigid deformation, when compared to the ground truth. The first column shows the mean ground truth deformation, which represents the magnitude of the displacement vector that is used to generate the moving images in each experiment. For each row twenty different transformation fields with this mean are generated and applied to the fixed image in order to generate the corresponding moving images. The second and third columns display the average and standard deviation of MSE for the generated twenty pairs of fixed-moving images. The results obtained using the proposed approach are considerably small compared to those of RC and NMI methods.

TABLE 3.1: Mean square error (MSE) statistics of the estimated nonrigid deformation.

μ_g	our method		RC		NMI	
	$\hat{\mu}_{\mathrm{MSE}}$	$\hat{\sigma}_{\mathrm{MSE}}$	$\hat{\mu}_{\mathrm{MSE}}$	$\hat{\sigma}_{\mathrm{MSE}}$	$\hat{\mu}_{\mathrm{MSE}}$	$\hat{\sigma}_{\mathrm{MSE}}$
2.1	0.4982	0.0325	0.5013	0.0251	0.7133	0.0436
3.0	0.5971	0.0843	0.5994	0.0413	0.8936	0.0362
4.6	0.7002	0.0157	0.7342	0.0321	1.0933	0.0733
5.1	0.7621	0.0241	0.7998	0.0379	1.4992	0.0536
5.7	0.7922	0.0252	0.8213	0.0317	1.6916	0.0837

In the second experiment, we used similar steps as in the first experiment, but this time we generated the moving image by distorting the fixed image with both intensity and geometric distortions. The intensity distortion is generated by corrupting the fixed image as follows [48]:

- $I(x,y) = I^{\gamma}(x,y) + \upsilon\dfrac{xy}{MN} + \dfrac{1}{K}\displaystyle\sum_{k=1}^{K}\exp\left(-\frac{\parallel [x;y] - \Psi_K \parallel^2}{2\sigma^2}\right)$
- Rescale I to $[0,1]$,

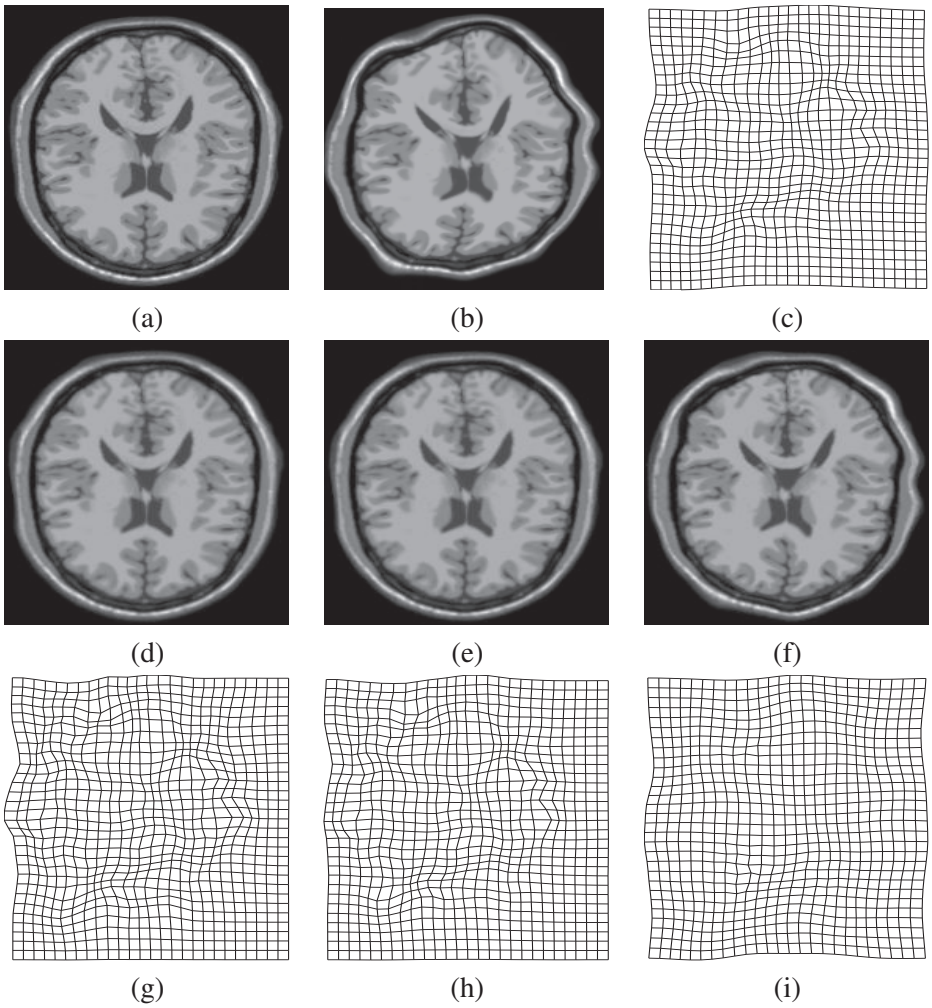

FIGURE 3.4: Geometric distortion experiment : (a) MR-T1 image; (b) distorted MR-T1 image with geometric distortion; (c) ground truth deformation field; (d)-(f) registered images using our approach, RC, and NMI, respectively; (g)-(i) estimated transformation using our approach, RC, and NMI, respectively.

where the first term represents the gamma correction on I after geometric distortion, the second term models a smoothly varying global intensity field and the third term models locally-varying intensity field with a mixture of K Gaussian densities. In this experiment, we chose a distortion level 2 with parameters as follows: $\upsilon = 0.4, K = 1, \Psi_K$ were randomly selected from the interval $[1, \nu]$ (ν is the size of the image domain), $\sigma = 30$, and γ is selected randomly from $[0.9, 1.2]$. The registered images shown in Figure 3.5 demonstrate that the proposed algorithm outperforms the RC approach, in the presence of spatially-varying intensity distortion. The result obtained by the NMI approach shows a poor performance. Moreover, the estimated deformation field obtained by our approach shows superior accuracy in comparison to RC and NMI methods.

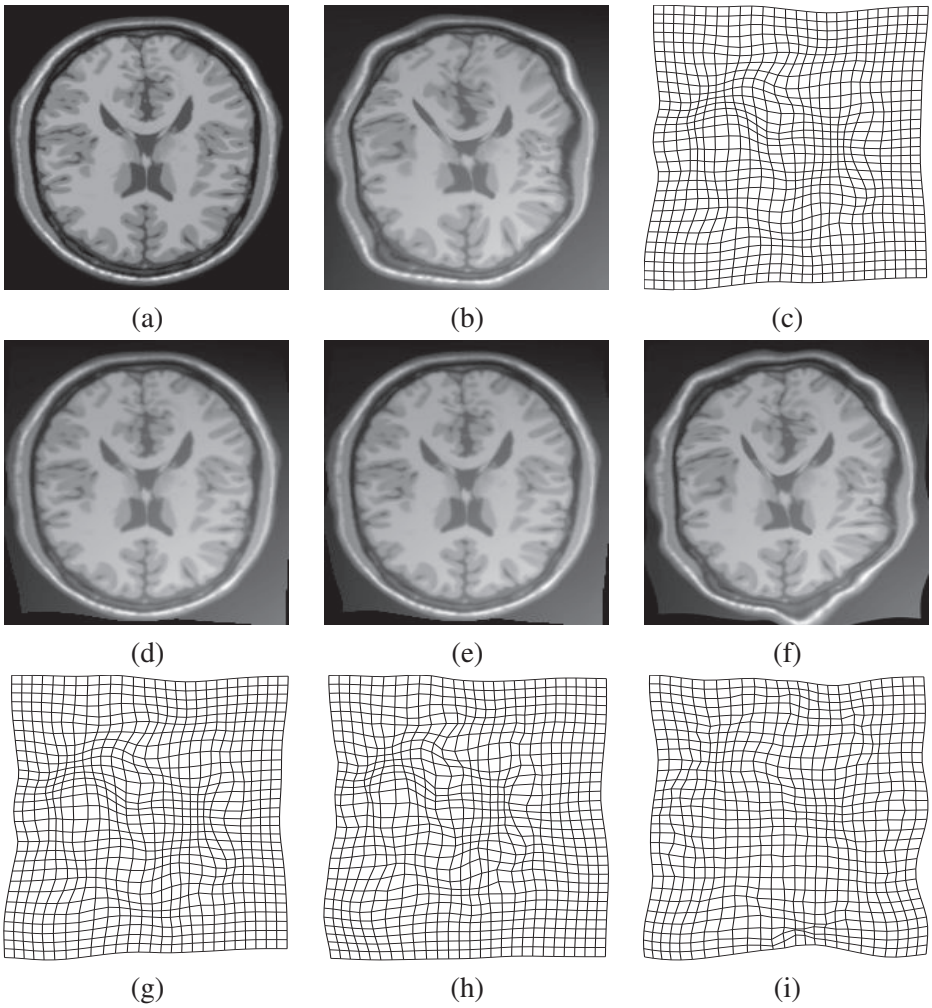

FIGURE 3.5: Geometric and intensity distortion experiment: (a) MR-T1 image; (b) distorted MR-T1 image with geometric and intensity distortion; (c) ground truth deformation field; (d)-(f) registered images using our approach, RC, and NMI, respectively; (g)-(i) the estimated transformation using our approach, RC, and NMI, respectively.

3.3.3 MULTIMODALITY TEST

The images used in this experiment are corresponding slices from MR-T1 and MR-T2 image pair, and they are originally aligned with each other. In this experiment we registered the geometrically deformed MR-T1 image onto MR-T2 image using our approach and the NMI method. We omitted the result of the RC approach because it is not applicable to multimodal images. Figure 3.6 shows the accuracy of our method in registering images from different modalities. As can be seen, the registered image using the NMI approach still has a considerable amount of misregistration. However, most of the visible amount of misalignment in the moving image has been removed after applying the proposed approach. In addition, the nonrigid

transformation estimated by the proposed method looks very similar to the ground truth, indicating a much better performance of our approach.

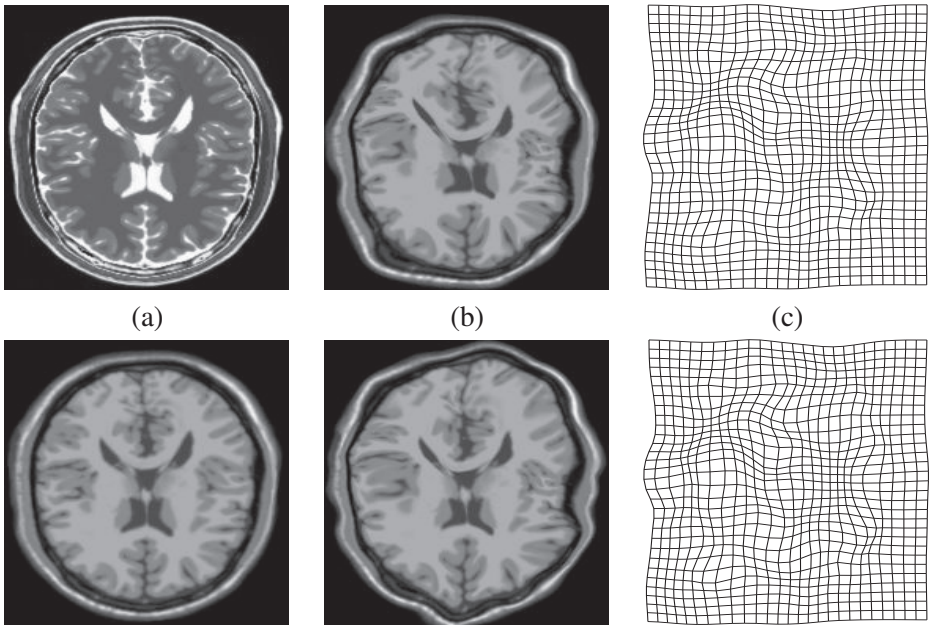

FIGURE 3.6: Multimodality experiment: (a) MR-T2 image,; (b) distorted MR-T1 image with geometric distortion; (c) ground truth deformation field; (d) and (e) registered images using our approach, and NMI, respectively; (f) the estimated transformation using our approach.

3.3.4 STATISTICAL SIGNIFICANCE TEST

We used a paired t-test to determine if the difference in mean squared error for the pairs of registration methods is statistically significant. Table 3.2 shows the p-values of the differences of mean square error between each pair of registration methods after applying paired t-test. At 95% level of confidence, it is evident from Table 3.2 that the mean squared error resulting from our approach is significantly lower than the mean squared errors resulting from RC and NMI methods, indicating the better performance of the proposed approach.

3.3.5 REAL-LIFE DATA SET: 3D THORACIC CT IMAGES

We also validated the proposed method, RC and NMI approaches on real-life clinically acquired 4D CT image data sets [58]. These publicly available data sets consist of thoracic 4D CT images acquired as part of the standard planning process for the treatment of esophageal cancer at the University of Texas

TABLE 3.2: Comparison between the registration methods using statistical significant test (p-values).

Registration Methods	μ_g				
	2.1	3.0	4.6	5.1	5.7
our method vs. RC	0.0493	0.0537	0.0067	0.0013	0.000585
our method vs. NMI	2.5033×10^{-10}	7.544×10^{-12}	3.2419×10^{-14}	0	0
RC vs. NMI	5.1467×10^{-10}	5.3916×10^{-11}	1.6183×10^{-12}	0	0

M. D. Anderson Cancer Center in Houston. Each 4D CT scan consists of a time-varying stack of ten 3D images of the entire thorax and upper abdomen, and were acquired at 2.5-mm slice spacing with a General Electric Discovery ST PET/CT scanner (GE Medical Systems, Waukesha, WI). The utmost inhale and exhale phases of the 4D CT sets were used for nonrigid registration evaluation. For each patient data set, an expert in thoracic imaging manually delineated and registered pulmonary land mark features such as vessel bifurcations between the fixed and moving image pairs as shown in Figure 3.7. A total number of four cases are used in this evaluation with a minimum of 1166 registered landmarks features in each case as shown in Table 3.3.

The deformable registration accuracy was evaluated by calculating the point registration errors as a 3D Euclidean distance between the manually determined landmark position in the exhale image and that calculated by applying the registration methods to the corresponding feature location in the inhale image. The mean registration errors and corresponding standard deviations were calculated for all cases before registration, to represent the initial misregistration, and after applying our algorithm, RC and NMI methods. As shown in Figure 3.8, it is evident that the proposed method achieved lower 3D registration errors than RC and NMI approaches. For the four patient cases, mean(standard deviation) 3D errors ranged from 1.17(1.05) to 2.30(1.65) mm for the proposed method, 1.27(1.36) to 2.48(1.89) for the RC method, and 1.92(1.52) to 4.97(3.87) for the NMI approach. For the cumulative validation landmark set of 5494 landmark pairs, the mean(standard deviation) registration errors were 1.49(1.26), 1.64(1.43) and 2.88(2.20) for the proposed method, RC and NMI approaches respectively.

TABLE 3.3: CT-image and reference landmark properties. The image volumes dimensions in units of voxels and also the voxel dimensions are shown for each patient case used in this experiment. The distribution of manually registered landmark pairs regarding right, left and total lung feature points are shown as well. More details about generation and characterization of landmarks can be found in [59].

CT properties	Case 1	Case 2	Case 3	Case 4
Volume dimensions	$256 \times 256 \times 94$	$256 \times 256 \times 112$	$256 \times 256 \times 104$	$256 \times 256 \times 99$
Voxel dimensions (mm)	$0.97 \times 0.97 \times 2.5$	$1.16 \times 1.16 \times 2.5$	$1.15 \times 1.15 \times 2.5$	$1.13 \times 1.13 \times 2.5$
Landmark points distribution	-			
# Right lung	672	767	637	803
# Left lung	608	720	529	758
Total	1280	1487	1166	1561

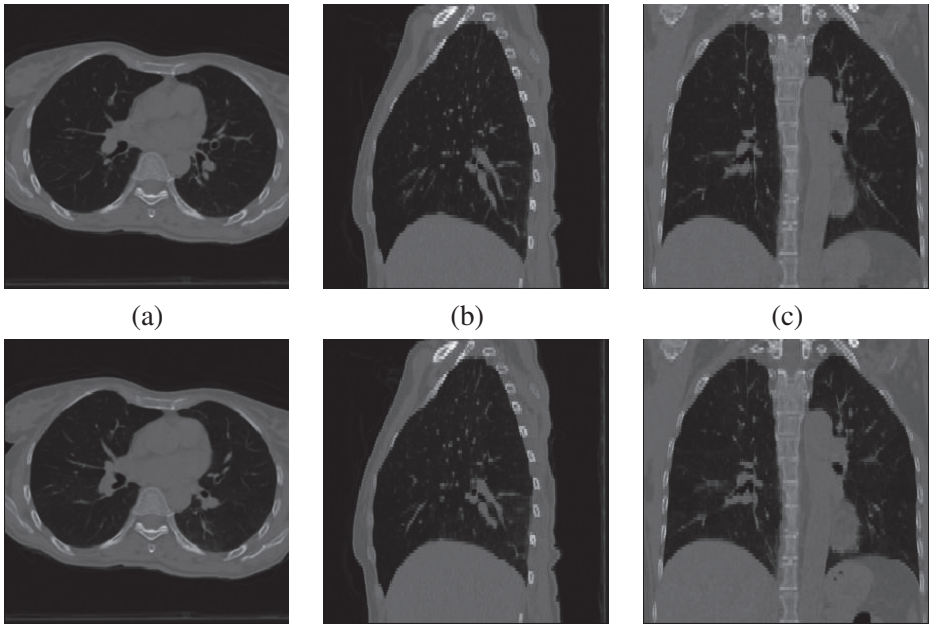

(a) (b) (c)

(d) (e) (f)

FIGURE 3.7: 4D CT scan of a lung taken during a single breath cycle: fixed (top row) and moving (bottom row) represent component phase 3D volumes from a 4D set for patient case number one. (a)-(c) display a 3D volume of the maximum inhale phase in transverse, coronal and sagittal orientation, respectively; (d)-(f) display a 3D volume of the maximum exhale phase in transverse, coronal and sagittal orientation, respectively.

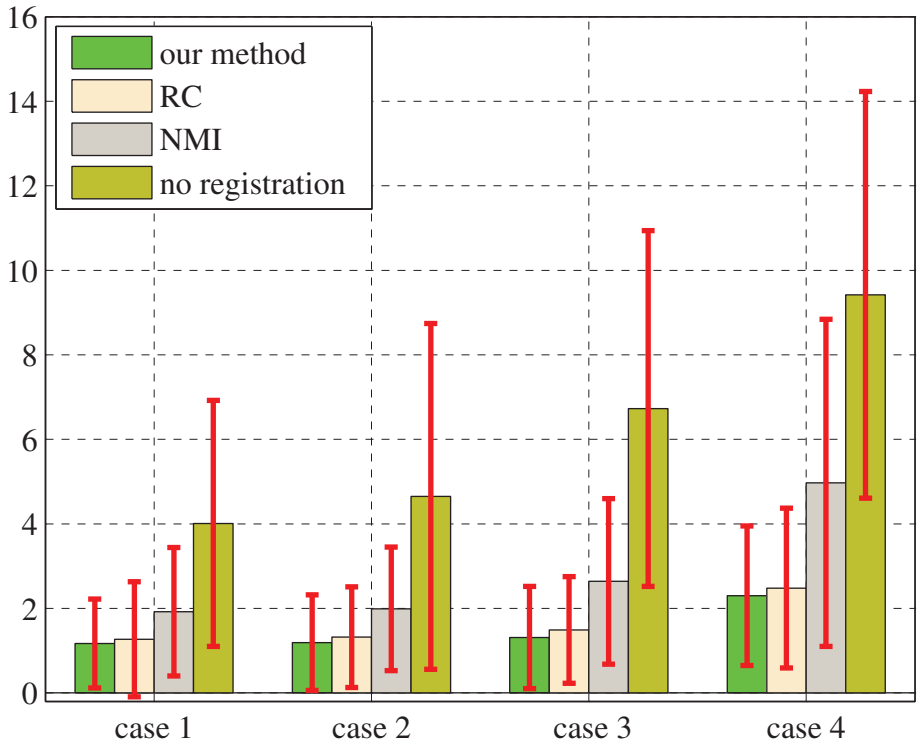

FIGURE 3.8: 3D volume registration accuracy. Mean and standard deviation of 3D registration errors are depicted for each case before registration and after applying the proposed method, RC and NMI approaches. All values are in units of millimeters.

CHAPTER 4

NONRIGID REGISTRATION OF DIFFUSION TENSOR IMAGES

In this Chapter, we propose an information-theoretic method for nonrigid registration of diffusion tensor images by extending our deformable registration algorithm described in the previous Chapter. In the proposed approach, we enable explicit orientation optimization by incorporating tensor reorientation, which is necessary for wrapping diffusion tensor images. Experimental results on diffusion-tensor image registration indicate the feasibility of the proposed approach and a much better performance compared to the affine registration method based on mutual information, not only in terms of registration accuracy in the presence of geometric distortion but also in terms of resistance to Rician noise.

4.1 INTRODUCTION

Diffusion tensor imaging (DTI) has become one of the most popular methods for analyzing the underlying white matter (WM) structure of brains and investigating the microstructure of biological tissue, especially in the presence of fibrous structures [60]. At each voxel of a diffusion tensor image, the water diffusion anisotropy and preferred orientation can be measured and represented by a symmetric second-order tensor. The orientation of the resulting diffusion tensor field represents the orientation of fiber bundles, and hence DTI is considered an ideal choice for studying and inspecting white matter metabolism in the brain.

By detecting the orientation of water molecules in white matter, DTI enables studying WM alteration across populations and provides a helpful tool for brain growth research [61]. An important prerequisite for these studies is nonrigid image registration. Extending nonrigid image registration from scalar images to DTI images is considered a challenging task, not only because of the multi-dimensionality of the DT images, but also due to the requirement of keeping DT orientation consistent with the anatomy after image transforma-

tion [62].

Recently, various techniques have been proposed in the literature to tackle the nonrigid registration problem of DT images. The vast majority of these methods can be broadly classified into three main categories: The techniques in the first category ignore the orientation components of images and register scalar images associated with DTI data set, such as the non-diffusion weighted images, MR-T2-weighted images, and fractional anisotropy maps [73, 74, 75]. In the second category, the methods register actual tensor images without reorienting the tensors during registration [65, 72]. Ruiz-Alzola *et al.* [65] proposed a unified framework for nonrigid registration of scalar, vector and tensor medical data. The framework measures image correspondence based on DT data by optimizing affine transformations in a certain restricted window of the image domain. Alexander *et al.* [72] presented a multiresolution elastic matching method and proposed a similarity measure that combines DT and T1-weighted structural information by averaging their individual similarities. In all the aforementioned techniques, no tensor reorientation was applied during the registration and hence producing inaccurate image matching results. Techniques in the last category either explicitly optimize tensor reorientation [64, 63] or perform tensor reorientation after application of the final transformations; and hence no tensor reorientation is applied during the optimization step [77]. Zhang *et al.* [64] proposed a piecewise affine registration algorithm that incorporates DT data in the similarity measure in an effort to explicitly optimize tensor reorientation. In [77], Hecke *et al.* proposed a nonrigid coregistration algorithm based on a viscous fluid model, in which the quality of image matching is measured by the mutual information similarity measure. The tensor reorientation in this method is only carried out after the application of the final deformation field.

Over the past few years, there has been a concerted research effort in statistical physics to explore the properties of Tsallis entropy, leading to a statistical mechanics that satisfies many of the properties of the standard theory [50]. Wachowiak *et al.* [51] introduced a generalized mutual information measure based on Tsallis entropy for 2D-3D multimodal biomedical image registration, and showed that their metric often produces fewer mis-registrations compared to the MI approach. In [87], we introduced a Jensen-Tsallis (JT)-based method for nonrigid image registration, as described in the previous Chapter. In the proposed approach, we modeled the nonrigid transformation of image coordinates using cubic B-splines [52]. Because of their attractive characteristics, such as inherent control of smoothness, separability in multiple dimensions and computational efficiency, B-splines are used widely in the literature to model nonrigid deformations [39, 48, 46, 47, 53]. The feasibility of the proposed algorithm was demonstrated on medical images from magnetic resonance imaging with different protocols and also on clinically acquired 4D CT

image data sets. In light of the success of our nonrigid registration method on scalar images, the focus of this Chapter is to extend our nonrigid method to DT images. More precisely, we propose a nonrigid image registration method by optimizing a multicomponent JT similarity measure using the quasi-Newton L-BFGS-B method [55] as an optimization scheme and cubic B-splines for modeling the nonrigid deformation field between the fixed and moving 3D image pairs. The analytical gradient of the JT similarity is derived so that we can achieve an efficient and accurate nonrigid registration. In order to achieve a compromise between the nonrigid registration accuracy and the associated computational cost, we implement a three-level hierarchical multi-resolution approach such that the image resolution is increased, along with the resolution of the control mesh, in a coarse to fine fashion. In the proposed approach no tensor reorientation is performed in an iterative way, assuming that JT is a robust measure of the image similarity. Tensor reorientation is only performed after the application of final deformation. The advantage of not applying tensor reorientation iteratively is to decrease the computational complexity of the registration algorithm and hence the computational time. Experimental results are provided to demonstrate the registration accuracy of the proposed approach in comparison to the affine registration method based on mutual information [76, 77].

The remainder of this Chapter is organized as follows. In the next Section, we provide a brief background on diffusion tensor imaging. In Section 4.3, we describe in detail the proposed method, including the JT similarity for multiple components, the problem statement, the tensor reorientation formulation, and then we present a summary of our proposed algorithm. Section 4.4 provides experimental results on a diffusion tensor imaging data set to demonstrate the effectiveness and superior performance of our method compared to the affine registration technique.

4.2 Background

In this section, we elaborately review the requisite background on DTI.

4.2.1 Brownian Motion

In physics, 'Brownian motion' is referred to the phenomenon that individual water molecules are constantly in motion, colliding with each other at a high speed. The phenomenon 'diffusion' can be considered as the macroscopic observable effect due to the microscopic Brownian motion of particles. Note that the diffusion of water molecules within its own environment (also known as self-diffusion) is conceptually equivalent to the diffusion of a substance in another host substance.

4.2.2 DIFFUSION

We now explain the time-distance relationship, developed by Einstein in 1905, for a particle undergoing a Brownian motion.

Isotropic environment: In isotropic environment (i.e. solutions without a concentration gradient), the probability of displacement of molecules is equal in all directions, and the mean molecular displacement is zero. As an example the grey matter in the brain is an isotropic environment in which the diffusion of water molecules is hindered equally in all directions.

The motion of the molecules in an isotropic environment can be characterized by a physical constant or the so-called diffusion coefficient D. Consider a particle in an isotropic environment (e.g., a water molecule in water) at position $\boldsymbol{r}_0$ at time $t = 0$. If its subsequent position at time $t = \tau$ is denoted by $\boldsymbol{r}$, the diffusion coefficient D can be given by Einstein's relation [66]

$$D = \frac{1}{6\tau}\langle(\boldsymbol{r} - \boldsymbol{r}_0)^2\rangle \tag{4.1}$$

where $\langle(\boldsymbol{r} - \boldsymbol{r}_0)^2\rangle$ denotes the mean square displacement over the particle ensemble.

Anisotropic environment: Unlike in isotropic environment, the motion of particles in anisotropic environment is restricted to a bounded medium, like tissues with a highly oriented microstructures in fibrous biological tissue (axonal fibers, cell membranes, polymers, etc.). For instance, the white matter in the brain consists of bundles of axon fibers that allow free diffusion along the fibers but hindered diffusion in directions perpendicular to the fibers. The displacement parallel to the direction of these boundaries appears higher than the displacement in the perpendicular direction. By virtue of this directional dependency of the displacement, Einstein's relation can be generalized as follows:

$$\boldsymbol{D} = \begin{bmatrix} D_{xx} & D_{xy} & D_{xz} \\ D_{xy} & D_{yy} & D_{yz} \\ D_{xz} & D_{yz} & D_{zz} \end{bmatrix} \tag{4.2}$$

where $\boldsymbol{D}$ is a second-order diffusion tensor. It can be shown that this 3×3 matrix is symmetric and positive definite [68, 67]. Figure 4.1 shows, from left to right, diffusion in an isotropic environment versus diffusion in an anisotropic environment. In the isotropic case the diffusion is similar in all directions while in the anisotropic case the diffusion is larger in one direction than the other.

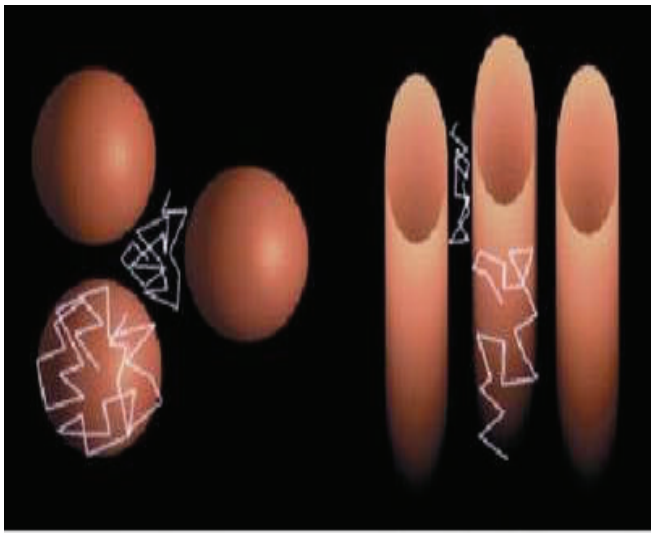

FIGURE 4.1: Isotropic diffusion (left) vs. Anisotropic diffusion (right). This image is adapted from Beaulieu [69].

4.2.3 DIFFUSION IMAGING

MRI images are sensitized to diffusion by using diffusion weighting gradient pulses which were originally introduced by Stejskal and Tanner [70]. The imaging technique which is based on the physical principles of diffusion, nuclear magnetic resonance is called Diffusion-Weighted (DW) MRI (DWI). Stejskal and Tanner [70] provided an early description of a DW sequence in 1965. They used a spin-echo T2-weighted pulse sequence with two extra gradient pulses that were equal in magnitude and opposite in direction. This sequence enabled the measurement of net water movement in one direction at a time. To measure the rate of movement along one direction, for example the x-direction, these two extra gradients are equal in magnitude but opposite in direction for all points at the same x-location. However, the strength of these two balanced gradients increases along the x-direction. Therefore, if a voxel of tissue contains water that has no net movement in the x-direction, the two balanced gradients cancel each other out. The resultant signal intensity of that voxel is equal to its signal intensity on an image obtained with the same sequence without the DW gradients. However, if water molecules have a net movement in the x-direction (eg, due to diffusion), they are subjected to the first gradient pulse at one x-location and the second pulse at a different x location. The two gradients are no longer equal in magnitude and no longer cancel. The difference in gradient pulse magnitude is proportional to the net displacement in the x-direction that occurs between the two gradient pulses, and faster-moving water protons undergo a larger net dephasing. The resultant signal intensity of a voxel of tissue containing moving protons is equal to its signal intensity on a T2-weighted image decreased

by an amount related to the rate of diffusion.

Water diffusion inside brain can be characterized by a diffusion tensor at each voxel of an MRI volume. The diffusion coefficient measured by nuclear magnetic resonance is also called apparent diffusion coefficient. This coefficient takes into account that diffusion process is not free in tissues, but hindered and modulated by many mechanisms such as restriction in closes spaces, tortuosity around obstacles, etc.

For each voxel, the signal intensity S of the tissue is calculated as follows:

$$S = S_0\, e^{-b\, ADC} \tag{4.3}$$

where S_0 is the signal intensity on the T2-weighted image, b is a factor representing the strength of diffusion sensitivity, and ADC is the apparent diffusion coefficient. The diffusion tensor, $\boldsymbol{D}$, and the apparent diffusion coefficient, ADC are related by the equation:

$$ADC = \hat{\boldsymbol{g}}_k^T \boldsymbol{D} \hat{\boldsymbol{g}}_k \tag{4.4}$$

where $\mathbf{g}_k$ is a unit vector [64].

Acquisition and computation of the diffusion tensor: Several DW images and different non-collinear gradient directions $\boldsymbol{g}_k (k = 1, 2, \ldots, N)$ should be acquired to compute the diffusion tensor $\boldsymbol{D}(\boldsymbol{r})$. Because $\boldsymbol{D}(\boldsymbol{r})$ is characterized by six degrees of freedom, at least six DW measurements $S_k(\boldsymbol{r})$ are needed, along with a reference image $S_0(\boldsymbol{r})$ acquired without diffusion weighting. In general, $\boldsymbol{D}(\boldsymbol{r})$ can be calculated for each voxel at position $\boldsymbol{r}$ by solving the following system of equations

$$S_k(\boldsymbol{r}) = S_0(\boldsymbol{r}) e^{-b\, \hat{\boldsymbol{g}}_k^T \boldsymbol{D}(\boldsymbol{r}) \hat{\boldsymbol{g}}_k} \;\text{ with }\; \hat{\boldsymbol{g}}_k = \frac{\boldsymbol{g}_k}{\|\boldsymbol{g}_k\|} \tag{4.5}$$

The matrix form of the linear equation system described in Eq. (4.5) can also be represented as follows:

$$\underbrace{\begin{bmatrix} \frac{1}{b}\ln\left(\frac{S_0(r)}{S_1(r)}\right) \\ \frac{1}{b}\ln\left(\frac{S_0(r)}{S_2(r)}\right) \\ \vdots \\ \frac{1}{b}\ln\left(\frac{S_0(r)}{S_N(r)}\right) \end{bmatrix}}_{\boldsymbol{B}(\boldsymbol{r})} = \underbrace{\begin{bmatrix} (\hat{\boldsymbol{g}}_{1x})^2 & 2\hat{\boldsymbol{g}}_{1x}\hat{\boldsymbol{g}}_{1y} & 2\hat{\boldsymbol{g}}_{1x}\hat{\boldsymbol{g}}_{1z} & (\hat{\boldsymbol{g}}_{1y})^2 & 2\hat{\boldsymbol{g}}_{1y}\hat{\boldsymbol{g}}_{1z} & (\hat{\boldsymbol{g}}_{1z})^2 \\ (\hat{\boldsymbol{g}}_{2x})^2 & 2\hat{\boldsymbol{g}}_{2x}\hat{\boldsymbol{g}}_{2y} & 2\hat{\boldsymbol{g}}_{2x}\hat{\boldsymbol{g}}_{2z} & (\hat{\boldsymbol{g}}_{2y})^2 & 2\hat{\boldsymbol{g}}_{2y}\hat{\boldsymbol{g}}_{2z} & (\hat{\boldsymbol{g}}_{2z})^2 \\ \vdots & \vdots & \vdots & \vdots & \vdots & \vdots \\ (\hat{\boldsymbol{g}}_{Nx})^2 & 2\hat{\boldsymbol{g}}_{Nx}\hat{\boldsymbol{g}}_{Ny} & 2\hat{\boldsymbol{g}}_{Nx}\hat{\boldsymbol{g}}_{Nz} & (\hat{\boldsymbol{g}}_{Ny})^2 & 2\hat{\boldsymbol{g}}_{Ny}\hat{\boldsymbol{g}}_{Nz} & (\hat{\boldsymbol{g}}_{Nz})^2 \end{bmatrix}}_{\boldsymbol{G}} \underbrace{\begin{bmatrix} D_{xx}(r) \\ D_{xy}(r) \\ D_{xz}(r) \\ D_{yy}(r) \\ D_{yz}(r) \\ D_{zz}(r) \end{bmatrix}}_{\boldsymbol{D}(\boldsymbol{r})} \tag{4.6}$$

When DW measurements $(N = 6)$ are exactly six, the unique diffusion tensor components can easily be calculated as follows:

$$\boldsymbol{D}(\boldsymbol{r}) = \boldsymbol{G}^{-1} \boldsymbol{B}(\boldsymbol{r}). \tag{4.7}$$

For more than six DW images, an over-determined system of equations is obtained which can be solved by Least Square (LS) methods [82]. For example, when applying the linear non-weighted LS approach, the diffusion tensor components can be calculated as follows:

$$\boldsymbol{D}(\boldsymbol{r}) = (\boldsymbol{G}^T\boldsymbol{G})^{-1}\boldsymbol{G}^T\boldsymbol{B}(\boldsymbol{r}). \tag{4.8}$$

The over-constrained solution for $\boldsymbol{D}(\boldsymbol{r})$ has the advantages of reducing the amount of noise propagating from the DW measurements into the calculated diffusion tensor, and increasing the robustness of anisotropy and tensor-orientation estimations. On the other hand, acquiring more DW measurements has the drawback of dramatically increasing the acquisition and processing time.

Six axial DW measurements $S_k(\boldsymbol{r})$ and one non-DW image $S_0(\boldsymbol{r})$ are shown in Figure 4.2, along with the corresponding magnetic field gradients $\boldsymbol{g}_k\,(k = 1, \ldots, 6)$. Note the difference in intensity values for different gradient directions $\boldsymbol{g}_k$.

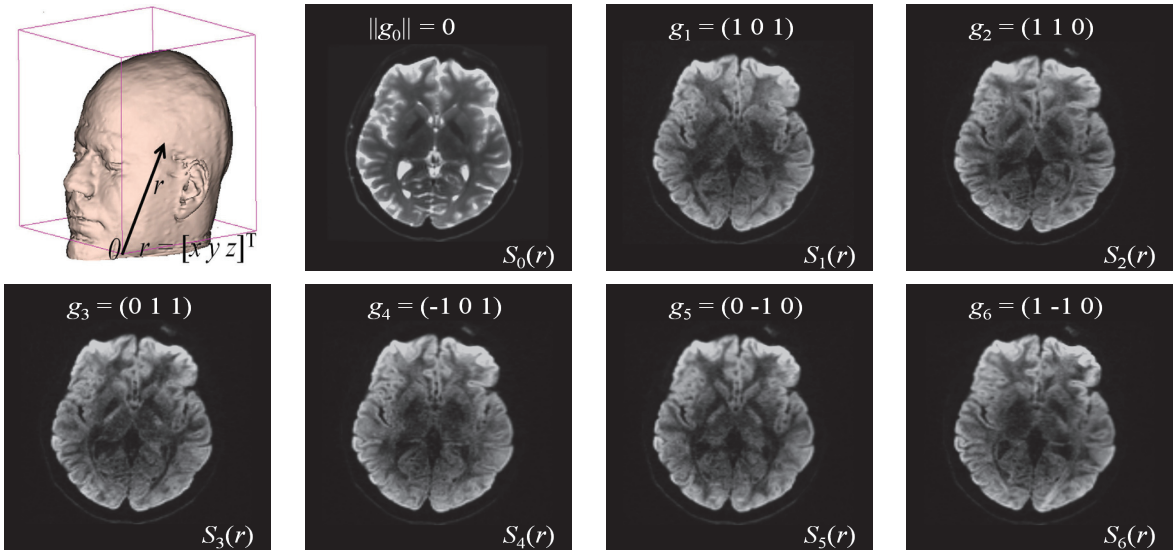

FIGURE 4.2: Axial DW images $S_k(\boldsymbol{r})$ of the human brain for different gradient directions $\boldsymbol{g}_k$.

In fact, the diffusion tensor field $\boldsymbol{D}$ is a covariance matrix describing the translational displacement of the diffusing molecules. Therefore, an ellipsoidal shape can be associated with $\boldsymbol{D}$, which represents the probabilistic iso-surface of this molecular diffusion [83]. Because $\boldsymbol{D}$ is a symmetric and positive definite second-order tensor, an eigendecomposition of $\boldsymbol{D}$ yields

$$\boldsymbol{D} = \boldsymbol{E}\boldsymbol{\Lambda}\boldsymbol{E}^{-1}, \tag{4.9}$$

where

$$\boldsymbol{E} = [\boldsymbol{e}_1\ \boldsymbol{e}_2\ \boldsymbol{e}_3] \qquad \text{and} \qquad \boldsymbol{\Lambda} = \begin{bmatrix} \lambda_1 & 0 & 0 \\ 0 & \lambda_2 & 0 \\ 0 & 0 & \lambda_3 \end{bmatrix}$$

and $\lambda_1 \geq \lambda_2 \geq \lambda_3 > 0$ are the positive eigenvalues of $\boldsymbol{D}$ associated to the orthonormal eigenvectors $\boldsymbol{e}_i$. The spectral decomposition of the diffusion tensor may be written as

$$\boldsymbol{D} = \lambda_1 \boldsymbol{e}_1 \boldsymbol{e}_1^T + \lambda_2 \boldsymbol{e}_2 \boldsymbol{e}_2^T + \lambda_3 \boldsymbol{e}_3 \boldsymbol{e}_3^T \tag{4.10}$$

The eigenvectors and eigenvalues of $\boldsymbol{D}$ represent the principal axes of the ellipsoid and their corresponding principal diffusion coefficients, respectively, as illustrated in Figure 4.3. Therefore, the ellipsoid axes are oriented according to the tensor eigenvectors, and their lengths depend on the tensor eigenvalues.

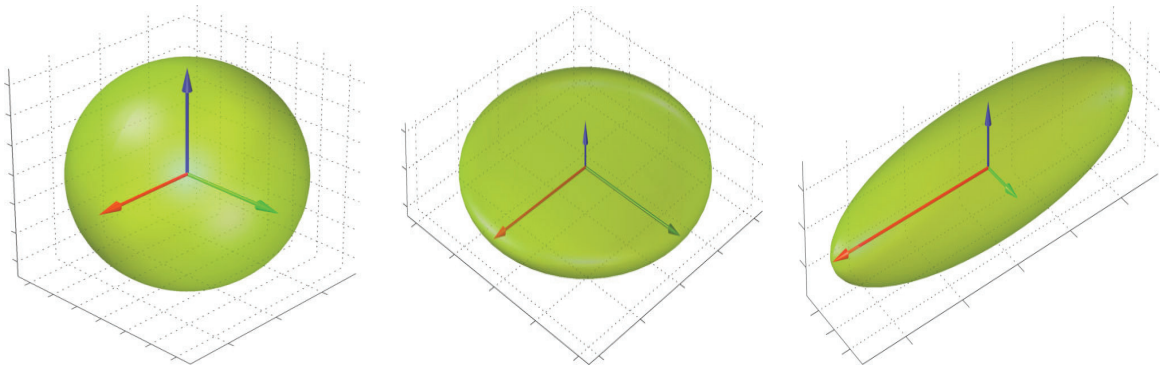

$\lambda_1 \approx \lambda_2 \approx \lambda_3$ $\lambda_1 \approx \lambda_2 \gg \lambda_3$ $\lambda_1 \gg \lambda_2 \approx \lambda_3$

FIGURE 4.3: Different cases of diffusion: Spherical diffusion (left); planar diffusion (center); linear diffusion (right).

4.2.4 SCALAR INDICES

The first eigenvector $\boldsymbol{e}_1$ (i.e., corresponding to λ_1) of a symmetric tensor $\boldsymbol{D}$ describes the predominant diffusion direction, which is parallel to the orientation of the corresponding underlying white matter fiber system. Therefore, it is also called the Principal Diffusion Vector. Figure 4.4 shows a visualization of the color-coded MR-DTI data with ellipsoids. The predominant diffusion direction can be directly related to a Green (G), Red (R), and Blue (B) digital color triple. The convention in which the G, R, and B color components represent the directions is as follows:

$$[||e_{1x}||, ||e_{1y}||, ||e_{1z}||] = [G, R, B]\,. \tag{4.11}$$

The RGB color-coded directionality maps provide an indication of the direction in which water diffusion is highest and improve the visibility of different WM fiber bundles. Many other useful scalar measures can be derived from the diffusion tensor $\boldsymbol{D}$, which provide supplementary information on the tissue microstructure.

Trace and Mean Diffusivity: The total diffusivity is $\text{trace}(D) = \sum_{i=1}^{3} \lambda_i$, and the mean diffusivity (MD) is equal to one third of $\text{trace}(D)$. The MD measure serves as an indicator of brain maturation and/or injury and provides the overall magnitude of water diffusion independent of anisotropy [84]. The MD map is shown in Figure 4.7(c) for which higher values of average diffusion appear brighter.

Fractional Anisotropy (FA): FA serves as an indicator of the degree of water diffusion anisotropy independent of the overall water diffusion coefficient and is defined as

$$FA = \sqrt{\frac{3}{2} \frac{\sum_{i=1}^{3} (\lambda_i - \frac{1}{3}\text{trace}(D))^2}{\sum_{i=1}^{3} \lambda_i^2}} \tag{4.12}$$

which is basically the normalized standard deviation of the eigenvalues. The values of FA vary from 0 to 1 with higher values corresponding to greater diffusion anisotropy. Figure 4.7(c) shows the FA map of the same slice as in Figure 4.7(a). The higher values of FA correspond to the white matter regions which contain densely packed fiber bundles that cause anisotropic diffusion by restricting water movement along the direction perpendicular to the fiber bundles.

4.3 Proposed Method

In this section, we present the details of our proposed nonrigid approach for DTI registration.

4.3.1 Literature Pertinent to DTI Registration

Different methods to register DTI data sets have been proposed in the literature. Some of these methods are based on aligning T1- or T2- weighted images that are taken at the same time as DTI data sets, followed by applying the resulting deformation to DT images. T1- and T2-weighted images represent the white matter structure as low-contrast regions, and hence registration based on these images poorly align the structure and orientation of the white matter regions [78]. To overcome this problem and provide a more structural information, diffusion tensor features are used. One possible feature that contains a high white matter contrast is the scalar FA map, which has proven to be a suitable feature [73]. Guimond *et al.* [74] proposed a multicomponent registration method based on eigenvalue images. Another feature that enhanced the quality of diffusion tensor image registration is the DT components as reported in [78, 79]. Thirion *et al.* [79] proposed a demons-based registration algorithm and used the sum of square differences as a similarity

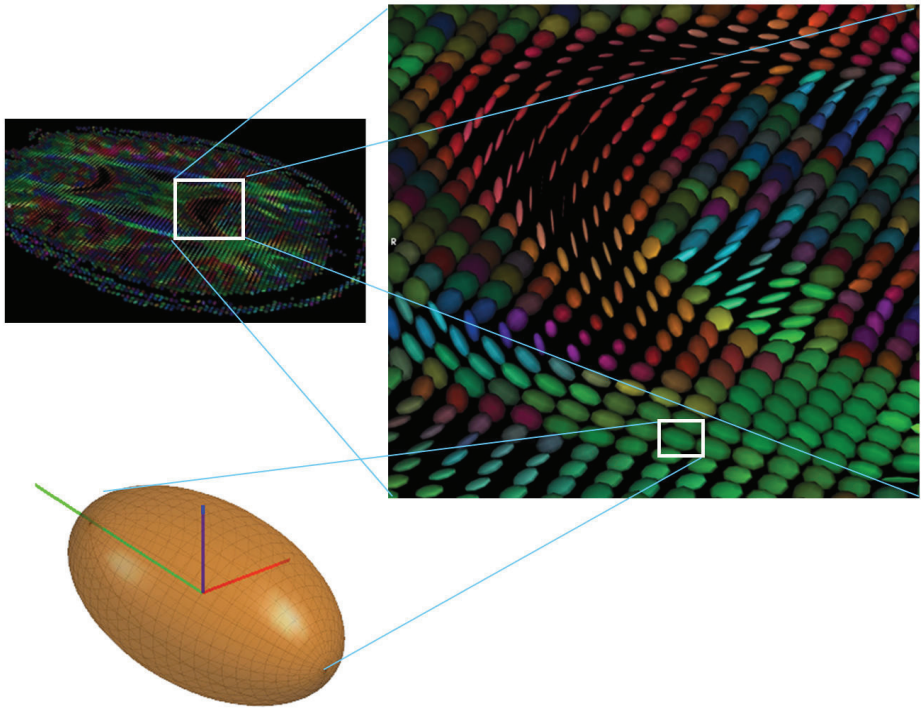

FIGURE 4.4: Ellipsoidal representation of the diffusion tensor at each voxel location of a DTI image.

criterion based on DT elements. Alexander *et al.* [62] reported that only rigid transformation should reorient the tensors to keep them consistent with anatomical structure of the image. For scalar measures, including the eigenvalues and FA map, tensor reorientation is not required during registration since they are invariant to rigid transformations of their corresponding tensors. In contrast to FA, the DT elements contain orientation information, and hence the voxel intensities of the DT elements may have different values for a particular white matter tract follows a different path in two subjects, where the FA can be similar. Because the intensity variation in corresponding voxels has a local, spatial dependent nature, a DTI image registration algorithm needs to accommodate both the alignment of intersubject images and the presence of nonlinear intervoxel intensity differences [77]. Moreover, the widely used sum of square differences similarity measure assumes similar voxel intensity values in different images that only differ from each other by a Gaussian noise term. But the FA or eigenvalue image data are known to be non-Gaussian distributed due to nonlinearity in the calculation of the eigenvalue system [81]. As a result, the sum of square differences cannot be used for this purpose optimally.

To tackle the aforementioned problem, we propose to use a multicomponent entropic similarity measure

for DT image registration. By employing the Jensen-Tsallis similarity, the nonlinear intervoxel intensity differences are taken into account without the need for an explicit tensor reorientation during the optimization procedure. Hence, the tensors are only reoriented after the application of the final deformation field. In this Chapter, two different registration approaches are evaluated using a different number of components: the FA map with one component, and the DT elements with six components.

4.3.2 Jensen-Tsallis Similarity for Multiple Components

As we have seen in the previous Chapter, the JT similarity measure is defined between two scalar images. In this Chapter, we propose an extension of the JT similarity to register DTI data sets. In our first approach, referred to as JT-FA, we apply the JT registration algorithm to the FA map between the fixed and deformed moving images. In this approach we do not need to modify the JT similarity measure since each DTI data set contains only one FA map $L = 1$. In the second approach, called JT-DT, the JT similarity measure needs to be modified to register the multicomponent DT elements since each DTI data set contains six DT elements $L = 6$. For the calculation of multi-component JT, the bivariate JT is computed for all corresponding components separately, assuming them to be independent. For instance, the first DT element image $\ell = 1$ of the fixed DTI data set is compared to the first DT element image of the moving DTI data set. A similar approach was presented in [77] using mutual information as similarity metric. The multicomponent JT similarity measure is then calculated by averaging the bivariate JT of the different corresponding components. Finally, the JT-DT approach is optimized in the iterative registration process.

The calculation of the JT similarity for multiple components and its derivative can be summarized as follows: First, we calculate the bivariate JT $S^{\boldsymbol{\omega}}_{\ell,2}$, $\ell = 1, \ldots, L$ and its derivative between all corresponding components of the moving and fixed DTI data sets using Eq. (4.13) and then we find their average as in Eq. (4.14).

$$\begin{cases} S^{\boldsymbol{\omega}}_{\ell,2}(\boldsymbol{p}_{\ell,1}, \ldots, \boldsymbol{p}_{\ell,n}) = 1 - \dfrac{D^{\boldsymbol{\omega}}_{\ell,2}(\boldsymbol{p}_{\ell,1}, \ldots, \boldsymbol{p}_{\ell,n})}{\log_2 n} \\ \dfrac{\partial S^{\boldsymbol{\omega}}_{\ell,2}(\boldsymbol{p}_{\ell,1}, \ldots, \boldsymbol{p}_{\ell,n})}{\partial \boldsymbol{\mu_\ell}} = -\dfrac{\partial D^{\boldsymbol{\omega}}_{\ell,2}(\boldsymbol{p}_{\ell,1}, \ldots, \boldsymbol{p}_{\ell,n})}{\partial \boldsymbol{\mu_l}} \times \dfrac{1}{\log_2 n} \end{cases} \tag{4.13}$$

where $\boldsymbol{p}_{\ell,i}\,(i = 1, \ldots, n)$ are based on the conditional intensity probability distributions of corresponding

image component ℓ.

$$\begin{cases} S_2^{\boldsymbol{\omega}}(\boldsymbol{p}_1, \ldots, \boldsymbol{p}_n) = \dfrac{1}{L} \displaystyle\sum_{\ell=1}^{L} S_{\ell,2}^{\boldsymbol{\omega}}(\boldsymbol{p}_{\ell,1}, \ldots, \boldsymbol{p}_{\ell,n}) \\ \dfrac{\partial S_2^{\boldsymbol{\omega}}(\boldsymbol{p}_1, \ldots, \boldsymbol{p}_n)}{\partial \boldsymbol{\mu}} = \dfrac{1}{L} \displaystyle\sum_{\ell=1}^{L} \dfrac{\partial S_{\ell,2}^{\boldsymbol{\omega}}(\boldsymbol{p}_{\ell,1}, \ldots, \boldsymbol{p}_{\ell,n})}{\partial \boldsymbol{\mu}_{\boldsymbol{\ell}}} \end{cases} \tag{4.14}$$

Note that when $L = 1$, the JT similarity for multiple components reduces to the bivariate JT derived in Chapter 3.

4.3.3 Problem Statement

In the sequel, we will use the multicomponent JT similarity measure, given by Eq. (4.14), as a matching criterion to solve the nonrigid DT image alignment problem. Let I and J be two misaligned images to be registered, where I is the fixed image and J is the moving image. The moving image J is obtained by applying a deformation field Φ to the fixed image I, as depicted in Figure 4.5. Note that, the deformation field Φ can be applied directly to the DT components of the the fixed image I or we can apply it to the DWI images before calculating the DT components. The deformation field $\boldsymbol{\Phi}$ is described by a transformation function $g(\boldsymbol{x}; \boldsymbol{\mu}) : V_J \rightarrow V_I$, where V_J and V_I are continuous domains on which J and I are defined, and $\boldsymbol{\mu}$ is a set of transformation parameters to be determined. The image alignment or registration problem may be formulated as an optimization problem:

$$\hat{\boldsymbol{\mu}} = \arg\min_{\boldsymbol{\mu}} S_\alpha^{\boldsymbol{\omega}}\big(I(\boldsymbol{x}), J(g(\boldsymbol{x}; \boldsymbol{\mu}))\big). \tag{4.15}$$

To align the transformed moving image $J(g(\boldsymbol{x}; \boldsymbol{\mu}))$ to the fixed image I, we seek the set of transformation parameters $\boldsymbol{\mu}$ that minimize the JT cost function $S_\alpha^{\boldsymbol{\omega}}\big(I(\boldsymbol{x}), J(g(\boldsymbol{x}; \boldsymbol{\mu}))\big)$. If I and J are scalar-valued images, then image transformations only change the position of each voxel $\boldsymbol{x}$. Image deformation is more complex for diffusion tensor images because the transformations also change the diffusion tensor orientation. Hence, tensor reorientation is needed to ensure that DT orientation is consistent with the underlying deformed microstructure.

4.3.4 Tensor Reorientation Formulation

For rigid transformation of DT images, tensor reorientation is straightforward. Let the orthogonal matrix $\boldsymbol{R}$ denote the rotational component of the rigid transformation to each tensor. Thus, the reorientation on a diffusion tensor $\boldsymbol{D}$ is $\boldsymbol{D}' = \boldsymbol{R}\boldsymbol{D}\boldsymbol{R}^T$.

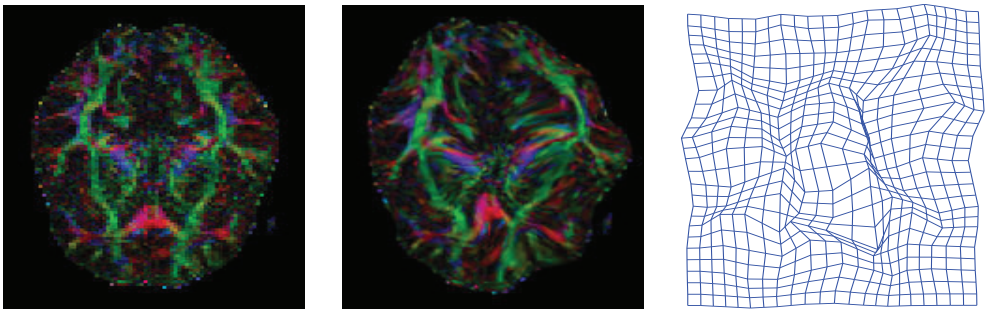

(a) (b) (c)

FIGURE 4.5: (a) Fixed image I; (b) moving image J; (c) deformation field $\mathbf{\Phi}$.

Under nonrigid transformations of DT images, when the moving image J is deformed to match the fixed image I with the mapping $g : V_J \rightarrow V_I$ then the tensor at voxel location $\boldsymbol{x}$ is deformed according to the Jacobian matrix $\boldsymbol{M} = \nabla g^{-1}(\boldsymbol{x})$. Alexander *et al.* [62] proposed a simple reorientation strategy, called finite strain method, to determine a rotational matrix $\boldsymbol{R}$ from the Jacobian matrix M. The finite strain algorithm selects the best orthogonal approximation of $\boldsymbol{M}$ to be $\boldsymbol{R}$, where $\boldsymbol{R}$ is the solution of $\arg\min_{\boldsymbol{R}'} ||\boldsymbol{R}' - \boldsymbol{M}||$ which is equal to $\boldsymbol{M}/\sqrt{\boldsymbol{M}\boldsymbol{M}^T}$. Figure 4.6 shows a registered image before and after applying FS tensor reorientation algorithm. In Figure 4.6(b), we display a portion of the diffusion tensor field before applying the tensor reorientation algorithm. Some tensor orientations in this field are not consistent with the anatomy after image deformation. Figure 4.6(d) shows that the orientations of all tensors become consistent with the anatomy after applying the finite strain method.

4.3.5 SUMMARY OF THE PROPOSED METHODOLOGY

Similar to the nonrigid registration technique introduced in Chapter 3, the proposed algorithm for nonrigid DTI-image registration is implemented by changing the deformation in the moving image(s) until the discrepancy between the moving and fixed images is minimized. The main algorithmic steps of our DTI-based nonrigid image registration approach are summarized in Algorithm 2. First, the algorithm initializes the deformation field $\mathbf{\Phi}$ by creating a uniform B-spline control grid with predefined spacing knots. Next, a 3-level hierarchical multi-resolution scheme is used to achieve the best compromise between the registration accuracy and the associated computational cost. As the hierarchical level increases the resolution of the control mesh is increased, along with the image resolution, in a coarse to fine fashion. In each hierarchical level, a limited-memory, quasi-Newton minimization scheme is used to find the optimum set of transformation parameters that reduce the JT cost function until the difference between the cost function values in two

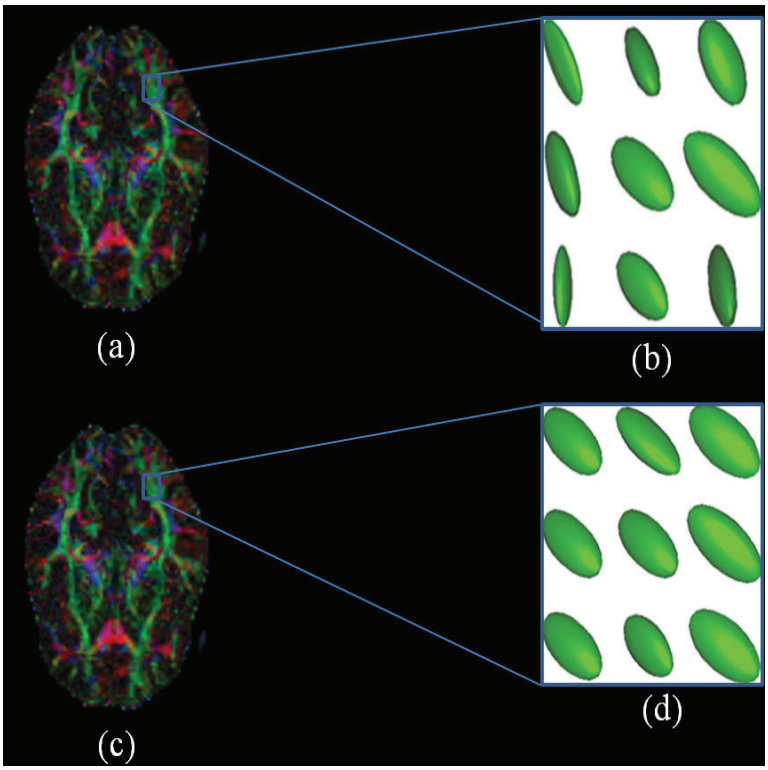

FIGURE 4.6: (a) and (c) Registered images before and after tensor reorientation, respectively; (b) and (d) Diffusion tensors of a certain region before and after applying tensor reorientation, respectively.

consecutive iterations is less than $\varepsilon = 0.01$. The resolution of the optimum set of transformation parameters, at a courser level, is increased to be used as starting point for the next hierarchical level. Finally, after the application of the final deformation field a tensor reorientation is applied using the finite strain strategy.

Algorithm 2 Proposed nonrigid DTI registration approach

1: Initialize the deformation field $\mathbf{\Phi}$ for each DTI-image component
2: **for** $hierarchical\_level = 1$ to 3 **do**
3: Calculate the cost function and its gradient as given by Eq. (4.14)
4: **repeat**
5: Use the quasi-Newton method to solve the optimization problem given by Eq. (4.15)
6: Update the deformation field for each DTI-image component
7: Recalculate the cost function and its gradient
8: **until** the difference in consecutive iterates is less than $\varepsilon = 0.01$
9: Increase the resolution of both the deformation field and the image.
10: **end for**
11: Apply tensor reorientation using the finite strain strategy.

4.4 Experimental Results

We tested the performance of the proposed approach on medical imaging data sets that were obtained from the National Alliance for Medical Image Computing (NAMIC) database in the MIDAS Journal [80]. These data sets contain 20 cases: ten are normal controls and ten are Schizophrenic. Each data set contains images from several protocols, including T1-weighted (MR-T1), T2-weighted (MR-T2), diffusion weighted DWI, and fMRI. The images used in our experiments are DTI scans that were acquired on a 3 Tesla GE system using an echo planar imaging (EPI) DTI Tensor sequence. The following scan parameters were used: TR=17000 ms, TE=78 ms, FOV=24 cm, 144×144 encoding steps, and 1.7 mm slice thickness. The number of slices is 85 axial slices. In addition, B_o field inhomogeneity maps are collected. To validate the registration accuracy of the proposed method on DTI data, we first applied geometric distortion to a fixed image in order to generate a moving image. Then, we aligned the moving image with the fixed image. In all the experiments, we used an entropic index $\alpha = 2$ and the normalized histogram of the fixed image as the weight vector $\boldsymbol{\omega}$ for the multicomponent JT similarity measure.

For the implementation of our JT-DT and JT-FA approaches, we modeled the nonrigid deformation field as a free-form deformation based on B-splines and then we employ an iterative gradient descent scheme as an optimization algorithm. In all the experiments, the moving image is generated by applying a random perturbation to the corresponding fixed image using a thin-plate spline interpolation such that the mean nonrigid displacement of the pixels, caused by the relative displacement between the fixed and generated moving images, is the ground truth deformation field.

4.4.1 Evaluation Criteria

For the quantitative evaluation analysis, we considered only voxels having FA values larger than 0.4. The registration accuracy of the proposed method is evaluated in terms of both the spatial registration and orientation correspondence.

Deformation field correspondence: The deformation field correspondence measure is defined as

$$C_B = \frac{\|\boldsymbol{\Phi} - \boldsymbol{\Phi}'\|}{\|\boldsymbol{\Phi}\| + \|\boldsymbol{\Phi}'\|} \tag{4.16}$$

where C_B represents the distance between the estimated deformation field $\boldsymbol{\Phi}'$ and the ground-truth deformation $\boldsymbol{\Phi}$ for each voxel B. We then compute the median value, denoted by C, of C_B of all selected voxels. The median value C represents an overall measure of the deformation field correspondence, and takes values

between 0, when the estimated deformation field exactly matches ground truth deformation, and 1 resulting in the worst alignment.

First eigenvector angle difference: To evaluate the quality of registration method with respect to the orientation information, the angle a_B between the first eigenvector $\boldsymbol{n}_B$ of the fixed image and the deformed moving image $\boldsymbol{n}'_B$ can be calculated for each selected white matter voxel B as follows:

$$a_B = \cos^{-1}\left(\frac{\langle \boldsymbol{n}'_B, \boldsymbol{n}_B \rangle}{||\boldsymbol{n}'_B||\,||\boldsymbol{n}_B||}\right) \tag{4.17}$$

The median, denoted by a, of all selected voxels B is a measurement of preservation of orientation information after registration. The smaller this value is, the better orientation alignment between the involved images.

Overlap of eigenvalue-eigenvector pairs: The overlap of eigenvalue-eigenvector pairs between tensors is another measure of registration quality given by

$$OVL = \frac{1}{N_B}\sum_{B}\frac{\sum_{i=1}^{3}\lambda'_i\lambda_i\langle\boldsymbol{\varepsilon}'_i,\boldsymbol{\varepsilon}_i\rangle^2}{\sum_{i=1}^{3}\lambda'_i\lambda_i} \tag{4.18}$$

where N_B the total number of selected WM voxels, and λ'_i, λ_i, $\boldsymbol{\varepsilon}'_i$ and $\boldsymbol{\varepsilon}_i$ are eigenvalues and eigenvectors of the deformed moving image and fixed image, respectively. The maximum value 1 of OVL indicates complete overlap, whereas the minimum value 0 represents no overlap of the principal axes of the DT field.

4.4.2 Qualitative Registration Test

In the first experiment, we distorted the fixed DWI images of the data set shown in Figure 4.7 with a known nonrigid transformation field, or the so-called ground truth deformation, $\boldsymbol{\Phi}$ as shown in Figure 4.8(a). Then, the DT field is computed from the deformed DW images. Next, the DT elements are reoriented to preserve the alignment with the underlying, deformed microstructure. And then, the DW images are recomputed from the reoriented DT field, resulting in the moving image data set as shown in Figure 4.8(b)-(c). Next, we applied the proposed approaches using DT elements (JT-DT) and FA images (JT-FA), as well as the affine registration method based on mutual information [76, 77]. And finally, we compared the registered DT and FA images to their corresponding fixed images. Figure 4.8 shows the results obtained from this experiment. Note that the registered moving images obtained by JT-DT and JT-FA are visually more similar in shape to the fixed images than the images produced by the affine method. Moreover, it can be seen that the registered image using the affine registration method still has a considerable amount of misregistration. However, most of the visible amount of misalignment in the moving image has been removed after applying our JT-DT and JT-FA approaches.

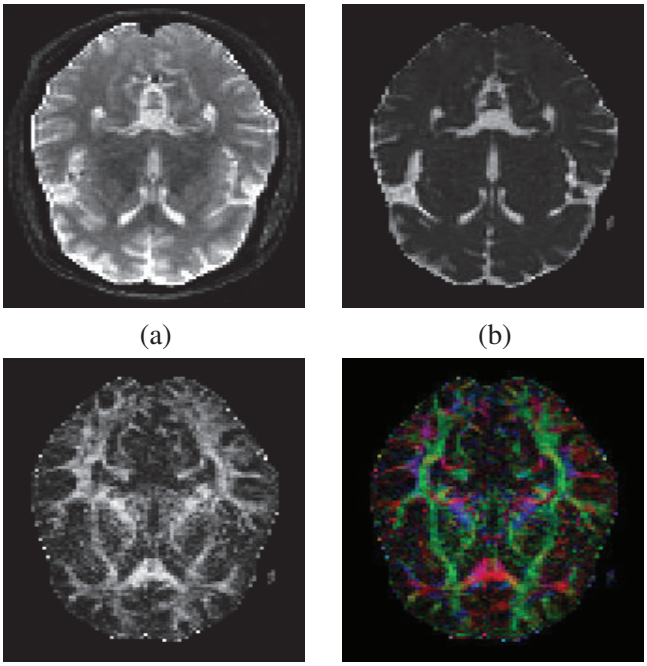

FIGURE 4.7: The axial slice No. 30 of the diffusion tensor image chosen as the template in this study : (a) DW image; (b) Mean diffusion; (c) Fractional anisotropy; (d) Color-coded DT elements. The DT maps are color-coded according to the diffusion direction.

4.4.3 QUANTITATIVE TEST

Quantitative registration results on DTI data sets deformed with known deformation fields are shown in Figure 4.9. All methods apply the finite strain strategy to reorient the tensors after registration. In Figure 4.9(a)-(b), the eigenvalue-eigenvector overlap (OVL) of tensors in corresponding voxels, and the first eigenvector angle difference (a) between the first eigenvectors of corresponding voxels are displayed. As shown in these two figures, the proposed registration approaches outperform the affine registration method. Moreover, the use of diffusion elements in the JT-DT method resulted in improved registration results compared to the JT-FA method. In Figure 4.9(c), the measure C calculates the discrepancy between the estimated deformation field and ground truth deformation field. The results obtained using the JT-DT method are considerably small compared to JT-FA. On the other hand, a paired t-test is used to determine if the difference in the quantitative parameters for the pairs of registration methods is statistically significant. The table displayed in Figure 4.9(d) shows that at 95% level of confidence, the JT-DT method significantly improves the registration accuracy compared to JT-FA and affine methods.

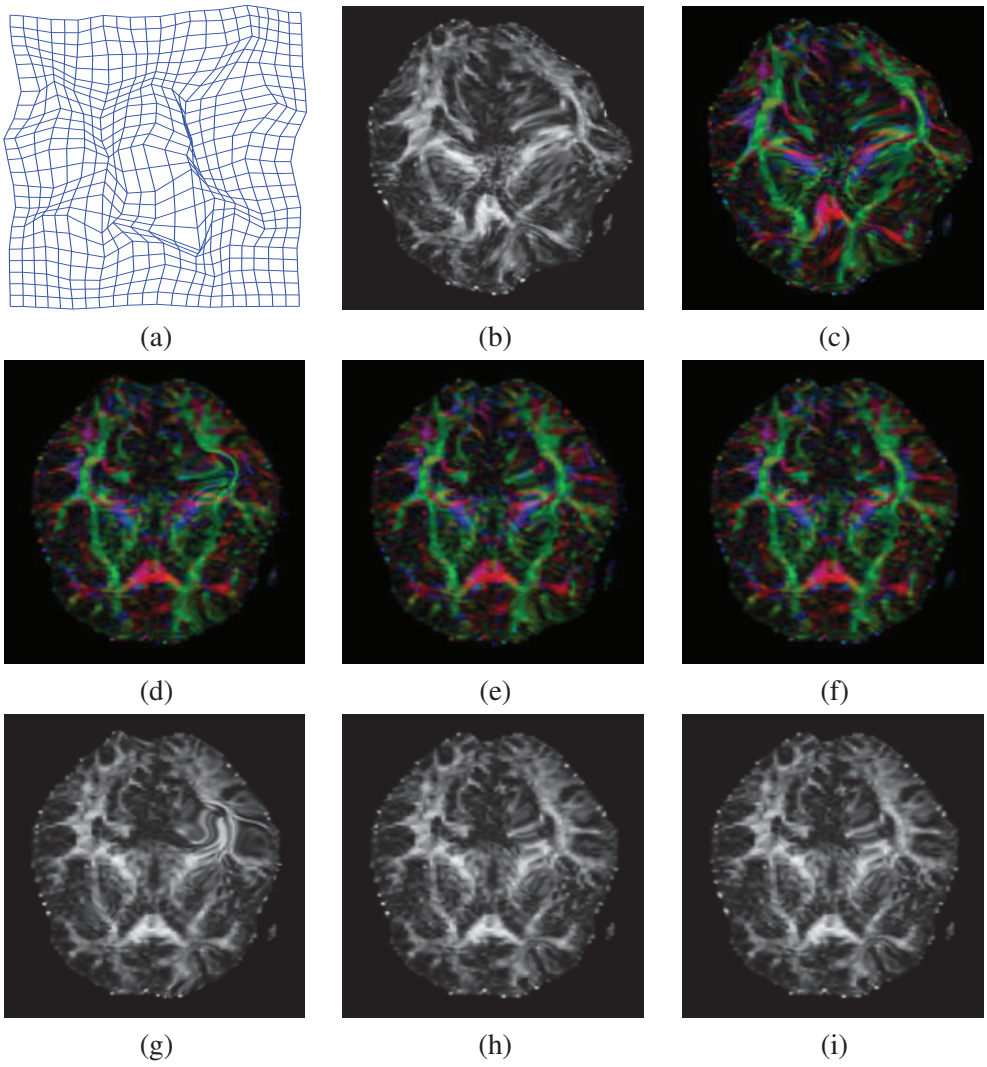

FIGURE 4.8: Geometric distortion experiment: (a) Ground truth deformation field; (b)-(c) distorted FA and DT elements' images, respectively, with geometric distortion; (d)-(f) DT elements of the registered images using affine, JT-FA, and JT-DT, respectively; (g)-(i) FA of the registered images using affine, JT-FA, and JT-DT, respectively.

4.4.4 EFFECT OF NOISE

In the second experiment, we studied the effect of noise on the registration accuracy. The DWI images of both the fixed and deformed moving images were corrupted with different levels, represented by σ, of Rician noise. Then, the FA and DT elements were computed from the noisy DW images. After registration, a transformation is found for each voxel from the moving to fixed image. Then, the estimated deformation field is applied to the moving image without noise so that the quantitative measures indicate the effect of noise on the alignment error itself.

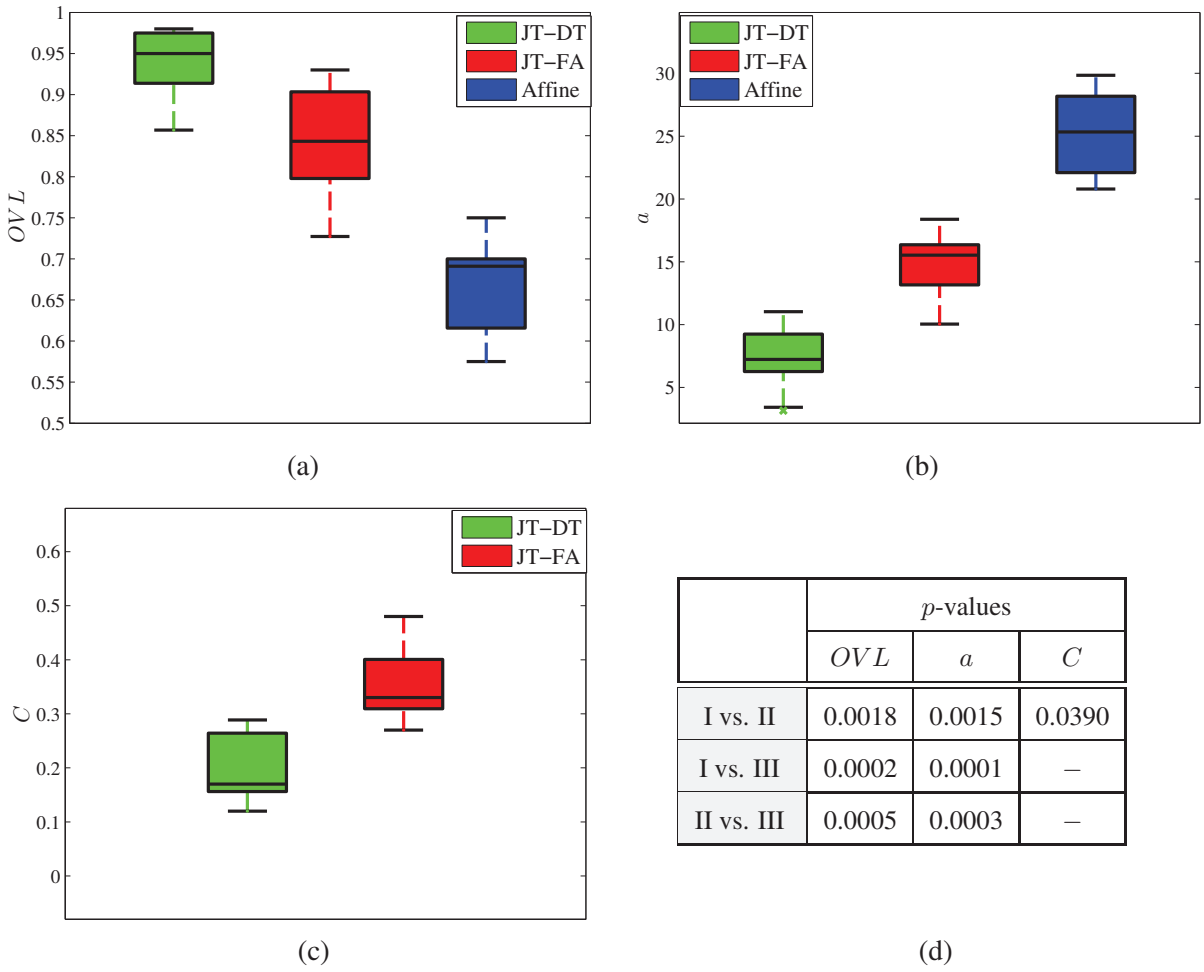

	p-values		
	OVL	a	C
I vs. II	0.0018	0.0015	0.0390
I vs. III	0.0002	0.0001	–
II vs. III	0.0005	0.0003	–

FIGURE 4.9: Quantitative registration results of deformed image data sets with known deformation fields. JT-DT, JT-FA, and affine registration methods are displayed on the horizontal axis, respectively. (a) The OVL measures the eigenvalue-eigenvector overlap of tensors in corresponding voxels between the reference and registered images. (b) The angle difference between the first eigenvectors of corresponding voxels in the reference and registered images. (c) The measure C calculates the discrepancy between the estimated deformation field and ground truth deformation field. (d) The p-values between the JT-DT, JT-FA, and affine registration techniques represented by I, II, III respectively, are displayed for quantitative parameters.

In Figure 4.10, the alignment results are displayed in the presence of different levels of noise. As shown in the figure, the results obtained by our registration approach JT-DT indicate that the spatial alignment and the orientation correspondence are still preserved even in high noise environments.

4.4.5 INTERSUBJECT TEST

To assess the performance of our proposed algorithm on intersubjet registration, we apply it to a normalized set of DT-MR images. The data set consists of nine subjects with Parkinson's disease, aged between 64 and 78 years. The DW-MR brain volumes were provided by CIEN-Fundación Reina Sofia in Madrid, Spain. These volumes were acquired with a 3 Tesla General Electric scanner equipped with an 8-channel coil. The DW images were obtained with a single-shot spin-eco EPI sequence (FOV=24 cm, TR=9.1 s, TE=88.9 ms, slice thickness=3 mm, spacing=0.3 mm, matrix size= 128×128, NEX=2). Each DW-MRI data set consists of one volume obtained with $b = 0\,\text{s/mm}^2$ and 15 volumes obtained with $b = 1000\,\text{s/mm}^2$, which correspond to the gradient directions specified in [71].

In this experiment, one of these subjects is chosen as a reference image and the other eight subjects are then registered to that reference using the aforementioned registration algorithms. Figure 4.11 through Figure 4.12 show the axial slice No. 21 before and after registration using JT-DT, JT-FA, and affine registration methods, respectively. The axial slice, chosen as a reference, is displayed on the top left in all these figures. In Figure 4.14, the alignment of all eight subjects to the reference subject are greatly improved after applying JT-DT algorithm compared to the results obtained using JT-FA and JT-affine algorithms, as shown in Figures 4.13 and 4.12, respectively. Moreover, it can be seen that the affine registration method is not able to remove the large differences in the shape of the corpus callosum and left and right hemisphere between the reference and the eight target images while using JT-DT and JT-FA registration algorithms reduce greatly the shape variations.

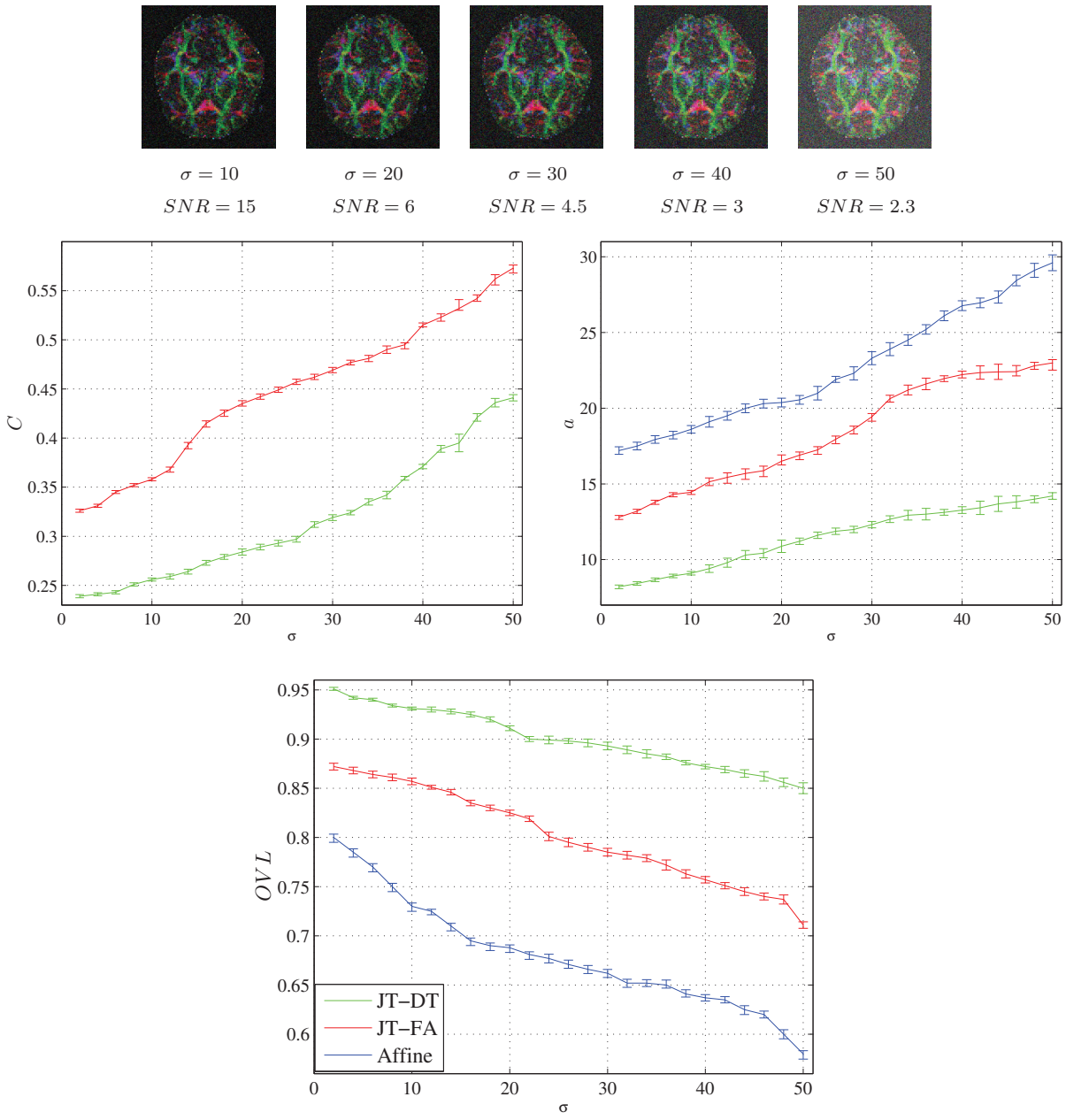

FIGURE 4.10: Effect of noise. Top: DTI data after corrupting the DW images with different levels of Rician noise. The DT elements' representation is according to diffusion direction. Middle and bottom: Spatial and orientation correspondence are given using JT-FA, JT-DT, and affine algorithms. The values of C, a, and OVL represent the median deformation field correspondence, the median first eigenvector angle difference, and the eigenvalue-eigenvector overlap, respectively.

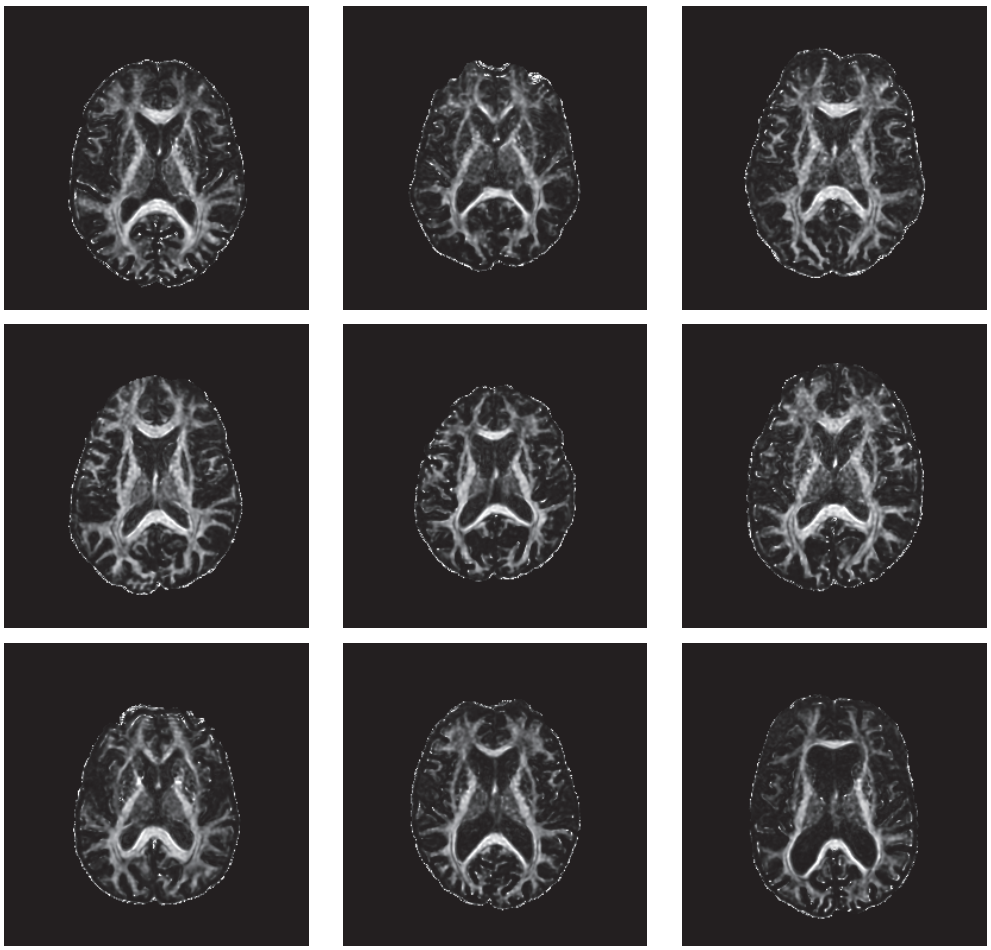

FIGURE 4.11: The FA map of the axial slice No. 21 computed from the diffusion tensor of each subject is presented. The image from the subject chosen as a template is shown on the top-left. The rest of the images are from the other 8 subjects before registration.

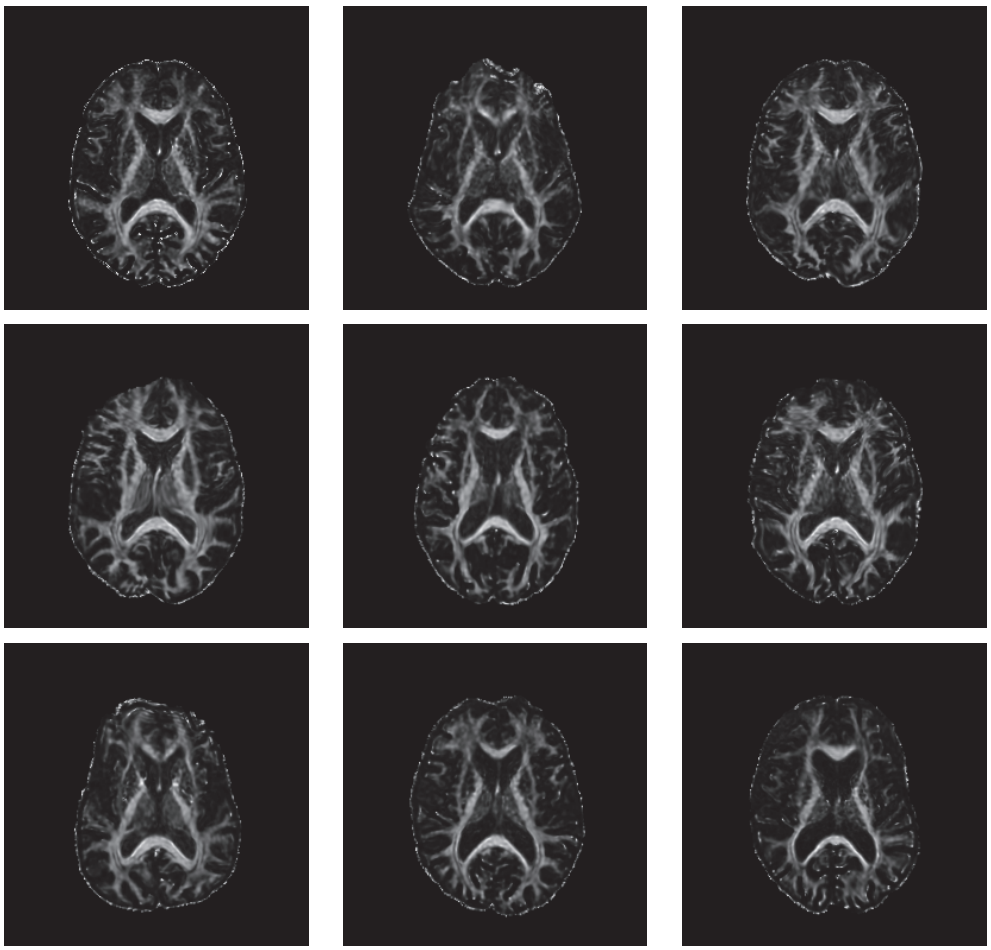

FIGURE 4.12: The FA map of the axial slice No. 21 computed from the diffusion tensor of each subject is presented. The image from the subject chosen as a template is shown on the top-left. The rest of the images are from the other 8 subjects after registration to the template with the affine registration algorithm.

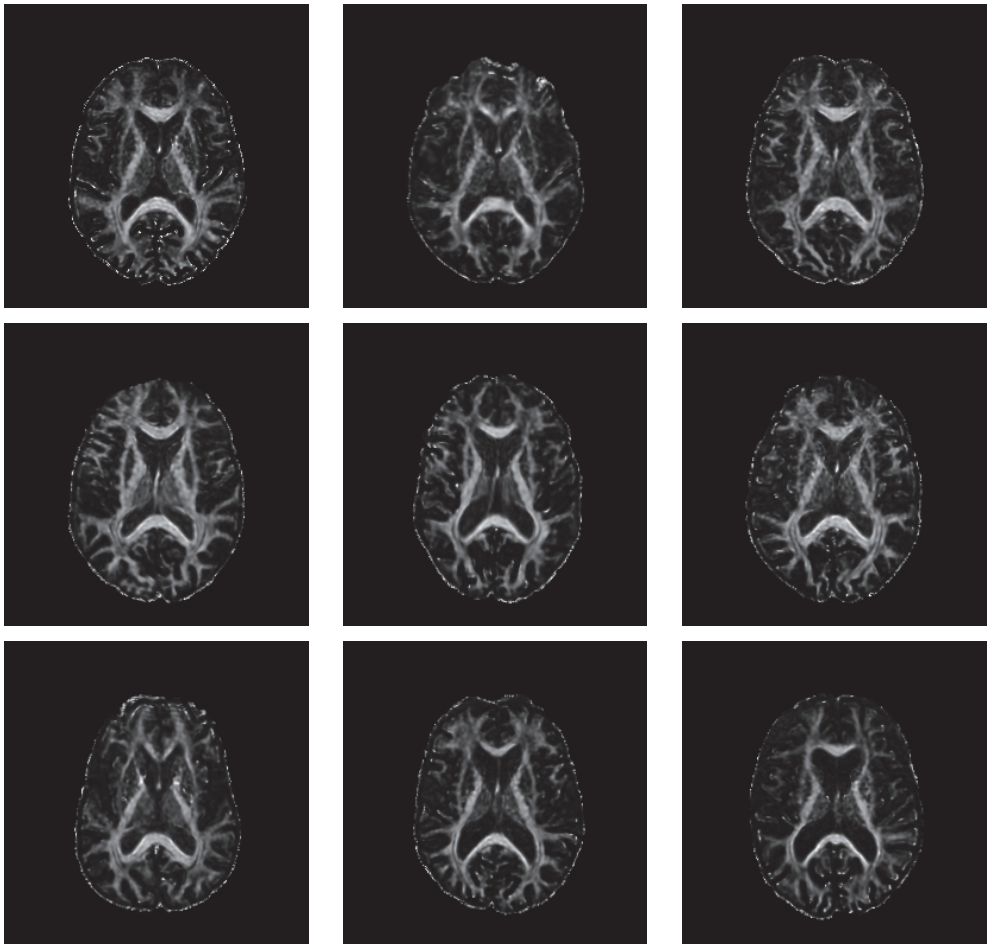

FIGURE 4.13: The FA map of the axial slice No. 21 computed from the diffusion tensor of each subject is presented. The image from the subject chosen as a template is shown on the top-left. The rest of the images are from the other 8 subjects. The rest of the images are from the other 8 subjects after registration to the template with the JT-FA algorithm.

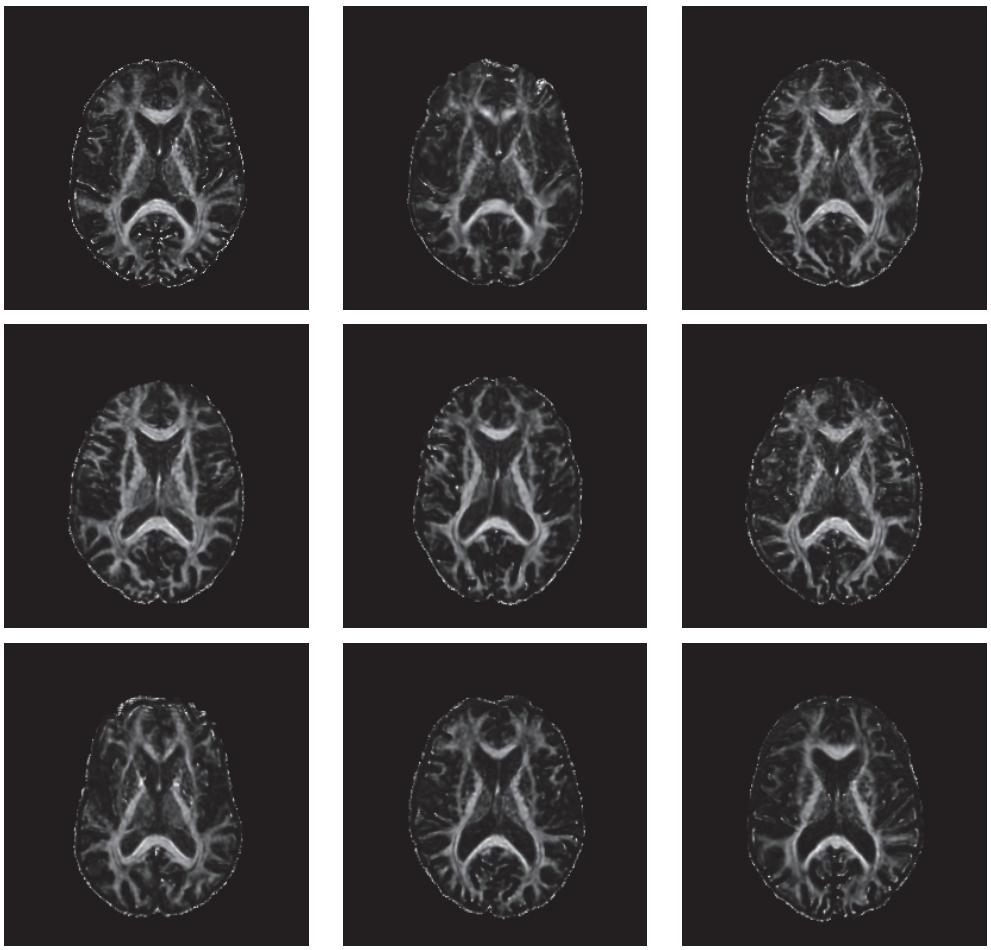

FIGURE 4.14: The FA map of the axial slice No. 21 calculated from the diffusion tensor of each subject is presented in this figure. The image from the subject chosen as a template is shown on the top-left. The rest of the images are from the other 8 subjects after registration to the template with the JT-DT algorithm.

CHAPTER 5

CONCLUSIONS AND FUTURE WORK

This chapter briefly concludes the thesis and highlights the major contributions of this research.

This thesis presented an image registration framework in the information-theoretic setting. The proposed approaches were successfully applied to multimodality and nonrigid medical images as well as diffusion tensor image registration. We have demonstrated the effectiveness of the proposed methods through numerical experiments on a variety of medical images.

In the next section, the contributions made in each of the previous chapters and the concluding results drawn from the associated research work are presented. Suggestions for future research directions related to this thesis are provided in Section 5.2.

5.1 THESIS CONTRIBUTIONS

5.1.1 AN INFORMATION-THEORETIC METHOD FOR MULTIMODALITY IMAGE REGISTRATION

In Chapter 2, we proposed an entropic framework for multimodal image registration. The proposed algorithm was applied to medical images of different modalities. The experimental results on MR to CT and MR to PET registrations indicated the feasibility of the proposed approach and a much better performance compared to MI and NMI-based methods, not only in terms of wider capture range of registration functions but also in terms of robustness to noise.

5.1.2 Nonrigid Image Registration using an Entropic Similarity

In Chapter 3, we presented an information-theoretic methodology for nonrigid image registration. The experimental results on (MR-)T1-T1 and (MR-)T1-T2 registrations indicate the feasibility of the proposed approach and a much better performance compared to RC and NMI methods, not only in terms of registration accuracy in the presence of intensity and geometric distortion but also in terms of nonrigidly registering images of different protocols and modalities. The feasibility of the proposed algorithm was also demonstrated on clinically acquired 4D CT image data sets.

5.1.3 Nonrigid Registration of DTI using a Multicomponent Entropic Similarity

In Chapter 4, we proposed a technique for nonrigid registration of diffusion tensor images by extending our deformable registration algorithm described in Chapter 3. In the proposed approach, we enable explicit orientation optimization by incorporating tensor reorientation, which is necessary for wrapping diffusion tensor images. The experimental results on DTI image registrations indicated the feasibility of the proposed approach and a much better performance compared to the affine registration method based on mutual information, not only in terms of registration accuracy in the presence of geometric distortion but also in terms of resistance to Rician noise.

5.2 Future Research Directions

Several interesting research directions motivated by this thesis are discussed next. In addition to focusing on further improving the results of nonrigid image registration, we also intend to accomplish the following projects in the near future:

5.2.1 Image Denoising

Our ongoing efforts are focused on exploring the use of image denoising as a prerequisite to image registration. We intend to develop an image denoising approach for diffusion tensor imaging in the variational framework.

5.2.2 Image Fusion

Another possible future work direction is image fusion. It would be of great interest to fuse images after their registration. Images are usually registered for the purpose of combining or comparing them, enabling

the fusion of information in the images. Incorporating image fusion with our nonrigid registration algorithm will provide a systematic framework which extracts information from input images such that the fused image provides better information for human or machine perception as compared to any of the input images.

5.2.3 Group-wise Image Registration

Another possible future work direction is to extend the Jensen-Tsallis similarity measure to register a set of multiple images. The key idea is to register all image frames to the average (mean) image.

5.2.4 Diffusion Tensor Imaging Atlas

Another future work direction is to investigate a framework for constructing DTI atlases by incorporating our DTI-based nonrigid image registration technique.

REFERENCES

[1] T.M. Cover and J.A. Thomas, *Elements of information theory*, Wiley Series in Telecommunications, John Wiley and Sons Inc., New York, 1991.

[2] R. Woods, S. Cherry, and J. Maziotta, "Rapid automated algorithm for aligning and reslicing PET images," *Journal of Comput Assist. Tomography*, vol. 16, no. 4, pp. 622-633, 1992.

[3] A. Collignon, D. Vandermeulen, P. Seutens, and G. Marchal, "3D multi-modality medical image registration using feature space clustering," *Proc. CVRMed*, Lecture Notes in Computer Science (LNCS), vol. 905, pp. 195-204, 1995.

[4] C. Studholme, D.L.G. Hill, and D.J. Hawkes, "Incorporating connected region labeling into automated image registration using mutual information," *Proc. IEEE Workshop on Mathematical Methods in Biomedical Image Analysis*, pp. 23-31, 1996.

[5] I. Bankman, *Handbook of Medical Image Processing and Analysis*, Academic Press, 2008.

[6] J.V. Hajnal, D.L.G. Hill, D.J. Hawkes, *Medical Image Registration*, CRC Press, 2001.

[7] A.A. Goshtasby, *2-D and 3-D Image Registration for Medical, Remote Sensing, and Industrial Applications*, Wiley Publishers, 2005.

[8] K.P. Wilkie and E.R. Vrscay, "Mutual information-based methods to improve local region-of-interest image registration," *Proc. ICIAR*, pp. 63-72, 2005.

[9] W.M. Wells, P. Viola, H. Atsumi, S. Nakajima, and R. Kikinis, "Multi-modal volume registration by maximization of mutual information," *Medical Image Analysis*, vol. 1, no. 1, pp. 35-51, 1996.

[10] P. Viola and W.M. Wells, "Alignment by maximization of mutual information," *International Journal of Computer Vision*, vol. 24, no. 2, pp. 173-154, 1997.

[11] F. Maes, A. Collignon, D. Vandermeulen, G. Marchal, and P. Suetens, "Multimodality image registration by maximization of mutual information," *IEEE Trans. Medical Imaging*, vol. 16, no. 2, pp. 187-198, 1997.

[12] F. Maes, D. Vandermeulen, P. Suetens, "Medical image registration using mutual information," *Proceedings of the IEEE*, vol. 91, no. 10, pp. 1699-1722, 2003.

[13] J.P.W. Pluim, J.B. Maintz, and M.A. Viergever, "Mutual-information-based registration of medical images: a survey," *IEEE Trans. Medical Imaging*, vol. 22, no. 8, pp. 986-1004, 2003.

[14] A.O. Hero, B. Ma, O. Michel, and J. Gorman, "Applications of entropic spanning graphs," *IEEE Signal Processing Magazine*, vol. 19, no. 5, pp. 85-95, 2002.

[15] J.P.W. Pluim, J.B.A. Maintz, and M.A. Viergever, "f-information measures in medical image registration," *IEEE Trans. Medical Imaging*, vol. 23, no. 12, pp. 1508-1516, 2004.

[16] H. Luan, F. Qi, Z. Xue, L. Chen, and D. Shen, "Multimodality image registration by maximization of quantitative-qualitative measure of mutual information," *Pattern Recognition*, vol. 41, pp. 285-298, 2008.

[17] C. Studholme, D. L. G. Hill, and D. J. Hawkes, "An overlap invariant entropy measure of 3D medical image alignment," *Pattern Recognition*, vol. 32, pp. 71-86, 1999.

[18] N.D. Cahill, J.A. Schnabel, J.A. Noble, and D.J. Hawkes, "Revisiting overlap invariance in medical image alignment," *Proc. IEEE Computer Vision and Pattern Recognition Workshops*, pp. 1-8, 2008.

[19] Y. He, A. Ben Hamza, and H. Krim, "A generalized divergence measure for robust image registration," *IEEE Trans. Signal Processing*, vol. 51, no. 5, pp. 1211-1220, 2003.

[20] D. Corici and J. Astola, "Segmentation of DNA into coding and noncoding regions based on recursive entropic segmentation and stop-codon statistics," *EURASIP Journal on Advances in Signal Processing*, vol. 1, pp. 81-91, 2004.

[21] L.S. Hibbard,"Region segmentation using information divergence measures," *Medical Image Analysis*, vol. 8, no. 3, pp. 233-244, 2004.

[22] M-C. Chiang, R.A. Dutton, K.M. Hayashi, O.L. Lopez, H.J. Aizenstein, A.W. Toga, J.T. Becker, and P.M. Thompson, "3D pattern of brain atrophy in HIV/AIDS visualized using tensor-based morphometry," *NeuroImage*, vol. 34, no. 1, pp. 44-60, 2007.

[23] D. Karakos, S. Khudanpur, J. Eisner, and C.E. Priebe, "Iterative denoising using Jensen-Rényi divergences with an application to unsupervised document categorization," *Proc. IEEE Inter. Conference on Acoustics, Speech and Signal Processing*, 2007.

[24] M.R. Sabuncu and P. Ramadge, "Using spanning graphs for efficient image registration," *IEEE Trans. Image Processing*, vol. 17, no. 5, pp. 788-797, 2008.

[25] C. Tsallis, "Possible generalization of Boltzmann-Gibbs statistics," *Journal of Statistical Physics*, vol. 52, pp. 479-487, 1988.

[26] S. Martin, G. Morison, W. Nailon, and T. Durrani, "Fast and accurate image registration using Tsallis entropy and simultaneous perturbation stochastic approximation," *Electronic Letters*, vol. 40, no. 10, pp. 595-597, 2004.

[27] J.C. Spall, "Multivariate stochastic approximation using a simultaneous perturbation gradient approximation," *IEEE Trans. Automatic Control*, vol. 37, no. 3, pp. 332-341, 1992.

[28] W. Mohamed, Y. Zhang, A. Ben Hamza, and N. Bouguila, "Stochastic optimization approach for entropic image alignment," *Proc. IEEE Inter. Symposium on Information Theory*, pp. 2126-2130, 2008.

[29] D-J. Kroon and C.H. Slump, "MRI modality transformation in demon registration," *IEEE Inter. Symposium on Biomedical Imaging: From Nano to Macro*, pp. 963-966, 2009.

[30] J. Burbea and C.R. Rao, "On the convexity of some divergence measures based on entropy functions," *IEEE Trans. Information Theory*, vol. 28, no. 3, pp. 489-495, 1982.

[31] J.C. Spall, "Implementation of the simultaneous perturbation algorithm for stochastic optimization," *IEEE Trans. Aerospace and Electronic Systems*, vol. 34, no. 3, pp. 817-823, 1998.

[32] J. West, F. Fitzpatrick, M. Wang, B. Dawant, C. Maurer, R. Kessler, and R. Maciunas, "Comparison and evalucation of retrospective intermodality image registration techniques," *Proc. SPIE Conference on Medical Imaging*, 1996.

[33] [Online]. Available: http://www.insight-journal.org/rire/

[34] H. Chui, L. Wing, R. Schultz, J. Duncan, and A. Rangarajian, "A unified non-rigid feature registration method for brain mapping," *Medical Image Analysis*, vol. 7, no.2, pp. 112-130, 2003.

[35] M. Yasein and P. Agathoklis, "A feature-based image registration technique for images of different scale," *IEEE Int. Symposium on Circuits and Systems*, pp. 3558-3561, 2008.

[36] N. Paragios, M. Rousson, and V. Ramesh, "Non-rigid registration using distance functions," *Computer Vision and Image Understanding*, vol. 89, no. 2-3, pp. 142-165, 2003.

[37] M. Audette, K. Siddiqi, F. Ferrie, and T. Peters, "An integrated range-sensing, segmentation and registration framework for the characterization of intra-surgical brain deformations in image-guided surgery," *Computer Vision and Image Understanding*, vol. 89, no. 2-3, pp. 226-251, 2003.

[38] A. Leow, P. Thompson, H. Protas, and S. Huang, "Brain warping with implicit representations." *Proc. IEEE Int. Symposium on Biomedical Imaging: Nano to Macro*, pp. 603-606, 2004.

[39] D. Rueckert, L. Sonoda, C. Hayes, D. Hill, M. Leach, and D. Hawkes, "Nonrigid registration using free-form deformations: Application to breast MR images," *IEEE Trans. Medical Imaging*, vol. 18, no. 8, pp. 712-721, 1999.

[40] C. Davatzikos, "Spatial transformation and registration of brain images using elastically deformable models," *Computer Vision and Image Understanding*, vol. 66, no. 2, pp. 207-222, 1997.

[41] J. Gee, M. Reivich, and R. Bajcsy, "Elastically deforming 3d atlas to match anatomical brain images," *Journal of Computer Assisted Tomography*, vol. 17, no. 2, pp. 225-236, 1993.

[42] M. Bro-Nielsen and C. Gramkow, "Fast fluid registration of medical images," *Proc. Int. Conf. Visualization in Biomedical Computing*, pp. 267-276, 1993.

[43] G. Christensen, R. Rabbitt, and M. Miller, "Deformable templates using large deformation kinematics," *IEEE Trans. Image Processing*, vol. 5, no. 10, pp. 1435-1447, 1996.

[44] A. Andronache, M. Siebenthal, G. Szekely, and P. Cattin "Non-rigid registration of multi-modal images using both mutual information and cross-correlation," *Medical Image Analysis*, vol. 12, no. 1, pp. 3-15, 2008.

[45] B. Likar and F. Pernus, "A hierarchical approach to elastic registration based on mutual information," *Image and Vision Computing*, vol. 19, pp. 33-44, 2001.

[46] F. Wang and B. Vemuri, "Non-rigid multi-modal image registration using cross-cumulative residual entropy," *International Journal of Computer Vision*, vol. 74, no. 2, pp. 201-215, 2007.

[47] D. Loeckx, P. Slagmolen, F. Maes, D. Vandermeulen, and P. Suetens, "Nonrigid image registration using conditional mutual information," *IEEE Trans. Medical Imaging*, vol. 29, no. 1, pp. 19-29, 2007.

[48] A. Myronenko and X. Song, "Image registration by minimization of residual complexity," *Proc. CVPR*, pp. 49-56, 2009.

[49] A. Myronenko and X. Song, "Intensity-based image registration by minimizing residual complexity," *IEEE Trans. Medical Imaging*, vol. 29, no. 11, pp. 1882-1891, 2010.

[50] C. Tsallis, "Possible generalization of Boltzmann-Gibbs statistics," *Journal of Statistical Physics*, vol. 52, pp. 479-487, 1988.

[51] M.P. Wachowiak, R. Smolikova, G.D. Tourassi, and A.S. Elmaghraby, "Similarity metrics based on nonadditive entropies for 2D-3D multimodal biomedical image registration," *Proc. SPIE of Medical Imaging*, vol. 5032, pp. 1090-1100, 2003.

[52] G. Wahba, *Spline models for observational data*, SIAM, 1990.

[53] D. Mattes, D. R. Haynor, H. Vesselle, T. K. Lewellen, and W. Eubank, "PET-CT image registration in the chest using free-form deformations," *IEEE Trans. Medical Imaging*, vol. 22, no. 1, pp. 120-128, 2003.

[54] A. Ben Hamza, "A nonextensive information-theoretic measure for image edge detection," *Journal of Electronic Imaging*, vol. 15, no. 1, pp. 130111-130118, 2006.

[55] J. Nocedal and S. J. Wright, *Numerical Optimization*. New York: Springer-Verlag, ch. 8-9, 2000.

[56] [Online]. Available: http://www.bic.mni.mcgill.ca/brainweb/

[57] H. Luan, F. Qi, Z. Xue, L. Chen, and D. Shen, "Multimodality image registration by maximization of quantitative-qualitative measure of mutual information," *Pattern Recognition*, vol. 41, pp. 285-298, 2008.

[58] [Online]. Available: http://www.dir-lab.com

[59] R. Castillo, E. Castillo, R. Guerra, V. Johnson, T. McPhail, A. Garg, and T. Guerrero, "A framework for evaluation of deformable image registration spatial accuracy using large landmark point sets," *Physics in Medicine and Biology*, vol. 54, no. 7, pp. 1849-1870, 2009.

[60] P. J. Basser, J. Mattiello, and D. Le Bihan, "MR diffusion tensor spectroscopy and imaging," *Biophysical Journal*, vol. 66, no. 1, pp. 259-267, 1994.

[61] M. Rovaris, A. Gass, R. Bammer, S. Hickman, O. Ciccarelli, D. Miller, and M. Filippi, "Diffusion MRI in multiple sclerosis," *Neurology*, vol. 65, no. 10, pp. 15261532, 2005.

[62] D.C. Alexander, C. Pierpaoli, P.J. Basser, and J.C. Gee, "Spatial transformations of diffusion tensor magnetic resonance images," *IEEE Trans. Medical Imaging*, vol. 20, no. 11, pp. 11311139, 2001.

[63] Y. Cao, M. Miller, S. Mori,R. Winslow, and L. Younes, "Diffeomorphic matching of diffusion tensor images," *Proc. CVPR*, 2006.

[64] H. Zhang, P. Yushkevich, D. Alexander, and J. Gee, "Deformable registration of diffusion tensor MR images with explicit orientation optimization," *Medical Image Analysis*, vol. 10, no. 5, pp. 764-785, 2006.

[65] J. Ruiz-Alzola, C-F. Westin, S. Warfield, A. Nabavi, and R. Kikinis, "Nonrigid registration of 3D tensor medical data," *Medical Image Analysis*, vol. 6, no. 2, pp. 143-161, 2002.

[66] A. Einstein. "Uber die von der molekularkinetischen Theorie der Warme geforderte Bewegung von in ruhenden Flussigkeiten suspendierten Teilchen," *Annals of Physics*, vol.4, pp. 549560, 1905.

[67] D. Le Bihan, *Diffusion and Perfusion Magnetic Resonance Imaging: Applications to Functional MRI*, Raven Press, New York, 1995.

[68] L. Landau and E. Lifschitz, *Statistical Physics*, Butterworth-Heinemann, 1999.

[69] C. Beaulieu, "The basis of anisotropic water diffusion in the nervous system," *NMR in Biomedicine*, vol. 15, pp. 435-455, 2002.

[70] E. Stejskal and J. Tanner, "Spin diffusion measurements: spin echoes in the presence of a tim-dependent field gradient," *Journal of Chemical Physics*, vol. 42, pp. 288-292, 1965.

[71] D. Jones, M. Horsfield, and A. Simmons, "Optimal strategies for measuring diffusion in anisotropic systems by magnetic resonance imaging," *Journal of Magnetic Resonance in Medicine*, vol. 42, no. 3, pp 515-525, 1999.

[72] D. Alexander, J. Gee, and R. Bajcsy, "Elastic matching of diffusion tensor MRIs," *Proc. CVPR*, pp. 244-249, 1999.

[73] D. Jones, L. Griffin, D. Alexander, M. Catani, M. Horsfield, R. Howard, and S. Williams, "Spatial normalization and averaging of diffusion tensor MRI data sets," *NeuroImage*, vol. 17, no. 2, pp. 592617, 2002.

[74] A. Guimond, C. Guttmann, S. Warfield, and C. Westin, "Deformable registration of DT-MRI data based on transformation invariant tensor characteristics," *Proc. ISBI*, pp. 1-4, 2002.

[75] D. Xu, S. Mori, D. Shen, P. van Zijl, and C. Davatzikos, "Spatial normalization of diffusion tensor fields," *Magnetic Resonance in Medicine*, vol. 50, no. 1, pp. 175-182, 2003.

[76] A. Leemans, J. Sijbers, S. De Backer, E. Vandervliet, and P.M. Parizel "Nonrigid coregistration of diffusion tensor images using a viscous fluid model and mutual information," *Proc. ACIVS*, LNCS 3708, pp. 523530, 2005.

[77] W. Hecke, A. Leemans, E. D'Agostino, S. De Backer, E. Vandervliet, P.M. Parizel, J. Sijbers "Affine coregistration of diffusion tensor magnetic resonance images using mutual information," *IEEE Trans. Medical Imaging*, vol. 26, no. 11, pp. 1598-1612, 2007.

[78] H.J. Park, M. Kubicki, M. Shenton, A. Guimond, R. McCarley, S. Maier, R. Kikinis, F. Jolesz, and C.F. Westin, "Spatial normalization of diffusion tensor MRI using multiple channels," *NeuroImage*, vol. 20, no. 4, pp. 1995-2009, 2003.

[79] J.P. Thirion, "Image matching as a diffusion process: An analogy with maxwells demons," *Medical Image Analysis*, vol. 2, no. 3, pp. 243-260, 1998.

[80] [Online]. Available: http://insight-journal.org/midas/collection/view/190.

[81] A. Anderson, "Theoretical analysis of the effects of noise on diffusion tensor imaging," *Magnetic Resonance in Medicine*, vol. 46, no. 6, pp. 1174-1188, 2001.

[82] J.F. Mangin, C. Poupon, C. Clark, D. Le Bihan, and I. Bloch, "Distortion correction and robust tensor estimation for MR diffusion imaging," *Medical Image Analysis*, vol. 6, no. 3, pp. 191198, 2002.

[83] W.D. Taylor, E. Hsu, K.R. Krishnan, and J.R. MacFall, "Diffusion tensor imaging: background, potential, and utility in psychiatric research," *Biological Psychiatry*, vol. 55, no. 3, pp. 201-207, 2004.

[84] S. Mori and P. Zijl, "Diffusion weighting by the trace of the diffusion tensor within a single scan," *Magnetic Resonance in Medicine*, vol. 33, pp. 41-52, 1995.

[85] M. Khader and A. Ben Hamza, "An information-theoretic method for multimodality medical image registration," *Journal of Expert Systems with Applications*, Elsevier, vol. 39, no. 5, pp. 5548-5556, 2012.

[86] M. Khader and A. Ben Hamza, "Non-rigid image registration using an entropic similarity," *IEEE Trans. Information Technology in Biomedicine*, vol. 15, no. 5, pp. 681-690, 2011.

[87] M. Khader and A. Ben Hamza, "An entropy-based technique for nonrigid medical image alignment," *Proc. IWCIA*, Lecture Notes in Computer Science, vol. 6636, pp. 444-455, 2011.

[88] M. Khader, A. Ben Hamza, and P. Bhattacharya, "Multimodality image alignment using information-theoretic approach," *Proc. ICIAR*, Lecture Notes in Computer Science, vol. 6112, pp. 30-39, 2010.